

CRITICAL PHENOMENA
IN
SUPERCONDUCTORS

MASTER

James Clark Solinsky

**Solid State and Low Temperature
Physics Group**

SCHOOL OF PHYSICS AND ASTRONOMY



DECEMBER 1973

UNIVERSITY OF MINNESOTA
MINNEAPOLIS, MINNESOTA

DISTRIBUTION OF THIS DOCUMENT IS UNLIMITED

Work supported in part by the U.S. Atomic Energy Commission

DISCLAIMER

This report was prepared as an account of work sponsored by an agency of the United States Government. Neither the United States Government nor any agency Thereof, nor any of their employees, makes any warranty, express or implied, or assumes any legal liability or responsibility for the accuracy, completeness, or usefulness of any information, apparatus, product, or process disclosed, or represents that its use would not infringe privately owned rights. Reference herein to any specific commercial product, process, or service by trade name, trademark, manufacturer, or otherwise does not necessarily constitute or imply its endorsement, recommendation, or favoring by the United States Government or any agency thereof. The views and opinions of authors expressed herein do not necessarily state or reflect those of the United States Government or any agency thereof.

DISCLAIMER

Portions of this document may be illegible in electronic image products. Images are produced from the best available original document.

CRITICAL PHENOMENA
IN
SUPERCONDUCTORS

A THESIS
SUBMITTED TO THE FACULTY OF THE GRADUATE SCHOOL
OF THE UNIVERSITY OF MINNESOTA

BY

JAMES CLARK SOLINSKY

IN PARTIAL FULFILLMENT OF THE REQUIREMENTS
FOR THE DEGREE OF
DOCTOR OF PHILOSOPHY

DECEMBER 1973

NOTICE

This report was prepared as an account of work sponsored by the United States Government. Neither the United States nor the United States Atomic Energy Commission, nor any of their employees, nor any of their contractors, subcontractors, or their employees, makes any warranty, express or implied, or assumes any legal liability or responsibility for the accuracy, completeness or usefulness of any information, apparatus, product or process disclosed, or represents that its use would not infringe privately owned rights.

DISTRIBUTION OF THIS DOCUMENT IS UNLIMITED
FJ

Abstract

Critical Phenomena in Superconductors

Departures from the predictions of Mean Field Theory (MFT) are not usually observed because the region in temperature ΔT_c (i.e., the critical region) over which the theory is invalid is very small ($\sim 10^{-12}$ K) for pure superconductors. The narrowness of this region results from the dependence of ΔT_c on the inverse of the sixth power of the zero temperature value of the temperature dependent coherence length $\xi(T)$, a parameter which measures the size of coherent superconducting regions, and is about 10^4 \AA for pure superconductors. This relationship between ΔT_c and $\xi(0)$ is why in superfluid He^4 critical phenomena are observed ($\xi(0) \sim 2 \text{ \AA}$) and why MFT works so well for pure superconductors. But ΔT_c can be increased to the order of 10^{-3} K by studying dirty superconductors (i.e., the mean free path $\lambda \ll \xi(0)$) in restricted geometry (i.e., a characteristic length $L \ll \xi(0)$).

Experimental studies were carried out with 1000 \AA thick dirty granular aluminum films (mass $\sim 20 \text{ \mu g}$) which were evaporated onto mica substrates. The electrical conductivity and heat capacity were studied in the superconducting transition region. The resistive transition of the film was used as a thermometer in conjunction with optical heating in an A.C. calorimetry scheme to measure the films $5 \times 10^{-9} \text{ J/K}$ heat capacity. Results presented on

four films indicate a rise in the heat capacity near the low temperature region of the transition where the film's resistance becomes zero. This rise peaked in two films studied to a value of up to 32 times the BCS jump in heat capacity and at a temperature of about 20 mK below the MFT transition temperature T_c^{MFT} as determined from the conductivity measurements. An applied magnetic field widened and reduced the peak in the heat capacity while shifting it to a lower temperature. These results indicate that higher order corrections are needed to recent heat capacity predictions for thin films in the transition region.

Preface

Because dissertations tend to be written and then placed on obscure shelves, this thesis was structured to enable the reader to read what is important without all the small details. The main body of the thesis is without all the experimental details, and is written from a phenomenological point of view, with fine theoretical details to be found in the references. All experimental details are structured in appendices, and can be omitted in reading, if one so chooses. If this format does not make the thesis more readable, it at least helped the author in distinguishing between what is called research and what is called physics.

Table of Contents

	page
Abstract.....	i
Preface.....	iii
Table of Contents.....	iv
List of Tables and Figures.....	vi
Chapter 1. Introduction.....	1
Chapter 2. Theory.....	9
Fluctuation Enhancement.....	9
Estimation of the Critical Region.....	13
Theoretical Predictions.....	15
Chapter 3. Previous Experimental Work.....	29
Chapter 4. Experiment.....	42
Basic Methods.....	42
Apparatus.....	45
Equivalent Circuit.....	46
Error Analysis.....	56
Chapter 5. Data Analysis and Discussion.....	65
General Features.....	65
Electrical Conductivity.....	69
Heat Capacity.....	74
Magnetic Field Effects.....	77
Discussion.....	83
Conclusion.....	87
List of References.....	91

	Page
Appendix A. A.C. Bridges and Thermometry.....	95
Appendix B. Optical Systems.....	104
Appendix C. Cryostat and Isolation.....	110
Appendix D. SQUIDS.....	118
Appendix E. Functional Differentiation and Numerical Analysis.....	133
Appendix F. A.C. Calorimetry and the Heat Conduction Problem.....	146
Appendix G. Analog Servo System.....	166
Appendix H. Sample Preparation and Resistive Transitions.....	177
List of References for Appendices.....	202
Acknowledgements.....	207

List of Tables and Figures

	page
Figure 1. Lambda Transition in LHe^4	2
Figure 2. List of Phase Transitions.....	2
Table 1. Critical Regions for Different Systems.....	7
Figure 3. Predicted Fluctuation Heat Capacity Effects in Three Dimensions.....	12
Figure 4. Hartree Approximation Calculation for Three Dimensions.....	12
Table 2A. Heat Capacity Predictions for Superconductors.....	19
Table 2B. Conductivity Predictions for Superconductors.....	21
Figure 5. Predicted Fluctuation Heat Capacity in One Dimension...	25
Figure 6. Observed Fluctuation Heat Capacity in Two Dimensions...	25
Figure 7. Finite Anomaly Prediction in Two Dimensions.....	26
Figure 8. Finite Anomaly Prediction in Two Dimensions Compared to Hartree Result.....	26
Figure 9. Observed Heat Capacity of Pure Superconductors in Three Dimensions.....	30
Figure 10. Magnetic Field Heat Capacity Studies in Dirty, Bulk Superconductors.....	30
Figure 11. Comparison of Magnetic Field Studies to Hartree One Dimensional Predictions.....	33
Figure 12. Calorimeter Used by Zally and Moche1.....	33
Figure 13. Top View of Calorimeter Used by Zally and Moche1.....	35
Figure 14. Raw Calorimetry Data on Bi Films.....	35

Figure 15. Excess Heat Capacity and Resistive Transition of Bi Film.....	37
Figure 16. Comparison to Hartree Prediction for Bi Film Results..	37
Figure 17. Resistive Transition Used as a Non-linear Thermometer.	43
Figure 18. Equivalent Circuit Used in Analysis.....	43
Figure 19. Block Diagram of Electronics Used in Experiment.....	48
Figure 20. Raw Data Used in Experiment.....	61
Figure 21. Heat Capacity of 1000 Å Aluminum Film (#38B).....	63
Table 3. Physical Constants for Films Discussed.....	66
Figure 22. Resistive Transition From Run #39 with Theoretical Fit.....	71
Figure 23. Inverse of Excess Conductivity Ratio vs. Temperature for Run #39.....	73
Figure 24. Total Heat Capacity of Run #301, Plotted for Three Temperature Ranges.....	76
Figure 25. Resistive Transition for Run #36B, Showing Multiple Transitions.....	78
Figure 26. Resistive Transition and Heat Capacity for Run #36B...	79
Figure 27. Excess Heat Capacity Plotted for Run #39.....	81
Figure 28. Inverse of Excess Heat Capacity for Run #39.....	82
Figure 29. Total Heat Capacity for Run #39 for Two Values of Magnetic Field.....	84
Figure A-1. A.C. Resistance Bridge.....	96
Figure A-2. Self-Balancing Bridge.....	100
Figure A-3. A.C. Kelvin Bridge.....	101
Figure B-1. Optical Electronics.....	105

Figure B-2.	Output of Miniature Light Bulbs.....	106
Figure C-1.	Dewar Assembly and Isolation Platform.....	111
Figure C-2.	LHe Level Detector Circuit.....	114
Figure C-3.	Cryostat for Experiment.....	115
Figure D-1.	Basic Equations for SQUID Operation.....	119
Figure D-2.	SQUID Construction and Biasing.....	122
Figure D-3.	SQUID Electronics--Mixer and Oscillator.....	125
Figure D-4.	SQUID Electronics--Pre-Amp.....	126
Figure D-5.	SQUID D.C. Bias and Feedback Box.....	128
Figure D-6.	SQUID Critical Current Behavior.....	132
Figure E-1.	Basic Analog Differentiation.....	135
Figure E-2.	More Complicated Analog Differentiation.....	137
Figure E-3.	Higher Order Harmonic Detection Method.....	139
Figure E-4.	Small Modulation Differentiation.....	140
Figure E-5.	Multiplier Box.....	141
Figure F-1.	A. C. Calorimetry and Electrical Analog.....	147
Table F-1.	Electrical Analogy to Heat Flow.....	149
Figure F-2.	A.C. Heat Conduction for a Steel Rod.....	155
Table F-2.	Thermal Properties for Materials Used in the Experiment.....	159
Figure G-1.	Linear and Non-Linear Relationships for Servo System.	169
Figure G-2.	Block Diagram of Analog Computer.....	171
Figure G-3.	Non-Linear Functions Produced by Analog Computer.....	172
Figure G-4.	Active Filter Box.....	174
Figure G-5.	Block Diagram of Complete Servo System.....	175
Figure H-1.	TEM Micrographs of Aluminum Films.....	179

Figure H-2. Sample Geometries and Self-Supported Method.....	183
Figure H-3. Resistive Transition of a Self-Supported Film.....	189
Figure H-4. Time Dependence of "Notch" in Resistive Transition...	190
Figure H-5. Magnetic Broadening of Resistive Transitions.....	193
Figure H-6. Cumulative Data Compared to Patton's Theory.....	198

Chapter 1. Introduction

Among the many processes that one observes in the physical world, one of the most striking processes is that of a phase transition. A phase transition is characterized by a dramatic overall change in a system, brought about by a relatively small change in one of the parameters of the system. Figure 1 shows the heat capacity of liquid He^4 plotted vs. temperature. One should note the dramatic change in the heat capacity due to a relatively small change in the temperature. One should also note that as one increases the resolution of the variable parameter (temperature), the relative shape of the feature remains the same. This is a characteristic of the "critical region," and is related to the exponential power of the diverging quantity (see ref. 2; scaling theory). One can observe critical behavior in other systems as well. A more common example is the liquid-gas phase transition. One can ponder for a long time the question of why water boils at precisely one temperature and becomes a wholly different state of matter from the liquid.

Landau³ first realized the similarity in all phase transitions. He believed a phase transition to be due to a change in symmetry of the system which he characterized with a parameter called the "order parameter." For temperatures greater than the transition temperature (T_c) the system was in a disordered state, and the order parameter (Δ) had a zero average value. For temperatures

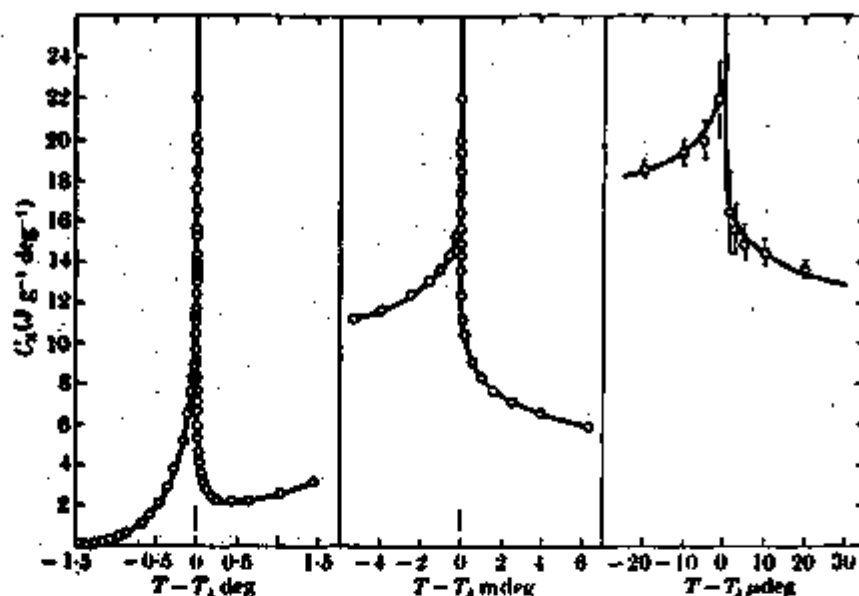


FIG. 1.10. Specific heat of ${}^4\text{He}$ as a function of $T - T_\lambda$ in K. Notice that the shape of the specific heat curve is rather like the Greek letter λ , whence the origin of the term ' λ -transition'. The fact that the specific heat is only about ten times its 'normal' value even at temperatures only a few microdegrees from T_λ is correlated with the fact that the critical-point exponent is extremely small (in fact, α is probably zero, corresponding to a logarithmic divergence). The width of the small vertical line just above the origin indicates the portion of the diagram that is expanded in width in the curve directly to the right. After Buckingham and Fairbank (1965).

Figure 1. (from Ref. 1)

Partial list of phase transitions and the order parameters $\langle p \rangle$ associated with each. Adapted from Kadanoff et al. (1967)

Transition	Meaning of $\langle p \rangle$	Free choice in $\langle p \rangle$	Thermodynamic conjugate of $\langle p \rangle$
liquid-gas	$p - p_c$	$p > 0 = \text{liquid}$ $p < 0 = \text{vapour}$ (2 choices)	μ
ferromagnetic	magnetisation M	if n equivalent 'easy axes' $2n$ choices	applied magnetic field, H , along easy axis
antiferromagnetic	sublattice magnetisation	if n 'easy axes' $2n$ choices	not physical
Heisenberg model ferromagnet	magnetisation M	direction of M (can choose any value on surface of sphere)	H
Ising model ferromagnet	s_i	2 choices	H
superconductors	Δ (complex gap parameter)	phase of Δ	not physical
superfluid	$\langle \psi \rangle$ (condensate wave function)	phase of $\langle \psi \rangle$	not physical
ferroelectric	lattice polarization	finite number of choices	electric field
phase separation	concentration	2 choices	a difference of chemical potentials

Figure 2. (from Ref. 1)

less than the transition temperature, the system was in an ordered state, and the order parameter had a non-zero average value. This is summarized below:

Landau Phase Transitions

$T > T_c$	$ \Delta = 0$	disordered
$T < T_c$	$ \Delta \neq 0$	ordered

An example of the order parameter can be shown by looking at a Curie-Weiss spin lattice, where N_+ is the number of spins up, and N_- is the number of spins down. Then $\Delta = (N_+ - N_-) / (N_+ + N_-)$ and then the order parameter obeys the rules shown above.

The universality of the order parameter idea is shown in Figure 2. The transition is listed in the first column with the order parameter listed in the second. The third column is the degeneracy, or "free choice" in the order parameter. One can see that for the superconducting transition, the order parameter is the complex energy gap parameter (Δ), sometimes written as $\psi (= Ae^{i\phi})$, which is like a quantum mechanical condensate wave function with its amplitude (A) relating to the square root of the density of electron pairs (Cooper pairs) in the system, and has a phase (ϕ) associated with it. One can add to the table the recent observations in ${}^3\text{He}$ at 2.7 mK of a possible phase transition similar to the pairing of a superconductor.

Landau used a phenomenological approach, which for a

superconductor has an equivalence in the microscopic B.C.S.⁴ theory near T_c . He expanded the thermodynamic free energy function as a power series in the order parameter with temperature dependent coefficients, where certain terms dropped out due to symmetry arguments. Thus, the free energy is:

$$F = F_n + \alpha |\Delta|^2 + \frac{\beta}{2} |\Delta|^4 + \dots \quad (1)$$

where F_n is the free energy above the transition temperature.

This is a type of Mean Field Theory (MFT) and is consistent with a second order phase transition in a superconductor (the name originally related to the order of the discontinuous derivative of the free energy, but now just implies no latent heat in the phase transition). This can be shown by minimizing the free energy with respect to the order parameter and calculating the heat capacities above and below T_c (where $C = T \frac{\partial^2 F}{\partial T^2}$)

At finite temperatures, above the critical temperature, it is possible to have thermally activated fluctuations in the order parameter. Then, the thermal average value of the order parameter is zero ($\langle \Delta \rangle = 0$), but the r.m.s. fluctuation in the order parameter about the thermal average value at a point r is not zero ($\langle \delta \Delta^2 \rangle = \langle (\Delta(r))^2 \rangle - \langle \Delta(r) \rangle^2$). Thus, to modify the MFT, a spatially varying term is added to the free energy ($C |\nabla \Delta|^2$) and eq. (1) becomes:

$$F = F_n + \alpha |\Delta|^2 + \frac{\beta}{2} |\Delta|^4 + C |\nabla \Delta|^2 + \dots \quad (2)$$

in the MFT with fluctuations, commonly called Fluctuation theory. The correlation function between two fluctuating regions can be calculated as;

$$g(\hat{r}, \hat{r}') = \langle (\Delta(\hat{r}) - \langle \Delta(\hat{r}) \rangle) (\Delta(\hat{r}') - \langle \Delta(\hat{r}') \rangle) \rangle \quad (3)$$

as was done by Kadanoff.² One finds a coherence length ($\xi(T)$) or range of this correlation function and a relaxation time ($1/\Gamma(T)$) associated with these fluctuations above the critical temperature, where:

$$\xi(T) = \xi(0) \epsilon^{-1/2} \quad T > T_c \quad \text{where} \quad \epsilon = \frac{T - T_c}{T_c} \quad (4)$$

$$\Gamma(T) = \Gamma(0) \epsilon^1$$

The relaxation time comes from the more complicated Time Dependent Ginzburg-Landau equation (T.D.G.L.).⁵ One can picture regions on the size of $[\xi(T)]^3$ in the system going superconducting for a time on the scale of $1/\Gamma(T)$ at temperatures above the critical temperature, in the so-called "classical region".

As one approaches closer to the critical temperature, the difference in entropy between the two states approaches zero (i.e., the definition of a 2nd order transition is $\Delta S|_{T_c} = 0$). Then, it takes very little change in entropy for the order parameter to fluctuate between the two states, and the fluctuations get more

violent. Since, the probability for the order parameter (Δ) to be between Δ and $(\Delta + \delta\Delta)$ varies as the exponential of the entropy, for $T > T_c$ where $\langle \Delta \rangle = 0$, this is the same as the probability for the order parameter being equal to the fluctuations $\langle \delta\Delta \rangle$.^{*} For small differences in the entropy between the two states, this probability is a Gaussian function of the difference in entropy. Thus, when one approaches the transition, the entropy difference approaches zero, and the probability of the fluctuations being on the order of the order parameter ($\langle \Delta \rangle \sim \langle \delta\Delta \rangle$) becomes enormous. One can see that the size of the fluctuations diverges, and their lifetime becomes infinite (eqs. (4), (5)), so that the system is approaching a coherent macroscopic mode. In this region, the MFT theory breaks down because of the diverging quantities, and one calls it the "critical region". The width of this region can be estimated in reduced temperature (ϵ) as shown below.

$$\epsilon_c = \frac{T - T_c}{T_c} \sim \left[\frac{k_B}{\Delta C \epsilon_0^3} \right]^2 \quad (\text{ref. 2}) \quad (8)$$

This estimate is similar to the thermal energy in the size of the coherent region ($k_B T_c / \epsilon_0^3$) being on the order of the average energy associated with the phase transition ($T_c \Delta C$), and where the exponent comes from the temperature dependence of $\xi(T)$. Table I lists a number of systems with their zero temperature coherence

^{*} See Landau and Lifshitz, Statistical Physics, (1969), pg. 343.

Table I

<u>System</u>	<u>$\xi(T=0)$</u>	<u>M.F.T.</u>
Magnetic	$\leq 2 \text{ \AA}$	No Good ($\epsilon_c < 10^{-2}$)
Ferroelectric	100 \AA	Good ($\epsilon_c < 10^{-4}$)
LHe ⁴	1 \AA	No Good ($\epsilon_c < 10^{-1}$)
Superconductor	10^4 \AA	Good ($\epsilon_c < 10^{-12}$)

length used in estimating the critical region. Thus, it is obvious why there are observable critical phenomena in LHe^4 , and why for a superconductor one would expect M.F.T. to work well and no observable critical behavior to exist.

The estimation of the critical region is somewhat arbitrary, and each calculation requires a specific estimation of its breakdown. But equation (6) is calculated from more general considerations, and is in major agreement with the estimates of others. One can then imagine the understanding of the phase transition in a superconductor as consisting of phenomenological M.F.T. regions (where the theory works well) on either side of the critical region and are a good approximation for microscopic B.C.S. theory. One uses approximations to approach closer to the critical region, to include fluctuations. And finally, in the critical region the M.F.T. with fluctuations breaks down and one can only use scaling theory. B.C.S. theory (including Gor'kov's integral equations) being a microscopic description, will work well throughout, but the calculations can be impossible near the critical region. One can estimate that in a superconductor, the critical region, and thus the region of divergent behavior, is extremely narrow, and one would expect to never observe such behavior. Essentially the description of a superconductor in the critical region is as difficult to predict theoretically as it is to observe experimentally.

Chapter 2. Theory

Fluctuation Enhancement

Because of the rather narrow regions in temperature predicted for observable critical behavior, one could conclude that in superconductors one would never observe fluctuation effects. There are, however, means of increasing the fluctuations of a superconductor to enhance the fluctuation effects. This enhancement will not only widen the estimated critical region, but will also change the nature of the fluctuation behavior, and in addition, lower the transition temperature.

Anderson⁶ made an analogy with other phase transitions and noted that "dirty" superconductors, where the electron mean free path was smaller than the coherence length ($\lambda \ll \xi(0)$ where now $\xi(0) = .85\sqrt{\lambda \xi_0}$), should have an enhanced critical region. The electrons cannot travel as fast, due to the more numerous collisions, and are not as effective in averaging out the fluctuations that lead to critical and fluctuation effects.

Little's⁷ work in microgeometries led to the suggestion that reduced dimensions would enhance fluctuations. Reducing the dimensions of a sample simply implies one of the characteristic lengths of the system (L) is less than the coherence length ($\xi(0)$). Thus, a 3-D system is a bulk material; 2-D is a thin film (thickness $= L$); 1-D is a wire (area $= L^2$); and 0-D is a powder (particle volume $= L^3$). One can imagine a ball bouncing in a 3-D box, and, as one pushes in two opposing sides, the bouncing increases as the system becomes a plane. It is this type of effect, in a quantum

mechanical sense, that allows the reduced geometry to enhance fluctuations.

More recently a third method has been suggested by Lee and Shenoy⁸ and others, to increase fluctuations. If one applies a small magnetic field to a metal, the motion of the electrons in the metal will be confined to planes (2-D) and (for higher fields) to 1-D rods. Thus, an applied magnetic field will reduce the dimensionality of the system to further enhance the fluctuations in a superconductor.

One can also think of fluctuations as an "inexact" pairing of the electrons in forming Cooper pairs.⁶ For the B.C.S. formulation, one has a total momentum equal to zero, but fluctuations allow local, non-precision pairing. This is equivalent to the Hartree-Fock self-consistency treatment of the phenomenological approach where one has a total constant value of the order parameter over space, but the $|\nabla\psi|^2$ term implies a local non-constant value. At temperatures above the transition ($T > T_c$), fluctuations are observable because there is no pair-field ($\langle\psi\rangle = 0$), and one observes a "shorting" effect in the conductivity measurements due to small fluctuating regions going superconducting. But, for $T < T_c$ the problem is quite different. Now a pair-field exists ($\langle\psi\rangle \neq 0$) and fluctuations are only slightly disturbing the whole field. Then, regions going normal due to fluctuations in the pair field are hard to observe amidst the whole superconducting field. It is for this reason that the treatment of fluctuation

theory is generally concerned with fluctuations above T_c , and why the theories, as well as the experimental data, are not as complete below T_c .

Historically, work began in looking at the conductivity of dirty superconducting films. The wide transitions observed were at first believed to be due to sample inhomogeneities, where one was observing an averaging of many T_c 's in the transition. But, at the same time, theoretical work began that predicted observable fluctuation effects outside the critical region, even in pure superconductors. These calculations agreed with the widened experimentally observed transitions. Fluctuation effects have been observed in the conductivity (σ), in the diamagnetism (χ_{dia}), and in the superconducting tunneling (I_c) of a superconductor above its MFT transition temperature. Approximation schemes used in the calculations lead to good agreement between fluctuation theory and experimental results near the transition. The overall effect of enhanced fluctuations is to widen the predicted critical region (as large as $\epsilon_c \sim 10^{-3}$ for dirty, 2-D films) and change the nature of the measurement and shift the transition temperature to a lower value.

Figure 3 shows the fluctuation effects on the heat capacity of a superconductor as calculated by Grossman, Richter, and Wissell.⁹ Notice not only the increased distortion of a perfect B.C.S. discontinuous jump in the heat capacity, as one widens the critical region, but also notice how the effect is appearing at a

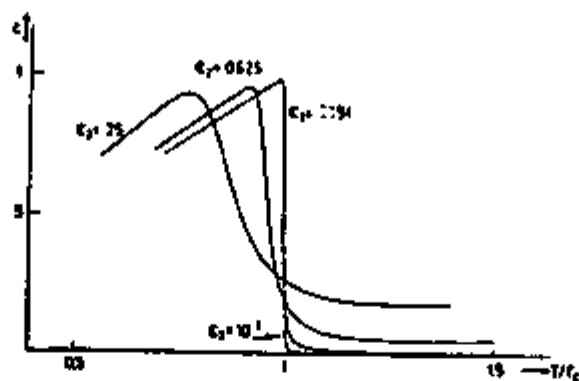


FIG. 2. Specific heat of films for various transition widths ϵ_p .

Figure 3. (from Ref. 9)

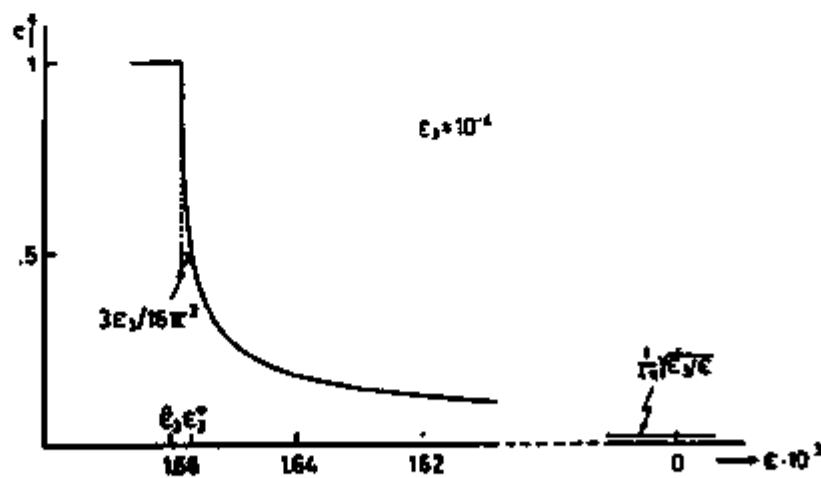


FIG. 1. Bulk specific heat in Hartree approximation.

Figure 4. (from Ref. 9)

lower transition temperature for wider critical regions (ϵ_c). Also notice the "rounding" or precursor nature of the effect as one approaches the transition from above. This is similar to the form that the other measurements (σ , χ_{dia} , I_c) of fluctuations show (i.e., precursive entrance into divergent behavior).

As stated earlier, much work has been done in looking at fluctuation effects in the superconducting transition, through σ , χ_{dia} , and I_c . But, because of the experimental difficulties, not much work has been done to look at the heat capacity fluctuation effects. Before embarking on the theoretical nature of these effects, one should revise the estimates of the critical region with enhanced fluctuations to see if the experiment is possible.

Estimation of the Critical Region

As stated earlier, the estimation of the critical region is a somewhat arbitrary procedure. It basically involves estimating where a particular calculation breaks down as $\epsilon (= \frac{T-T_c}{T_c})$ gets smaller. Thus, if one made an approximation of neglecting the 4th order term in the free energy ($|\psi|^4$), then the critical region could be defined as when the omission of the 4th order term no longer becomes possible ($|\psi|^4 \sim |\psi|^2$) relative to the lower order terms. Depending upon the particular calculation, most estimates of the critical region can vary by an order of magnitude or so. Ferrell's⁶ estimates - for the above mentioned

breakdown are listed below for the dirty superconductor case only. The estimate is for aluminum, chosen because of its ease in film preparation and moderate critical temperature, and because of the extensive previous work reported in the literature on dirty aluminum.

Dimension	Quantity	Numerical Value for dirty Aluminum ($\xi \sim 10 \text{ \AA}$)
3-D	$\epsilon_c \sim \frac{1}{(k_F \xi_0)} \frac{1}{(k_F \xi)^3}$	10^{-8} bulk
2-D	$\epsilon_c \sim \frac{1}{(k_F L)} \frac{1}{(k_F \xi)}$	10^{-5} (1000 \AA thick = L)
1-D	$\epsilon_c \sim \frac{1}{(k_F L)^{4/3}} (\xi_0 / \xi)^{1/3}$	10^{-3} (1000 \AA diameter = L)

Here k_F is the Fermi momentum ($\sim 1.75 \times 10^8 \text{ cm}^{-1}$), ξ_0 is the Pippard intrinsic coherence length ($\sim 1.6 \times 10^{-4} \text{ cm}$), and L, ξ were defined earlier. For a film, one can use the fact that $\sigma = \frac{Ne^2 \ell_{\text{eff}}}{m v_F}$ to get $\epsilon_c = 0.43 \times 10^{-5} R_{\square}^N$ for aluminum films (see ref. 10) where R_{\square}^N is the normal resistance of the film per square. These estimates show that only in the film, and wire experiments would one expect to observe critical behavior. But, it should be pointed out that this does not rule out observable fluctuation behavior for regions much wider than ϵ_c , ($\epsilon > \epsilon_c$) as long as the inhomogeneities are small ($\epsilon_{\text{inhom.}} < \epsilon$). One would then expect it to be possible to see a fluctuation enhanced transition in a dirty aluminum film.

Theoretical Predictions

To study critical phenomena in superconductors, an experiment was done in dirty aluminum films. The characteristics of the films which were studied, were the electrical conductivity and heat capacity. The conductivity was studied only as a guide to the transition properties of the films and to relate results to other work in the literature. The real interest was in the heat capacity in the vicinity of the transition. The heat capacity is a static thermodynamic property related to the energy density-energy density correlation function $\langle (\delta\psi^2)(\delta\psi^2) \rangle$ since $F \propto \psi^2$ and where now ψ will be used for Δ).⁶ The conductivity is a dynamical transport property related to gradients in the order parameter correlation function $\langle (\nabla\psi \cdot \psi')(\psi' \cdot \nabla\psi) \rangle$.⁶ One would not necessarily expect these two properties to have the same temperature dependence in the transition region. If one considers the fact that the aluminum films are quite granular, and intergrain tunneling is included in the conductivity as an effective electron mean free path, one would even expect less similarity. Also, as pointed out earlier, the conductivity is a measurement of a property of the order parameter that is not symmetric about the transition, whereas the heat capacity has some symmetry to its behavior. It is only when one considers that large fluctuations are present, and that the behavior of these properties is governed predominantly

by the size of the coherence in the system, that one could then expect the behavior for both properties to be related in the same way to the temperature dependent coherence length ($\xi(T)$).

The theoretical approach to calculating these properties in the transition region breaks down into essentially three methods. One can take the rather crude Ginzburg-Landau free energy presented earlier (F), and form the spatial average of the order parameter by computing a functional integral of the order parameter weighted by the Boltzmann factor. Thus, the free energy becomes in Fourier transformed momentum space:

$$\mathcal{F}(\psi) = \sum_{\vec{r}} e^{i \vec{q} \cdot \vec{r}} F(\psi(\vec{r})) \quad (7)$$

and then $\langle |\psi|^2 \rangle$, the thermal average of the order parameter is:

$$\langle |\psi|^2 \rangle = \text{Tr} |\psi|^2 = \frac{\int_{\mathcal{Q}} d\psi_{\mathbf{q}} |\psi|^2 e^{-\beta \mathcal{F}}}{\int_{\mathcal{Q}} d\psi_{\mathbf{q}} e^{-\beta \mathcal{F}}} \quad (8)$$

This is an integral equation similar to a Green's function propagator and usually involves a momentum cutoff in the integration. Because of the non-linear nature of the G-L free energy, one has to make approximations to F in order to solve for $\langle |\psi|^2 \rangle$. Then one can calculate properties of the system by using transport

or thermodynamic relationships of the order parameter to the properties calculated, which is similar to operating on the free energy explicitly. The problem with this method is that the G-L equation is phenomenological, and the absolute values of the coefficients are not known, so in the end one has to match to experiment by varying these parameters. It also is an inexact calculation in that one cannot solve the problem exactly, because of the diagrammatic perturbation techniques used in the integral equation.

The second approach to the problem is to go to the microscopic B.C.S. Hamiltonian and calculate the pair-field propagator in thermal Green's function analysis, and use diagrammatic techniques. Near T_c , as pointed out earlier, this is equivalent to the G-L approach, except it has a wider range of validity, as long as no approximation methods are used. Then the coefficients are known, and one usually has only one parameter in the theory (T_c). But, this problem too has to rely on perturbation methods, and one again is using approximation methods to handle the non-linear free energy. This method is in essence, the real understanding on a microscopic level, but it does not have the machinery to complete the predictions exactly.

The third method of approach is that of Ma¹¹ and Wilson using re-normalization techniques where they are concerned with an n-parameter field in a d-dimensional space. The problem is formulated in a general manner (expansion in powers of $1/n$), and then

one looks at a set of diagrams and concludes which are the important sets in certain limits of n , and d (for a superconductor $n = 2$). There is no perturbation theory used in the general formulation because one sums the diagrams, rather than explicitly evaluating them, so it has the possibility of solving the problem exactly. But it is mainly concerned with the regions of the transition where all quantities are related only to the size of the coherence length. It also cannot be solved at this point in time, without some use of perturbation theory to get around the mechanical difficulties (an example is ref. 15).

The calculation of properties of a superconductor in the transition region thus involves approximation schemes. This leads to the rather large range of predictions of the behavior of the heat capacity and the conductivity in 3, 2, and 1 dimensions both below and above T_c . Some author's calculations will leave out certain terms. Others will include them and show different behavior. But, neither have included all the terms, so it is difficult to show that a higher order term might not cancel off some effects of an earlier calculation. For this reason, the calculated predictions of interest are listed in Table 2A for the heat capacity and listed for the conductivity in Table 2B for all three values of d (dimension). The different approximations are shown, and some idea of the validity is given.

Above the transition, there is wide spread agreement with the conductivity calculations in all three dimensions. The 2-D result

Table 2A. Heat Capacity (C) Predictions for Dirty Superconductors (unless otherwise noted) $H = 0$. (Note: C' = excess heat capacity = $C_s - C_n$, where C_s, C_n are the super + normal state electron heat capacities and $C' = \Delta C$ at T_c in MFT.)

d (dimension)	Approximation	Authors (ref. #)	Fluctuation Region ($T > T_c$; $T < T_c$)	Critical Region ($\epsilon \sim \epsilon_c$)	Comments
3-pure	B.C.S. + Ladder Diagrams	Thouless (16) - 1960 (later done in dirty limit by Gor'kov and Batiyev)	* $C'/\Delta C \sim (T_c/T_F)^2 e^{-1/2}$ * $C'/\Delta C \sim (T_c/T_F)^2 \sqrt{2}(-\epsilon)^{-1/2}$	diverg.	Sum diverges for $T < T_c$
3-general 2nd order	G-L + $ \psi ^2$ in a Functional Integral	Levanjuk (17) - 1964	* $C'/\Delta C \propto \epsilon^{-1/2}$		Calculation for 2nd order compared to Quartz
3-pure	Q.M. Statistical Arguments using Green's Functions	Heller (18) - 1965	no singularity for superconductor		
3 0	microscopic B.C.S. + Green's Functions	Aslanov, Larkin (24) - 1968	* $C'/\Delta C \propto \epsilon^{1/2}$ * $C'/\Delta C \propto \epsilon^{-2}$		C, σ have same fluctuation regions
2	G-L Functional Integral-Hartree Approx. $ \psi ^2 + \psi ^2 < \psi ^2 >$	Marčelja, Masker, Parks (32) - 1969	* $C'/\Delta C \propto$ finite anomaly below T_c^{MFT}		
3 2	G-L Functional Integral but use thermodynamics on Free Energy itself.	Ferrell (6) - 1969	* $C'/\Delta C \propto \epsilon^{-1/2}$ * $C'/\Delta C \propto \epsilon^{-1}$	diverg.	
3 2 1	G-L Functional Integral 1st order only	Grossmann, Richter (29) - 1970	* $C'/\Delta C \propto \epsilon^{d/2-2}$ ** $C'/\Delta C \propto (-\epsilon)^{d/2-2} (\sqrt{2})^{d-2}$		

Table 2A (continued)

d (dimension)	Approximation	Authors (ref. #)	Fluctuation Region ($T > T_c$; $T < T_c$)	Critical Region ($\epsilon \sim \epsilon_c$)	Comments
1	Exact solution (like anharmonic oscillator)	Marčič (31)-1971 Sunther, Gruenberg (12)-1972	* $C'/\Delta C$ exact **	finite-slight bump	
3 2 1	G-L Functional Integral-Hartree ($ \psi ^4 + \langle \psi ^2 \rangle \psi ^2$)	Sunther, Gruenberg (13)-1972	* $C'/\Delta C = (1 + [\epsilon_{0L}/\epsilon(T)\epsilon_c]^{1/2})^{4-d} - 1$ **	no bump	$\epsilon_c \sim 9 \times 10^{-3} \frac{e^2}{4\pi} \times \frac{R^2}{k}$ Agree with Z+M
0	G-L-neglect $ \psi ^2$ but retain $ \psi ^4$	Parkinson (26)-1972	* $C'/\Delta C$ a 1-D exact but more complicated form		Hartree Approx. over estimates fluctuation effects
1 2	G-L Functional Integral Hartree $T > T_c$ Hartree-Fock $T < T_c$ (screened)	Bray, Rickayzen (14)-1972	* $C'/\Delta C$ d-D exact almost ** * $C'/\Delta C$ of finite anomaly **	should peak in 2-D	Use momentum cutoff. Do not agree with Z+M experiments results
1	G-L Functional Integral. HQ induces 1-D in 3-D. Hartree Approx.	Hassing, Hake, Barnes (27)-1973	* $C'/\Delta C$ a 1-D exact solution modified by R (ref. 8)		
3 2 1	Calculate Partition Function Functional-Integral B.C.S. Hamiltonian, SCF of $ \psi ^4$ in Hartree approx.	Hassing, Wilkins (28)-1973	* $C'/\Delta C \propto \epsilon^{d/2-2}$ Similar for 2-D, 1-D	finite in 3-D But a ϵ^{-1} No peaking	Only 3-D has Phase transition, does not quite agree with exact in 1-D
2	Renormalization G-L field Hartree approx. including screening	Scalapino, Ferrall, Bray (15)-1973	* $C'/\Delta C$ a Hartree of ref. 13 ** including screening gives peak		Don't agree with Z+M

Table 2B. Conductivity (σ) Predictions for Dirty Superconductors ($H=0$)
 (Note: σ' excess conductivity = $\sigma - \sigma_n$; where σ_n = normal state conductivity)

d (dimension)	Approximation	Authors (ref. #)	Fluctuation Region ($T > T_c$ to $T < T_c$)	Critical Region ($T \sim T_c$)	Comments
3 2 1	BCS + Green's Functions	Aslamazov, Larkin (23,24) -1968	$\sigma'/\sigma_n \propto \epsilon^{d/2-2}$		
3 2	BCS + Green's functions	Maki (25)-1968	$\frac{\sigma'}{\sigma_n} \propto \epsilon^{-1/2} + \frac{\sigma'}{\sigma_n} \propto \epsilon^{-1/3}$ diverges (Thompson fixed up with momentum cutoff).		Use SCF for spectrum in critical region
3 2 1	Kubo-formula and scaling arguments in $\xi(T)$	Kadanoff, Laramore, (20)-1968	$\sigma'/\sigma_n \propto \epsilon^{d/2-2}$	$\sigma'/\sigma_n \propto (\frac{\epsilon}{\epsilon_c})^{-1/3}$ for 3-D	Many assumptions in arguments
2			$\sigma'/\sigma_n \propto (\frac{\epsilon}{\epsilon_c})^{1/2} \exp(-\epsilon/\epsilon_c)$		
3 2 1	T.D.G.L. Phenomenological + Complex order parameter neglect $ \psi ^4$ (harmonic approx.)	Schmidt (21)-1968 Schmidt (22)-1970	$\sigma'/\sigma_n \propto \epsilon^{d/2-2} K(\omega)$ $\sigma'/\sigma_n \propto \epsilon^{d/2-2} K(\omega)$		$K(\omega), K'(\omega)$ include the fluctuation spectrum
3 2	B.C.S. in Self-consistent Field (S.C.F) using diagrammatic techniques	Teuzuki (19)-1969	$\sigma'/\sigma_n \propto \epsilon^{-1/2}$ $\sigma'/\sigma_n \propto \epsilon^{-3}$	$\sigma'/\sigma_n \propto \epsilon^{-1/3}$ $\sigma'/\sigma_n \propto \epsilon^{-1}$	
3 2	G-L Functional Integral works on Free energy	Ferrelli (6)-1969	$\sigma'/\sigma_n \propto \epsilon^{-1/2}$ $\sigma'/\sigma_n \propto \epsilon^{-1}$		Expects σ, ξ to have same temperature dependence

Table 2B continued

d (dimension)	Approximation	Authors (ref. #)	Fluctuation Region ($T > T_c$; $T < T_c$)	Critical Region ($c = c_c$)	Comments
2	Microscopic B.C.S. including lifetimes for normal + supercond. states	Patton (30) - 1971 (full experimental comparison in ref. 33)	$\sigma/\sigma_n = \frac{c}{T} \left[1 + \frac{2}{T - T_c} \ln\left(\frac{c}{8}\right) K \right]$		No transition in 2-D, 1-D
3 2 1	G-L Functional Integral with B.C.S. Hamiltonian in SCF of $ \psi\rangle$ in Hartree	Messing, Wilkins (28) - 1973	$\sigma/\sigma_n \propto n^{d/2-2}$ * $n = c + K_T > T_c$ ** $n = c + K_T < T_c$		Below T_c^{NFT} 2-D, 1-D go to 0-D. No phase transition in 2-D or 1-D
3 2 1	G-L Functional Integral Hartree Approx.	Mackay, Maréchal, Parks (32) - 1969	* $\sigma/\sigma_n \propto T \Delta T_c^{*} < T_c^{NFT}$ * $\sigma/\sigma_n = \frac{A.L.}{T_0} c^{-1}$ ** $d/\sigma_n \propto \exp\left(\frac{cT_c}{T}\right)$ ** $\sigma/\sigma_n \propto (-c)^3$		

(generally associated with the work of Aslamazov and Larkin)

for the excess conductivity is:

$$\sigma'/\sigma_n = \tau_0^{A.L.} \epsilon^{-1} \tau_0^{A.L.} = 1.52 \times 10^{-5} R_{\square}^N \quad T > T_c \quad (9)$$

The Maki and Thompson corrections are for films with long electron mean free paths, and thus include the electron-pair interactions. Patton's work is in agreement with the largest amount of experimental work, but it still is valid only outside the critical region. Below T_c , there are various forms of exponential falling off that can be fit to experiments only for $T \ll T_c$. There is really no clear understanding of the conductivity very near T_c , or below, and generally there is accepted agreement in the A.L. result above T_c . There is some agreement that 2-D and 1-D systems do not exhibit a phase transition, but just an inexact superconductivity, with a very large (but not infinite) conductivity. There is also some agreement that the conductivity and the heat capacity should have the same temperature dependence. Table 2B is by no means a complete list, but only an illustrative table of the many ways theorists can get similar or different answers. It would be expected that dirty aluminum films would at least follow the A.L. result above T_c .

The calculations of Table 2A show some of the earlier work predicting a divergence in lower order perturbation theory. It maybe is an artifact of a theory that there is a divergence. That is,

if an approximation is used in the calculation, it breaks down close to T_c , and the calculation diverges. This does not mean that the full calculation would necessarily diverge. Thus, in some ways the precursive nature of the heat capacity prediction is a property of the approximation. Later work includes better approximation methods for higher order terms. These results predict different types of finite anomalies in 2-D. The 1-D problem can be solved exactly, and is used as a check on the approximation methods in 2-D. Figure 4 shows the precursive nature of a 3-D calculation, with possibly a finite anomaly at the reduced $T_c(\epsilon_3 = \epsilon_c)$. Figure 5 shows the exact 1-D calculation, with a slight bump in a smooth transition over to the B.C.S. jump. Figure 6 shows one prediction of the 2-D result compared to an experiment (Zally and Mochel referred to as ZM) to be discussed later. Figure 7 shows a finite anomaly prediction in 2-D that is in disagreement with the work of ZM, where A is a momentum cutoff. In general, all the calculations predict above the transition:

$$C'/\Delta C = \tau_0 \epsilon^{-1} \quad \text{where}$$

$$\tau_0 \sim \tau_0^{A.L.} \quad \text{for } T > T_c$$

$$\tau_0 = .69 \tau_0^{A.L.} \quad \text{for the calculation of ref. 6}$$
(10)

This exhibits a precursive nature similar to the conductivity. But, the difference in the predictions is for the critical region, where some theories predict a peaking of the heat capacity above the B.C.S. jump, and others predict a monotonic transition

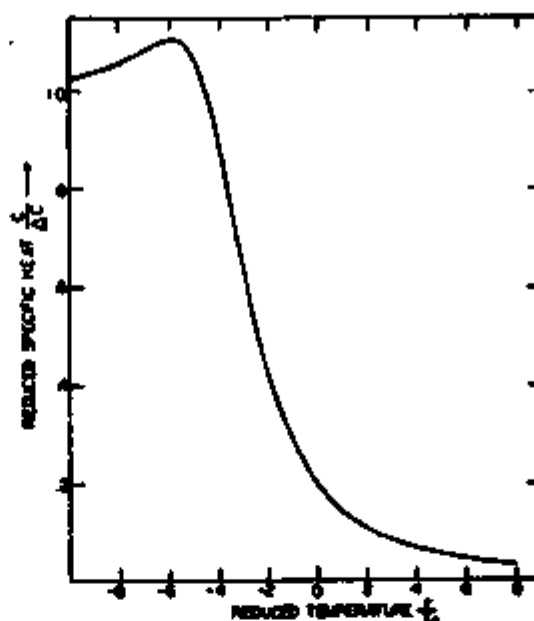


Fig. 1. Specific heat versus temperature. The specific heat, in units of the bulk specific heat discontinuity, is plotted against the reduced temperature $T/T_0 = (T - T_0)/T_0 - T_0$. No peak appears in the Hartree approximation [1] nor in recent specific heat data [3] on thin films which agree well with the Hartree approximation.

Figure 5. (from Ref. 12)

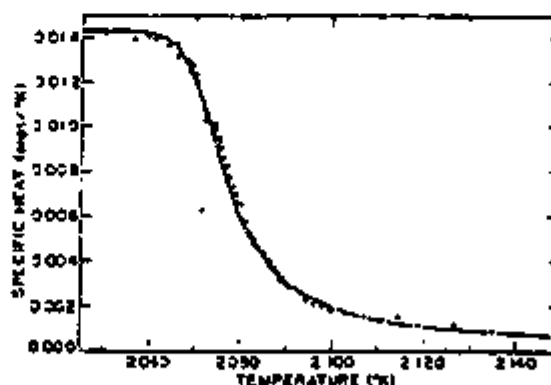


FIG. 1. Comparison of theory with experiment. The dots are the experimental values of the specific heat of a 1350 Å sample of $\text{BiSb}_{0.99}$ plotted against temperature. The solid curve is the theoretical curve of specific heat versus temperature determined by the equation $f(C/0.0143) = (0.0143/C - 1) - \ln(0.0143/C - 1) - 322.6/C - 659.3$.

Figure 6. (from Ref. 13)

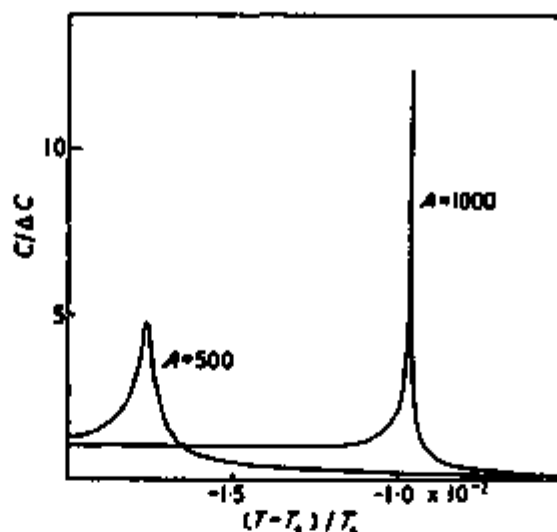


Figure 4. Specific heat in two dimensions for $A = 500$ and $A = 1000$.

Figure 7. (from Ref. 14)

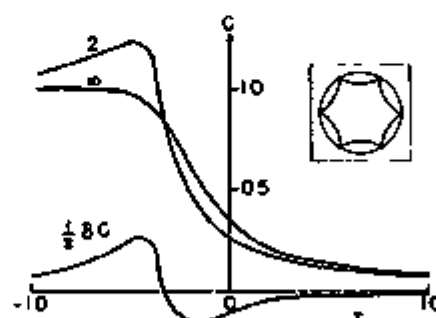


FIG. 1. Specific heat C of a two-dimensional Ginzburg-Landau model versus reduced temperature τ . C is normalized to unity as $\tau \rightarrow -\infty$. The curve labeled " ∞ " shows the specific heat per component of an n -component model in the Hartree limit, $n \rightarrow \infty$. The curve labeled "2" shows the first-order screening approximation for $n=2$. The difference between the two curves is $\frac{1}{2}\Delta C$, the screening correction, and is shown by the bottom curve. The Feynman graph shown in the upper right-hand inset is a typical ring diagram included in the screening correction.

Figure 8.

Heat Capacity in 2-D including screening approximation terms (graph #2). (from Ref. 15).

to the B.C.S. value. The calculations involve different forms of a Hartree approximation. The work shown in Figure 7 includes the screening terms in the Hartree approximation. The technique of extending perturbation theory far into the critical region, where it is expected to break down, is quite risky. In fact, this method is questionable, even in conductivity work, where the agreement with experiment is quite good.⁶ As pointed out earlier, the renormalization technique is the best approach. Figure 8 shows the results of using a renormalization approach, but due to the difficulty of the problem, perturbation theory was used. The curve labeled " ∞ " is the Hartree result equal to that of Figure 6. But, by including higher order terms, additional contributions give the result labeled "2", which shows a peak in 2-D. If one included even higher order terms, one might expect a "cusp-like" feature to appear (at the peak of Fig. 6). This work also is in disagreement with the work of ZM.

Thus, the heat capacity should exhibit a behavior similar to the excess conductivity above T_c in 2-D, but its behavior near T_c is not understood. One would expect the 3-D system to exhibit a singularity like that observed in other 3-D phase transitions (i.e., LHe^4). But due to the narrow width of the critical region in 3-D (ϵ_c) and the rather large samples used, one would expect inhomogeneities to broaden the results ($\epsilon_{\text{inhom.}} > \epsilon_c$). The 1-D prediction is an exact calculation, and because of the experimental difficulties, this problem has not been studied.

A 0-D experiment (dust) might be possible, but it is not quite understood theoretically. The 2-D problem is of greatest interest because of the different predictions. Some predictions are for a full phase transition and a divergence, as in 3-D. Other predictions are for no phase transition, but a definite non-monotonic peaking to occur near T_c . Finally, other predictions indicate no peaking at all. Because of these predictions, the experiment was carried out on a 2-D system where one is interested in, 1) the behavior above T_c , where one expects a precursive nature, and 2) whether or not a peaking occurs in the transition to the B.C.S. jump.

Chapter 3. Previous Experimental Work

The experimental work in measuring fluctuation effects in the superconducting transition is substantial. Some of the measurements of conductivity on aluminum films will be discussed in the appendix on sample preparation. However, there has been relatively little work done on looking for fluctuation effects in the heat capacity. This is most likely due to the difficulty of the experiment.

One of the early studies of fluctuation effects was that of Cochran.³⁴ In making an analogy to the work on the superfluid transition of He⁴, he looked at the heat capacity of bulk pure superconductors very near their transitions. Figure 9 shows the work of Cochran for the total heat capacity vs. temperature plotted for the bulk samples of Ta-II. The dots are the experimental data, and the dotted line and the continuous line are two theoretical curves. In analyzing his data, Cochran used a form for the heat capacity that had the BCS jump plus a diverging form for the bulk sample ($\epsilon^{-1/2}$). It is shown below.

$$C(T_C) = \Delta C_{BCS}(T_C) + \frac{\alpha}{T_C} |\epsilon|^{-1/2} \text{ where } \alpha \text{ is an arbitrary parameter.} \quad (11)$$

Then, because he was working in bulk samples, where one would expect an inhomogeneous system with multiple transitions, he formed an average of the individual heat capacities (eq. 11) associated

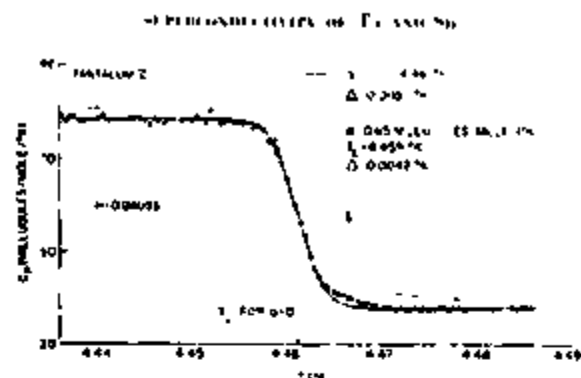


FIG. 9. Variation of the order parameter of Fe 330 S₂ for temperatures $\alpha < T_c$ were calculated from Eq. (5).

Figure 9. (from ref. #34)

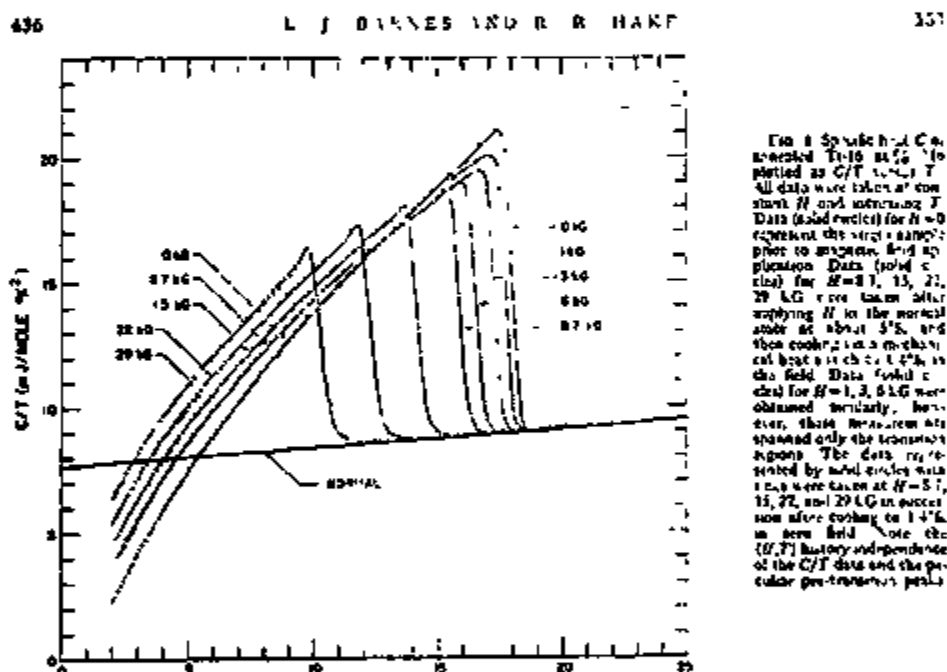


Figure 10. (from ref. #35)

with each transition. This average was weighted about a MFT T_c by a Gaussian-like function of the difference in transition temperature from the MFT value which is shown below:

$$C(T) = \int_{-\infty}^{\infty} \frac{1}{\sqrt{\Delta \pi}} \left[\exp - \frac{(T_c - T_{MFT})^2}{\Delta^2} \right] \left[\Delta C_{BCS}(T_c) + \sqrt{T_c} |\epsilon|^{-1/2} \right] dT_c \quad (12)$$

His best fit to the data was for $\alpha = 0$ and $\Delta = 3.2$ mK, which leaves out the precursor (the continuous line in Figure 9). The rounding or precursive nature of the data in going over to the BCS form is most likely due to the inhomogeneties broadening the transition. Cochran placed an upper limit on the entropy associated with a singularity in the heat capacity of the metals studied (Ta, Sn) as $\sim 10^{-3}$ J/mole K. Because of the expected width of the critical region ($\sim 10^{-12}$ K) for bulk pure samples, one can conclude that Cochran observed only MFT effects in an inhomogenous system.

More recently, Barnes and Hake³⁵ measured the heat capacity of bulk dirty samples of $Ti_{.84}Mo_{.16}$ in large magnetic fields. Figure 10 shows their results of the total heat capacity (divided by temperature) plotted vs. temperature squared. The normal BCS discontinuities are apparent. But, one also notices the reduction in the transition temperature (T_c) and the widening of the transition region with increasing values of applied magnetic field. This is in agreement with the magnetic field predictions of Lee

and Shenoy presented earlier. One should notice the rounding or precursive nature as the transition is approached, for the heat capacity measurements at higher magnetic fields. They also mention a possible fluctuation region as broad as 0.5K existing for their samples. In a recent paper, Hassing, Hake, and Barnes³⁶ reanalyze their previously mentioned work, using an extension of the previously discussed idea presented by Lee and Shenoy, where the magnetic field induces a reduction in the dimensionality of the system to enhance fluctuation effects. Using a Hartree approximation for the fourth order term, Hassing, Hake, and Barnes extend Lee and Shenoy's calculation through the transition region in a 1-D calculation of the heat capacity. Using a two parameter fit, their results are shown in Figure 11, where the excess heat capacity is plotted vs. temperature. They attribute the disagreement between theory and experiment in the value of ΔC_{BCS} as being related to the choice of the momentum cutoff used in the calculation. A more obvious problem is the rather wide transition regions observed ($\sim .4K$), even for a zero value of the magnetic field ($\sim .1K$). They cannot account for this with their present theory.

The problems in looking for fluctuations in the heat capacity of a bulk system are shown in the two previously mentioned experiments. One has a very narrow transition region (ϵ_c), and thus little experimental access to this region, even for enhanced transitions ($H \neq 0$, dirty systems). But a more limiting problem is

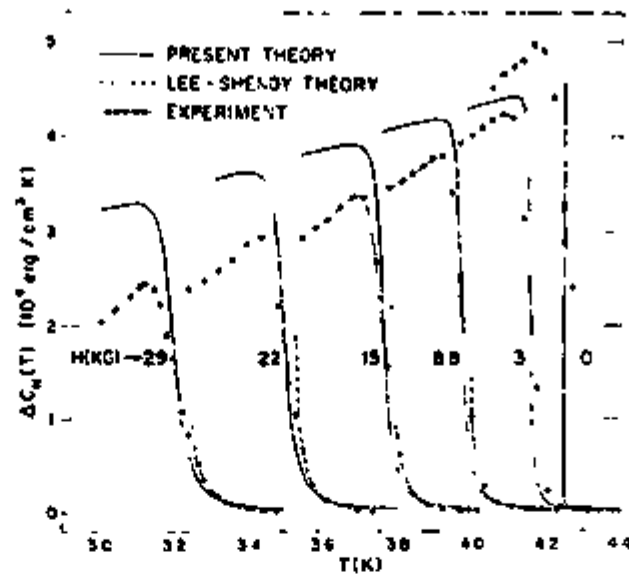


FIG. 1. Specific heat difference, $\Delta C = C_s - C_n$, versus temperature T for various values of applied magnetic field H , as given by the present theory, the theory of Ref. 3, and the data of Ref. 9. The dashed line (Lee-Sheny theory) merges with the heavy solid line (present theory) for T well above $T_{c2}(H)$. The zero- H curve given in the present theory stops abruptly at $\Delta C = 1.43C_p$ at a slightly shifted zero- H transition temperature $T_c = 4.2456$ K (critical exponent $\alpha = -1$; see Ref. 6). The data points are the observed superconducting-state specific heat C_s values minus the normal-state specific heat $C_n = \gamma T + \beta T^3$, where γ and β were determined by a least-squares fit for data taken in applied fields sufficient to quench superconductivity. All theoretical curves have been scaled so as to center the transitions at the experimental $T_{c2}(H)$ as discussed in the text. The experimental values of $T_{c2}(H)$ for $H = 20, 24, 15, 8, 3,$ and 0 kG are, respectively, 3.316, 3.509, 3.772, 3.980, 4.159, and 4.246 K, obtained by an entropy-fitting procedure (see Ref. 9, Table I, footnote c). The $H = 0$ data were taken without compensation of Hart's magnetic field.

Figure 11. (from Ref. #36)

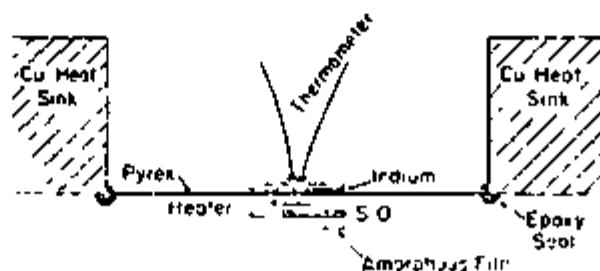


FIG. 2. Side view of sample holder and substrate

Figure 12. (from Ref. #38)

that of obtaining a bulk homogeneous sample. One can test for alloy concentrations, etc., but a more consistent measurement of the inhomogeneities of the system is rather difficult (i.e., the sample resistance is already quite small for $T > T_c$ in a bulk system due to its geometry). Thus, one would expect inhomogeneities to have a large role in the broadening of the transition of bulk samples.

In a 2-D system, where one is working with a thin film, it is much easier to obtain and verify homogeneous samples, that one can use to study the heat capacity of the superconducting transition. Zally and Mochel^{37,38} measured the heat capacity of a very dirty thin film. Their experimental configuration is shown in Figure 12. It consists of an amorphous $\text{Bi}_{.4}\text{Sb}_{.6}$ film which is flash evaporated at 4K onto the calorimeter. The calorimeter consists of a 100 Å constantan heater, separated from the film by a 5000 Å SiO film, and attached to the lower side of the glass plate. On the back side is a Ge chip thermometer epoxied to a 5000 Å In film. A.C. Calorimetry is used in measuring the heat capacity (see A.C. Calorimetry Appendix). The low thermal diffusivity of the glass creates a long thermal time constant from the calorimeter to the isothermal block, but also creates a long internal time constant for the calorimeter (i.e., the time constant to travel in the vertical direction of Figure 12), which limited the work to heating frequencies of less than 200 Hz (typically $2f = 60$ Hz). Figure 13 shows the experimental configuration in the plane of the glass

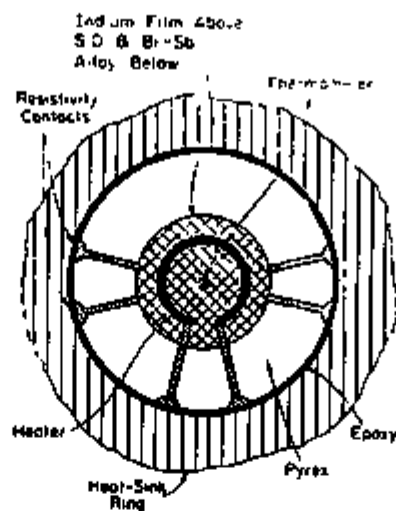


FIG. 3. Top view of sample holder and substrate showing heater and thermometer configuration, evaporated resistivity contacts, Pyrex window, and alloy dot.

Figure 13. (from Ref. #38)

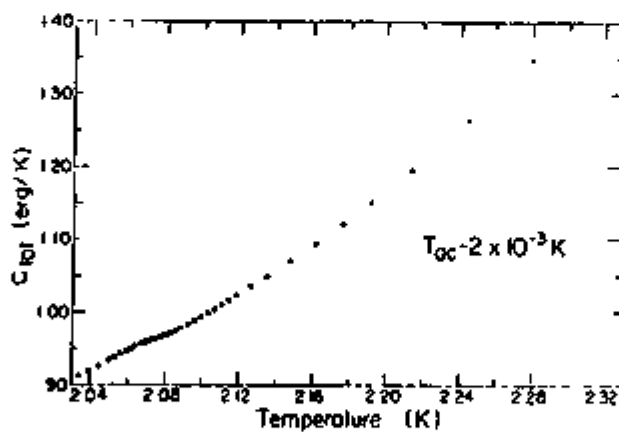


FIG. 4. Data for sample No. 13. The heating beam controlled to heat capacity of the total assembly + temperature.

Figure 14. (from Ref. #38)

plate (2-3 μm thick). It also shows the non-uniform current paths existing for the resistivity measurements of the film. It should be noted that these glass plates are actually glass "bubbles", so that there is some curvature associated with the film plane, and thus a non-uniformity in thickness. One should also notice the inductive nature of the heater configuration, which could lead to electrical coupling between the film and the Ge thermometer. Figure 14 shows the raw data of the total heat capacity and the calorimeter. The slight bump at 2.06K is the superconducting transition of the film. To extract the electronic heat capacity from the raw data, Zally and Moche1 used a four parameter fit that forced a zero excess electronic heat capacity for $T \gg T_c$ and a superconducting excess heat capacity for $T \ll T_c$ where the excess is $C' = C_{es} - C_{en}$. Then the excess heat capacity of the film was calculated from the equation below.

$$C'_{\text{film}} = C_{\text{tot}} - (AT + BT^2 + CT^3 + DT^4) \quad (13)$$

Because the overall experiment was only accurate to 1 part in 1500, and the heat capacity of the calorimeter was ~ 1 erg/K, and the BCS jump of the film was $\sim .01$ erg/K, the measurements on the film were accurate to only 10%. In fact, they state in their paper that shuttling the fitted parameters around can drastically change the form of the derived heat capacity of the film. Their excess heat capacity is shown in Figure 15, where the resistive transition is also shown. It should be noted that

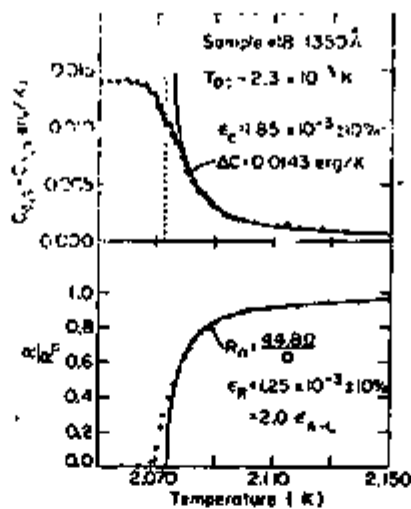


FIG. 9. Resonance and heat-capacity transitions for 1350-Å film - 63 at. % Sb film. Upper curve: fit to $C_{015} - C_{015}^0$. Lower curve: fit to $R = A_0 B + e_0 / \omega^2$. Dashed curve: mean-field result.

Figure 15. (from Ref. #38)

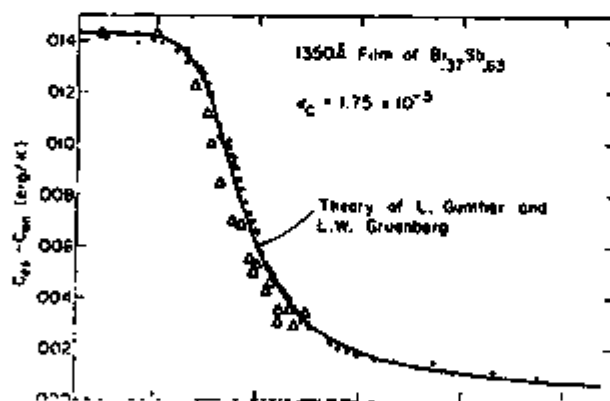


FIG. 10. Two-parameter fit between the Hartree-like theory of Gunther and Greenberg and the fluctuation heat capacity in a 1350-Å film of $\text{Bi}_{47}\text{Sb}_{53}$. The resulting standard deviation is less than 3% but the width $\epsilon_c = 1.75 \times 10^{-3}$ is three times larger than expected on the basis of resistivity measurements. The open triangles are measurements taken with ΔT_{90} five times smaller (0.3 mK) than the ΔT_{90} for the solid points. There is only a slight sharpening of the transition due to the improved temperature resolution.

Figure 16. (from Ref. #38)

the circular geometry of the film presents problems in calculating R_{\square}^N (the normal sheet resistance), but these problems are easily solved (see Sample Preparation Appendix). Also, the upper side of the calorimeter had LiH_e^4 on it to keep the substrate cold during evaporation, and although this was pumped out during the measurements, it never was totally removed. The resistive transition is off by a factor of 2 from the A.L. theory. Since these films had a mean free path (ℓ) of only $.8\text{\AA}^{0.37}$, one would expect quite good agreement with the A.L. theory for the resistive transition. But this mean free path was only estimated from the conductivity, and never independently measured. Because of the relatively few points taken in the resistive transition in the region where A.L. should work, it is hard to accept the fact of this film's conductivity being in agreement with a homogeneous transition in A. L. theory. Finally, the results of Figure 15 are used in a two parameter fit to get the remarkable agreement to the theory of Gunther and Gruenberg, shown in Figure 16. The true error bars on the curve are $\pm \Delta T_{A.C.}$ on the x axis, and $\pm C_{TOT}/1500 \sim .0007$ ergs/K on the y axis. This is on the order of the size of the triangles shown in Figure 16. Thus, one notices a considerable scatter in the smaller amplitude heating, and a remarkable agreement for the larger amplitude heating, where the error bars should be larger. Zilly and Mochel claim not to have observed any peak in the heat capacity as predicted, and to be in complete agreement with the theory of Gunther and Gruenberg mentioned earlier. Their observation of an ϵ^{-1} behavior in the heat capacity is consistent with

fluctuation theory. Their results show the difficulty of measuring the heat capacity of a thin film by conventional methods. But, their use of a four parameter fit to extract the film's heat capacity is an arbitrary approach. When one adds to this another 2 parameters to get agreement to the theory, the final results are not surprising at all. A true understanding of the heat capacity in 2-D will only come from results that are not forced to a particular form by multiple parameter fitting, and where control of the experiment is to a high enough degree that one can readily dismiss questions of electrical coupling and background LHe^4 coming into the measurement. It is also necessary to make a final comment on their method of presenting data. In their first paper (ref. 37), they compare the widths of the resistive transition (ϵ_R) and the heat capacity transition (ϵ_C) to theory by plotting the ratio of these widths vs. the film's thickness. The data is badly scattered and only a weak conclusion can be drawn. In their second paper (ref. 38), they plot the same numbers as independent entities to the inverse power (ϵ_R^{-1} , ϵ_C^{-1}) vs. film thickness. This somewhat obscures the differences between the numbers and gives a more consistent view to the data. There is no physical reason* why one plot is better than the other, and thus by choosing the better "picture", they are somewhat misleading the reader.

* Since ϵ_C , $\epsilon_R \propto \frac{1}{d}$, d being the film's thickness, it will cancel in a ratio plot, and remain linear in an inverse plot.

There have been no other experiments, to the author's knowledge, to measure fluctuation effects in the superconducting transition by measuring the heat capacity of a thin film. There is some work being done to measure the heat capacity of thin films that is worth mentioning. Greene, King, Zubeck, and Hauser³⁹ have used a very cleverly designed calorimeter to measure the heat capacity of granular aluminum films. They employ a Silicon chip calorimeter that has a heater and thermometer doped into it. The chip is suspended from an isothermal copper block by alloy wires to provide the correct time constants for A.C. Calorimetry. They shine a chopped laser beam (26 Hz) onto the calorimeter to provide the A.C. heating. Measurements were made on a 25 μm thick aluminum film (1.1 mg) sputtered onto the surface of the silicon chip. The film's grain size was on the order of 5000 \AA (as determined from SEM measurements) and its heat capacity transition was widened due to inhomogeneous broadening. One can infer from their measurements that any singularities in the heat capacity would have to have an entropy of less than the 5% agreement they get between the superconducting and normal state entropies. They also measured a free standing granular aluminum film of similar thickness (1.6 mg), with a thermocouple thermometer spot welded to the film. This film gave results similar to the sputtered film. There is one other group⁴⁰ that is measuring heat capacities of thin films that is not looking for fluctuation effects. They have constructed a calorimeter from Bi-Ag thermocouples and a luminescent diode with their films supported on a

colloidal substrate. There is a possibility of this scheme being useful for fluctuation measurements in thin films, but they have not reported using it for such measurements.

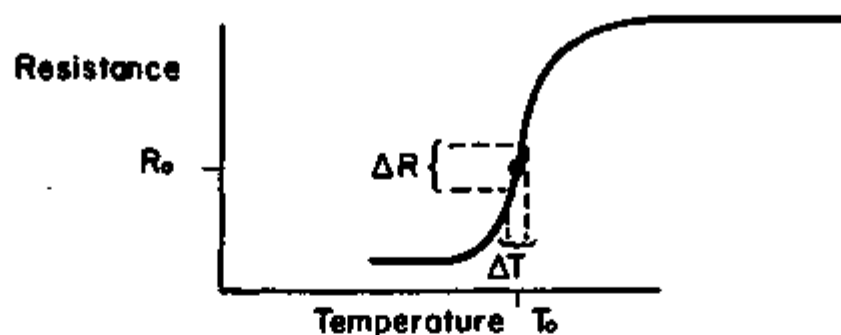
Thus, the experimental work to measure fluctuation effects in superconductors by measuring the heat capacity in the transition region is sparse. The results of measurements made in bulk systems are hindered by problems in obtaining homogeneous samples and accessible critical regions. There are no reported heat capacity measurements in 1-D (wires). The only work done in 2-D that is possibly in a homogeneous system and in the lower dimensional limit (the 25 μm films were probably too thick) is that of Zilly and Moche1. Although their work is in partial agreement with theory, there are considerable doubts about their abilities to observe such small heat capacities buried amidst the heat capacity of a relatively large calorimeter. Thus, the previous experimental work implies the difficulties of measuring the heat capacity in the transition region of a superconductor, and as yet, it has still left the theoretical understanding of the problem open to question.

Chapter 4. Experiment

Basic Method

Because the conventional experimental approach to the measurement of the heat capacity of thin films (as carried out by ZM) has inherent problems of temperature resolution and accuracy, unconventional techniques were used in this experiment. One unconventional feature was to use the superconducting film's resistive transition as a non-linear thermometer to measure the temperature of the film (first suggested by Ferrell⁶). The advantage of this method over the more conventional approach is that the thermometer in the calorimetric measurement is always in thermal equilibrium with the film, and it contributes no background heat capacity. A second unconventional feature was to use A.C. Calorimetry by heating the film optically with a modulated light source (see Appendix F). There is thus no contribution to the heat capacity measurement from a heater, and the heater and the film are also in thermal equilibrium for moderate A.C. heating frequencies (see Appendix F).

Figure 17 shows a resistive transition of a superconducting film. The film has been calibrated against a temperature standard such that for any value of resistance (R_0) of the film, one knows the corresponding temperature (T_0) of the film. Then if the film is heated with a power \dot{Q}_{abs} at a frequency $f=1/\tau_{heat}$, the film will experience a temperature rise ΔT in each cycle as a



$$C(T_0) = \left. \frac{\Delta Q}{\Delta T} \right|_{T_0} = \frac{\dot{Q}_{\text{obs}} T_{\text{heat}}}{\Delta R(R_0)} \quad \left. \frac{dR}{dT} \right|_{R_0}$$

Figure 17. Resistive Transition being used as a non-linear thermometer.

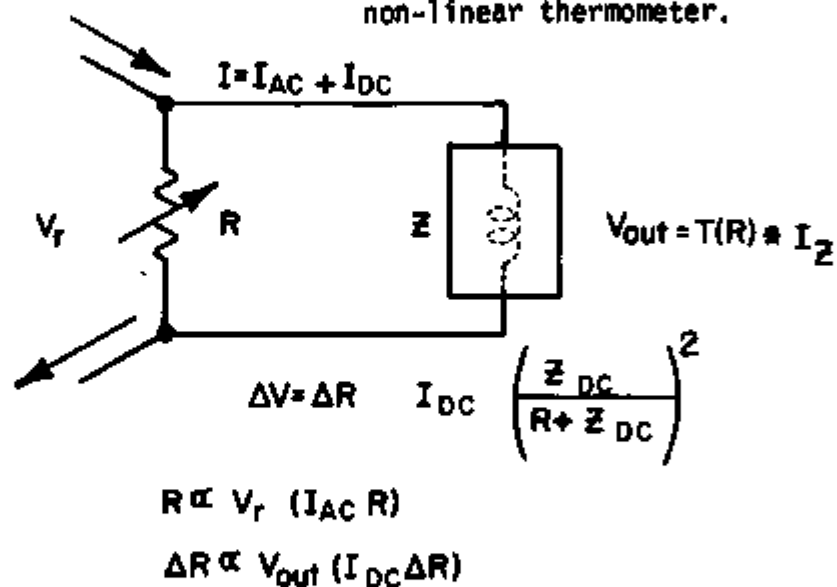


Figure 18.

Equivalent circuit used in analysis of the signal resulting from the optical heating (v^{heat}). With this analysis the voltage measured across the film V_r is proportional to the resistance R , and the voltage measured across the transformer (v^{out}) due to the optical heating is a functional form of the changing resistance ΔR .

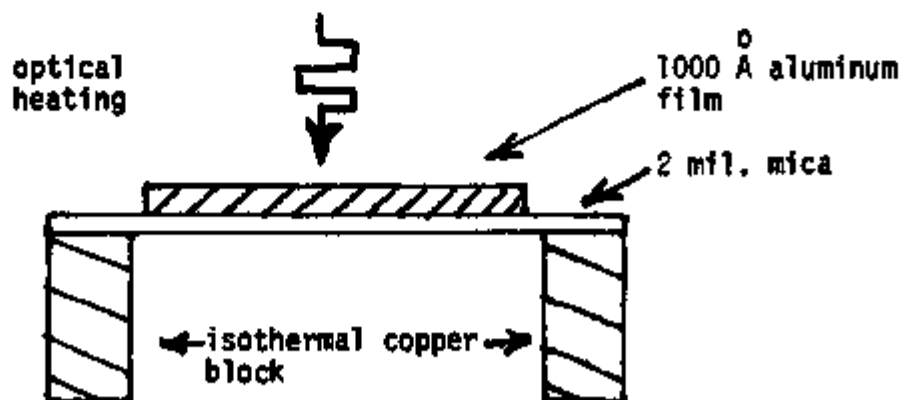
consequence of the energy put in during the cycle ($\Delta Q = \dot{Q}_{\text{abs}} \tau_{\text{heat}}$). This will cause a corresponding rise in the resistance of the film (ΔR). The heat capacity of the film at temperature T_0 can then be determined by the equation in Fig. 17, where $dR/dT|_{R_0}$ is the slope of the resistive transition at the point R_0 . The disadvantage of this method is that the thermometer only works in the transition region, and because of the non-linear relation between R_0 and T_0 , there is a considerable reduction in sensitivity near the beginning and end of the transition (dR/dT is small). Also, because the optical absorption in the film is not known exactly (\dot{Q}_{abs}), the absolute magnitude of the heat capacity cannot be obtained. The use of this method is warranted because the present theoretical interest in the heat capacity of a superconductor is in the transition region and the rather narrow predicted critical regions of temperature make a high level of accuracy necessary. With this method, one sacrifices the ability to relate measurements to known behavior outside the transition region for the extreme sensitivity and thermal resolution possible. Because of the need for accurately characterizing the superconducting phase transition by measuring the conductivity and heat capacity of a film, the advantages of the unconventional methods used in this experiment justify their use.

The basic procedure is to measure the changing value of the resistance of the film (ΔR) due to the optical heating (ΔT) as a function of the film's average resistance (R), which is varied through the whole transition by sweeping its temperature. This

is done at different frequencies and in an isolated environment. Then thermal grounding of the film to a thermometer is accomplished by adding He gas to the environment, and the film's resistance is calibrated against temperature. From this data, the heat capacity can be calculated in principle, using the equation of Fig. 17 for $C(T_0)$. The actual procedure is more complicated, but only because of the problems of a non-linear thermometer. However, no other alteration or fitting scheme is used to transform the data to the heat capacity.

Apparatus

The calorimeter consists of a 1000 \AA aluminum film on a 2 mil. mica substrate that is thermally grounded. The film is heated by light from a square wave modulated laser (see Appendix B). All measurements are made in a magnetically, electrically, and vibrationally isolated, thermally controlled environment (see Appendix C). A. C. Calorimetry is used in the measurement (see Appendix F). The basic apparatus is shown below:



The film behaves as if it were fully self-supported (see Appendices F and H). Thus, the fast thermal response time of the film allows equilibrium measurements, even at high optical heating frequencies (up to 20 KHz). An attempt was made to increase the sensitivity of the experiment at the ends of the transition by using a SQUID system, but this method was discarded due to problems that arose (see Appendix D). For more complete details, the reader is referred to the appendices.

Equivalent Circuit

The film's resistance is measured in a dynamical way (see Appendix H) where the film is biased from a low frequency (41.5 Hz) constant current source (see Fig. 19) at low current densities of $1 \rightarrow 5 \text{ A/cm}^2$. The phase sensitive detected voltage of the PAR-126 lock-in is scaled linearly in resistance at a temperature where the film is far above the transition region ($R=RN$). This scaling value for the resistance comes from a separate, four terminal A.C. bridge measurement (see Appendix A). This voltage signal is then used throughout the experiment as the value of the resistance. The out-of-phase contribution to the voltage is a small correction because of the low operating frequencies (see the discussion of the corrections in Appendix A).

The film is also biased from a constant D.C. current source at current densities of $10 \rightarrow 40 \text{ A/cm}^2$ (see Fig. 19). This current, in conjunction with the changing resistance ΔR , produces a voltage

signal ΔV that is also phase sensitive detected by a second lock-in (PAR #HR-8) with a reference that is coherent with the heating pulses ΔQ . Because of the low signal level and source resistance, a transformer (see Fig. 19, the AM-1 is set for $Z_{\text{input}} = 30 \Omega$, $Z_{\text{output}} = 147K\Omega$) is in parallel with the film to increase sensitivity and S/N ratio in the experiment. The combination of the transformer and varying resistance of the film creates a problem in determining the actual value of ΔR from the measured signal at the lock-in. The problem is that the transformer in parallel with the film has a low D.C. impedance, such that the D.C. current biasing the film is divided between the film and the transformer. The film's changing resistance as the temperature is swept through the transition, causes the division of the current to change during the measurement. Also, because the film's resistance is changing, the transformer relates the voltage on the film (V_f) to the voltage going into the lock-in (V_{out}) in a non-linear way.

To overcome this problem,⁴⁸ a general equivalent circuit is used to represent the real circuit (note there are low pass filters in the circuit of Fig. 19 that are not shown. See Appendix C). The equivalent circuit for the experiment is shown in Figure 18, where the film is in parallel with an unknown impedance Z and is biased by an A.C. and a D. C. current. Voltages that are detected by the PAR #HR-8 are presented by a transfer function $T(R)$ times the current I_Z in the impedance Z . Then, if the film is biased with a D.C. current, a D. C. voltage V_f appears across the resistance of the film. This voltage is given by the equation:

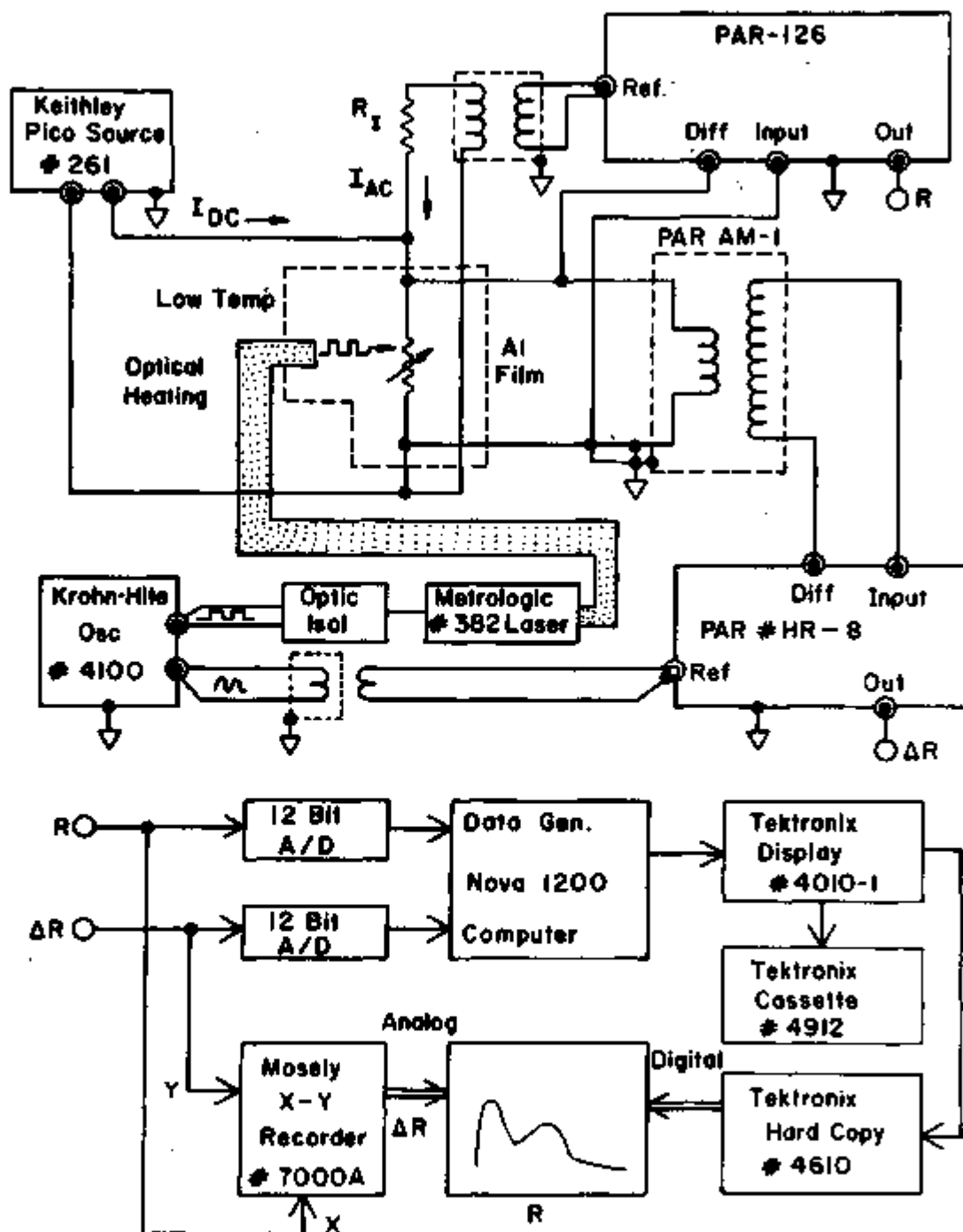


Figure 19.

Block diagram for electronic measurements including optical heating (via fiber optics), removal of electrical ground loops, and analog and digital recording and display systems. A direct comparison can be made between all analog data and recorded digital data. All chassis grounds are to a copper bus bar held at a true ground.

$$v_r^{DC} = \frac{I_{DC} R Z_{DC}}{(R + Z_{DC})}$$

Now if R is modulated by an amount ΔR , an A.C. voltage appears across the whole resistor and is shown below.

$$dV_r = \left[\frac{I_{DC} Z_{DC}}{(R + Z_{DC})} - \frac{I_{DC} R Z_{DC}}{(R + Z_{DC})^2} \right] dR, \text{ which reduces to:} \quad (15a)$$

$$\Delta V = I_{DC} \left(\frac{Z_{DC}}{R + Z_{DC}} \right)^2 \Delta R. \quad (15b)$$

This is contrasted with the more common method of including the modulation ΔR as a voltage source ($I_{DC} \Delta R$) in series with the resistance R . This is an incorrect model, since the voltage develops across the whole resistance R . Using the transfer function, eq. 15b becomes⁴²:

$$v^{Heat} \equiv \frac{T(R) \Delta V(\omega)}{Z(\omega)} = \frac{T(R) I_{DC}}{Z(\omega)} \left(\frac{Z_{DC}}{R + Z_{DC}} \right)^2 \Delta R(\omega) \quad (16)$$

v^{Heat} is the output of the lock-in detector measuring signals coherent with the heating. In order to determine the two unknown functions of eq. 16 ($T(R)$, $Z(\omega)$), two calibration measurements are also made. The film is first biased with an A.C. current at the frequency ω using the configuration shown in Figure 19. The voltage developing across the film is given by:

$$v^{film} \equiv \frac{I_{A.C.}(\omega) R Z(\omega)}{(R + Z(\omega))} \quad (17)$$

Then with the same bias, the signal is detected after passing through the transformer in the same manner as for the heating signal. The result is shown below:

$$v^{gain} \equiv \frac{I_{A.C.}(\omega) R T(R)}{(R + Z(\omega))} \quad (18)$$

Since the resistance of the source of these three signals (v^{heat} , v^{film} , v^{gain}) can change during the measurements, there are phase shifts in the detected signal. Thus, the in phase and out of phase components of the complex signal are detected and combined to give:

$$|v^{signal}|_R = \left[(v^{signal})_{0^\circ}^2 + (v^{signal})_{90^\circ}^2 \right]_R^{1/2} \text{ detected at } \omega \quad (19)$$

Thus by measuring $|v^{heat}|$ as a function of R (the 41.5Hz signal), and $|v^{film}|$ as a function of T (to be explained later), and $|v^{gain}|$ as a function of R , eqs. 16, 17, 18, 19, can be combined to form the equations below:

$$|v^{heat}| = \frac{|T(R)|}{|Z(\omega)|} \frac{|I_{DC}| |Z_{DC}|^2}{|R + Z_{DC}|^2} |\Delta R| \quad (20a)$$

Since Z_{DC} and I_{DC} are real, and $|v^{film}|_T$ is transformed to

$|V^{film}|_R$, $|V^{heat}|_R$ can be written:

$$|V^{heat}|_R = \left| \frac{I_{DC} Z_{DC}^2}{(R + Z_{DC})^2} \Delta R \right|_R \frac{(|V^{gain}|)_R}{(|V^{film}|_T)_R} \quad (20b)$$

The signal $|V^{film}|_T$ is measured as a function of T determined with a Germanium resistor (see Appendix A, H). Then, from the film calibration (R(T)) this can be transformed over to $|V^{film}|_R$. Figure 19 shows how the data is recorded by a sampling of the analog signals, and a cross check is made of this digital sampling to the analog recordings.

The film's resistance is varied through the transition by driving the temperature of the sample block (see Appendix C) with an increasing power such that the film takes about 31 minutes to traverse the transition region. The data is sampled every $\frac{1}{2}$ sec., such that 1020 pairs of data points are collected. Thus the following sets of data are recorded for one complete set used in a calculation.

$V^{heat} - \{R_i, V_i^{heat}(R)\} 0^{\circ}; 90^{\circ}$ 2 sets @ 1020 pt./set
at 1 pair/pt.

$V^{film} - \{T_i, V_i^{film}(T)\} 0^{\circ}; 90^{\circ}$ 2 sets @ 1020 pt./set
at 1 pair/pt.

$V^{gain} - \{R_i, V_i^{gain}(T)\} 0^{\circ}; 90^{\circ}$ 2 sets @ 1020 pt./set
at 1 pair/pt.

R(T) calib. - $\{R_i, T_i\} 0^{\circ}; 90^{\circ}$ 2 sets @ 1020 pt./set
at 1 pair/pt.

At ten ASCII characters per/number (floating point notation), this results in about 1.5 Megabits (8 bits/character) of stored data per run. The data is correlated in R and T to find ΔR from equation 20b. The correlation process involves a search for the closest point in the correlated parameter (R or T), and a linear extrapolation to obtain the correlated functional value. Due to the large sampling grid, this linear approximation is quite good. The functional correlation equation is shown below where f_i is the correlated value of f_j at point R_i .

$$f_i(R_i) = f_j(R_j) + \frac{(R_i - R_j) (f_j - f_{j\pm 1})}{(R_j - R_{j\pm 1})}$$

where the + sign is for $R_i > R_j$
 - sign is for $R_i < R_j$ (21)

The equivalent circuit of Figure 18 can be made much more complicated (including filters, capacitors, etc.), but in the range of frequencies used (2Hz + 20KHz), the basic form of the signal equation (eq. 20b) remains the same.

It was discovered that the discrete set of points for the two correction signals $|v_{gain}|_R$ and $|v^{film}|_R$ could be fitted to the functions shown below (notice that absolute values signs are omitted in the signal form of eqs. 17 and 18:

$$|V_{gain}|_R = \frac{\alpha_g R Z_g}{(R+Z_g)}; |V_{film}|_R = \frac{\alpha_f R Z_f}{(R+Z_f)}$$

Here α_g , Z_g , α_f , Z_f , are appropriate values for the unknown impedance Z and α is a scaling parameter for a particular frequency. $|V_{gain}|$, $|V_{heat}|$, $|V_{film}|$ are now measured in units proportional to the normal resistance (scaled when V_p is scaled to R_N), such that α is a dimensionless parameter. For a frequency of 1 KHz, the two functions are equal ($\alpha = 1.34$, $Z = 163 \Omega$). For the very low frequencies (2Hz) the functions differ slightly in the values of the parameters ($\alpha_g = 3.05$, $Z_g = 22.1 \Omega$, $\alpha_f = 1.34$, $Z_f = 16\Omega$). If a more complete model is used for the impedance $Z(\omega)$, the difference in the parameters can be explained for the low frequencies, but it in no way changes the final form of the heat signal in equation 20b. The value for Z_{DC} was measured directly ($Z_{DC} = V_{transformer}/I_{DC}$) and indirectly by a voltage division method. These results give a value of $Z_{DC} = 2.24 \pm .005 \Omega$. It should also be noted that the functions of eq. 22 are almost constant curves in R (due to the large Z value), and the parameter values are close to the measured values for the calibration ($\alpha \sim \frac{I_{AC}}{\sqrt{2}}$, $Z \sim Z_{transformer}$, $T \sim Z$) at the particular frequencies used. Thus, in this way, an analytical function can be used in the corrections of eq. 20b. At a frequency of 1KHz, the two functions $|V_{gain}|_R$, $(|V_{film}|_T)_R$ cancel. Then the variation of the resistance of the film due to the heating is shown below.

$$\Delta R = \frac{|V^{\text{heat}}|_R (R+Z_{\text{DC}})^2}{I_{\text{DC}}^2 Z_{\text{DC}}} \quad \text{for } \omega = 2\pi(1\text{KHz})$$

$$Z_{\text{DC}} = 2.24 \Omega \quad (23)$$

For lower frequencies, the corrections do not cancel and are included explicitly, but as mentioned before, the correction is small because of the low values of R (up to 30Ω), where the correction is of the form $\frac{(R+22)}{(R+16)} \sim \text{constant}$. The understanding of this equivalent circuit was strengthened by modeling the experiment with a known variable resistor in the exact same circuit (Fig. 19) as the real film (even including the filters). The results have slightly different parameter values, but the exact same form. A further convincing fact of the model was that the signal $|V^{\text{heat}}|$ was produced only from the optical heating (no ground loops, see Fig. 19). The D. C. current (I_{DC}) could be changed by a factor of 5 and the signal would also change by a factor of 5. The sign of the current could be reversed, resulting in a 180° phase shift of the detected heat signal. The intensity of the heating pulses could be reduced by a factor of 10, and the resulting signal would also scale. Finally, the light beam could be completely blocked, without altering any electrical circuit, and the signal would go to zero over the whole transition range.

Thus the changing resistance ΔR about the average value R due to the heating is determined by the analysis presented above. The film's calibration ($R(T)$) is used to calculate the slope of the transition (dR/dT) and to transform the measurements to temperature. The slope is calculated using a nearest neighbor derivative method

and consistent averaging (see Appendix E). The energy delivered per pulse (ΔQ) is estimated (to be explained later) and the heat capacity of the film, using the equation of Fig. 17 is shown below.

$$C_{\text{tot}}(T) = \left(\frac{\dot{Q}_{\text{abs}} \tau_{\text{heat}}}{\Delta R} \right) \left(\frac{dR}{dT} \right) \left(\frac{1}{R} \right) \left(\frac{1}{T} \right) \quad (24)$$

At first, it was thought that the slope ($\frac{dR}{dT}$) could be measured just by measuring the heat capacity at very low frequencies (2Hz) with a background of He gas, and then $C_{\text{tot}}(T)$ would be a slowly varying function, and the slope could be determined from ΔR and eq.24. Since the temperature range of the experiment (ΔT_{exp}) is very small relative to the operating temperature ($T_{\text{exp}} \sim 1.8\text{K}$), the ratio of $\Delta T_{\text{exp}}/T_{\text{exp}} \sim 10^{-2}$. Over this small range, functions of T , T^3 , $\exp(T)$ are constant to within a 5% error in the measured function. Thus the background heat capacity of a low frequency measurement would indeed be constant, and the 2Hz measurement should be proportional to the derivative. But this was not the case, indicating that even at 2Hz, a sizeable fraction of the heat capacity was due to the film. A final verification of the overall experimental analysis was that the theoretical forms for the final results of conductivity and heat capacity could be fit to the data, and a back calculation to the raw data could be performed. The major features of the raw data agree quite well with the back calculation (sketched in the plot of fig. 19). Thus, although the analysis

of the data was a complicated process, the general method was simple, and it involved no fitting of arbitrary parameters to the data. There was only slight smoothing done on the data in calculating the derivative (see Appendix E), and the final results were completely consistent with the raw data (the back calculation).

Error Analysis

Although there are many smaller errors in the experimental measurements, the major errors are due to the noise and drift of the signal $|v^{\text{heat}}|$ produced by the A.C. heating, and the noise and drift of the measurement of the resistance R. The latter is especially serious for small values of R. These errors are predominantly larger than the intrinsic errors of the electronic equipment used in the measurements. The digital conversion of the analog signals does not reduce the accuracy of the measurement.

The data is sampled by unipolar 12 bit analog-to-digital converters averaged at high speed by the computer software. The digital sampling has an overall accuracy of 2 parts in 10^4 . The analog signals are limited by the drifts of the D.C. output amplifiers. The output of the PAR HR-8 lock-in, which is used to measure T and $|v^{\text{heat}}|$, is accurate to 1 part in 10^3 or about 5 mv, whichever is greater. The output of the PAR-126 lock-in which is used to measure R is accurate to 1 part in 10^4 or 1 mv, whichever is greater. The modulated light source is quite stable over short times, but it has an overall drift of about 10%. All reference currents are accurate

to better than 1 part in 10^3 . The correction functions $|V^{\text{gain}}|$ and $|V^{\text{film}}|$ are measured and fit to better than within 2% of the analytic functional forms mentioned earlier.

The temperature is physically stable to $10 \mu\text{K}$ and by the use of the off-null bridge measurement (see Appendix A) of the Germanium resistance thermometer, a 10 v signal of the HR-8 corresponds to between 20 and 100 mK. The noise of the HR-8 is then transformed through the film's calibration to an equivalent temperature error of between 20 and $100 \mu\text{K}$. It should be emphasized that this experiment does not require an absolute temperature measurement but only short-term temperature resolution between neighboring points. The accuracy of sampled temperature data is thus limited only by the short-term physical fluctuations which are of the order of $10 \mu\text{K}$. The resistance of the film is measured as a scaled voltage, so that an error in the sampled resistance values corresponds to an error in the scaled voltage as a percentage of the maximum resistance of the film, R_N . Since the resistance is measured with the PAR-126, this makes the error in the resistance to be less than .1% of R_N . As for the temperature measurement, the short term resolution of R is governed by the noise in the resistance measurement coming from the lock-in and from thermal fluctuations. The thermal fluctuation noise is the larger of the two and is on the order of $dR/dT \times 10 \mu\text{K}$, which varies from $30 \text{ m}\Omega$ to less than $1 \text{ m}\Omega$ depending on the value of dR/dT for the particular point in the transition. The time constants used on the lock-ins represent an averaging of between 6 and 12 neighboring points for the R, T measurements and $|V^{\text{heat}}|$

measurements respectively. There can be considerably less averaging in regions where the measured quantities are rapidly varying.

Thus, the major errors in the experiment are in the $|V^{\text{Heat}}|$ signal, which reflects the fluctuations in the light intensity, and in the determination of the film's resistance and its derivative, with respect to temperature, in regions where R is small. These contribute to the determination of the change in resistance ΔR from the optical heating. The errors in the biasing current I_{DC} and in the value for the D.C. transformer impedance Z_{DC} are small contributions. In Figure 20 is shown the raw data used in the calculation of the heat capacity for run #38B. Figure 20d is the raw data for the signal $|V^{\text{Heat}}|$ as a function of the film's resistance for an optical heating at a frequency of 1 KHz. The arrow indicates the value of resistance at which the signal to noise ratio is unity, and hence the data has no meaning after that point. The fluctuations in the signal are a combination of real noise and fluctuations in the derivative of the resistance with respect to temperature (dR/dT , see Appendix E). Figure 20b shows the function which corrects the $|V^{\text{Heat}}|$ signal due to the changing D.C. bias current resulting from the changing value of R . These two functions used in calculating ΔR from eq. 24 give a total error in the determination of ΔR of between 2 and 8%, depending on where in the transition the value is determined. Figures 20b and 20d also reflect the effect on the raw data (Fig. 20d) of the decrease in the biasing current as R increases. Figure 20c shows the resistive transition of film #38 in a T vs. R plot. Figure 20a shows dR/dT of Figure 20c plotted vs. R

on the same scale. The method of determining dR/dT was outlined earlier. The region of meaningful $|V^{\text{Heat}}|$ data is indicated and it is smaller than the region of valid dR/dT data. This region is reflected in Figure 20c to indicate the total range (points P, P') in temperature of valid data. The percentage error in the value of dR/dT varies from 5% to 10% and is largest near the endpoints of the transition.

The calculation of the heat capacity uses the equation shown in Figure 20. The major errors are in the values of $|V^{\text{Heat}}|$ and dR/dT , which are given above. These values result in between 7 and 18% overall error in the value of the heat capacity. The error in temperature is considerably smaller, since it is just a reflection of the error in R transformed to temperature and amounts to between 20 and 100 μK , as stated earlier. Figure 21 shows the heat capacity calculated from the raw data of Figure 20 displayed over the temperature range of valid data. The errors in this calculation are reflected in the scatter at the higher temperatures, where the $|V^{\text{Heat}}|$ signal is small. The heat capacity in the lower temperature region increases above a constant value with decreasing temperature. This effect will be discussed in the next section. The rise in heat capacity occurs in the region where R is small, and the errors of dR/dT are large, but the effect is significant despite the overall error of between 7 and 18%. Since the temperature resolution is considerably more accurate than the resolution in heat capacity, the monotonic behavior of the heat capacity in this region indicates that over short regions, the error in this heat capacity measurement

Figure 20.

Raw data used in determination of heat capacity. a) is the digital derivative of the resistive transition of the film c), plotted vs. the film's resistance R. b) is the correction to the heating signal d) due to the transformer in parallel with the film. The arrow indicates the limit of valid data in d) and is reflected in figure c) to show a range in temperature (P, P') of valid data. The thermal excursion due to the A.C. heating is shown below.

$$\Delta T |R = \frac{|V^{\text{heat}}|}{(dR/dT) \left(\frac{Z_{DC}}{R+Z_{DC}} \right)^2} |R$$

For the data shown this is on the order of $1 \mu K$. The heat capacity is then given below.

$$C = \frac{\dot{Q}_{\text{abs}} \frac{dR}{dT} T^{\text{heat}}}{|V^{\text{heat}}|} \left(\frac{Z_{DC}}{R+Z_{DC}} \right)^2$$

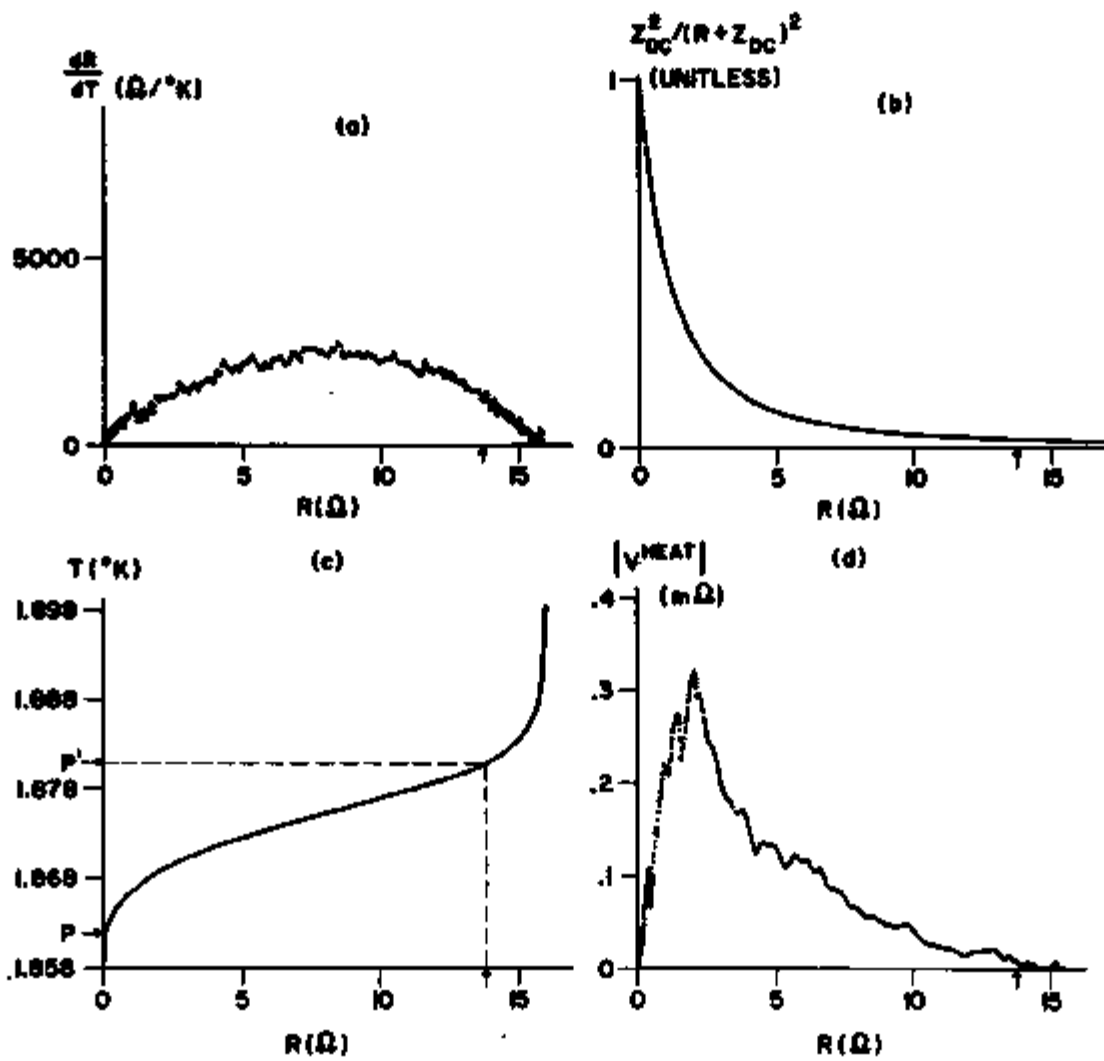


Figure 20.

is smaller than 7 to 18%. The inset of Figure 21 shows a semi-log plot of the logarithm of the excess heat capacity vs. temperature over a smaller range in temperature. This suggests that the total heat capacity may in fact, be diverging logarithmically. The excess conductivity of this film also had the same slope and linear behavior on a logarithmic plot in this region.

The heat capacity is plotted in relative units because only an approximate determination of the optical heating power \dot{Q}_{ABS} was made. Two methods were used in this determination. The first was to use an optical detector in place of the film to measure the amount of light shining down on the region the film occupies in the experiment at low temperatures (see Appendix B and Appendix C). Taking this value and the estimated light cone distribution and optical absorption of the film, the value of \dot{Q}_{ABS} was estimated at 2×10^{-11} watts. A more accurate method was to stabilize the film in a sensitive region of the superconducting transition (dR/dT large) with the laser off and measure the temperature rise due to turning the laser on for a short period of time. This same rise in temperature could also be produced by increasing the Joule heating of the film by changing I_{DC} . If this is done fast enough (~ 1 sec.), it gives an adiabatic determination of the power absorbed \dot{Q}_{ABS} . The value of \dot{Q}_{ABS} estimated this way was between 5×10^{-13} and 2×10^{-12} watts. As this method of determining \dot{Q}_{ABS} should be more accurate than that method explained earlier, one takes the value of \dot{Q}_{ABS} to be on the order of 10^{-12} watts. Using the equation of Figure 20, one then finds the value for the heat capacity of Figure 21 in the flat region to be

RUN #38B

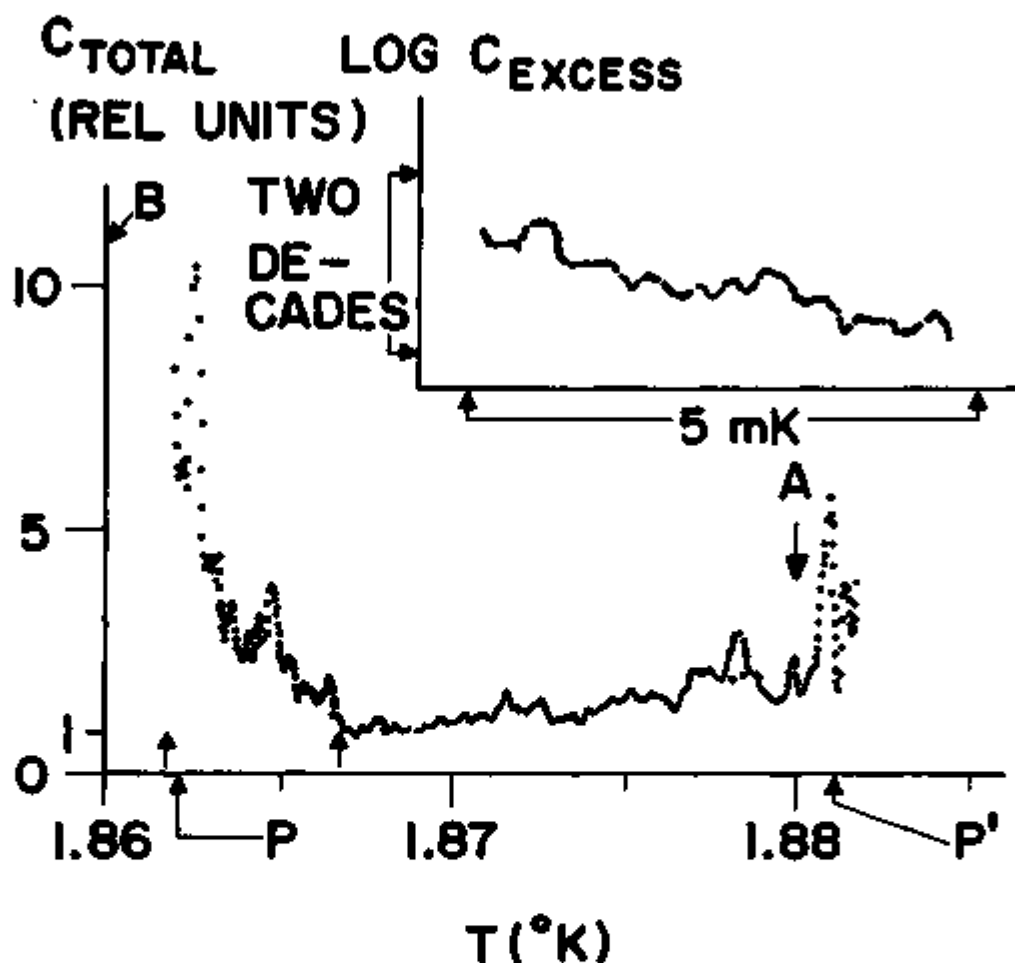


Figure 21.

Plotted is the total heat capacity of Sample #38B for a 1 KHz optical heating frequency. The points P, P' indicate the region of valid data. The data between the arrows is plotted in the insert as an excess heat capacity ($C_{\text{excess}} = C_{\text{total}} - C_{\text{background}}$ where $C_{\text{background}}$ is the linear region at higher temperatures). The insert is a logarithmic plot of the excess heat capacity and shows a linear behavior over the region indicated by the arrows. Point A is the MFT T_c , and point B is the temperature for $R = 0$.

on the order of that calculated for the film in Appendix F. If the heat capacity in the flat region of Figure 21 includes a contribution from part of the substrate, then what one has called an absolute determination of the film's heat capacity is only an upper limit. In Appendix F the maximum percentage contribution to the heat capacity by the mica is estimated at about 50% of the total heat capacity when the latter is measured at 1 KHz.

In conclusion, the errors of the experiment largely are the result of the "noise" in the determination of dR/dT and in the raw data ($|V^{Heat}|$). This error is between 7 and 18% overall, but it is considerably better over short ranges. The absolute determination of the total heat capacity measured is on the order of the values expected for the film, and the percentage of the measured heat capacity contributed by the film is between 50 and 100 %.

Chapter 5. Data Analysis and Discussion

General Features

The properties of the films studied are outlined in detail in Appendix H. Measurements were carried out using experimental methods discussed earlier. All data discussed in this section was taken in zero magnetic field unless explicitly noted, and at an optical heating frequency of 1KHz ($\tau_{\text{heat}} = 10^{-3}$ sec.). The films were made by slow evaporation of aluminum in varying pressures of O_2 gas onto cleaved mica substrates. Particular values for the preparation parameters of the films discussed are listed in Table 3. The films are generally quite granular (average grain size $\sim 400 \text{ \AA}$), with a significant range in grain size. They also have short mean free paths (λ_{eff}) as determined from the normal state sheet resistance R_{\square}^N listed in Table 3. An independent determination of λ_{eff} was done in an applied magnetic field (see Appendix H), which was in agreement with that calculated from R_{\square}^N . The transition temperatures determined from the resistive transitions are on the order of 1.86K. The constants listed in Table 3 show a reasonable consistency in the physical nature of the films discussed, with the exception of sample #30 (run #30I). This film was evaporated with a larger O_2 background. Its resistive transition was drastically affected by the amount of D.C. biasing current used in the experiment. Increasing this current resulted in "kinks" appearing in the transition. By increasing the A.C. biasing current used in the

Table 3. Physical Constants For Films Shown

Sample (Run #)	Preparation (gas during exp.)	d (Å)	ℓ_{eff}^{**} (Å)	R_{sq}^N (Ω)	A.L. τ_0	fit τ_0	T_c^{MFT} (pt.A) (K)	T_0 (pt.B) (K)
301	2×10^{-5} Torr O_2	1090	13	2.77	4.21×10^{-5}	7.04×10^{-4}	1.829	1.778
*368	1×10^{-7} Torr No O_2	1040	14	2.63	4.00×10^{-5}	2.32×10^{-3}	1.880	1.860
388	2×10^{-7} Torr No O_2	1170	53	.644	9.78×10^{-6}	9.50×10^{-5}	1.880	1.860
39	2×10^{-7} Torr No O_2	1190	23	1.46	2.21×10^{-5}	7.50×10^{-5}	1.843	1.814
	H = 21.8 Oe	The field lowered the temperature of the transition and broadened the overall transition. This measurement gave a value of $\xi(0) \approx 440$ Å. See Appendix H.				7.38×10^{-5}	1.827	1.758

Note: The width to length ratio was between 3 and 4×10^{-2} for these films. The evaporation rate was between 25 and 35 Å/sec. The ratio of the resistance at 300 K to the normal resistance was between .8 and 1.2. Point A in the heat capacity figures is the MFT T_c . Point B is the temperature for $R = 0$.

* Double transition. ** Using the relation $\ell_{eff} = \frac{4 \times 10^{-12} \Omega \text{ cm}^2}{R_{sq}^N d}$. See Appendix H.

experiment to a level equal to the D.C. current, these "kinks" could be dramatically reduced. When the "kinks" were removed, the overall transition was slightly different from the transition measured with a current less than that which would affect the resistive features of the transition (on the order of 10^{-6} A). This effect is discussed in more detail in Appendix H.

The heat capacity measured for film #38 is shown in Fig. 21. The analysis that led to this result is discussed in an earlier section. Over the temperature interval of the data plotted in Figure 21, functions exhibiting T , T^3 , and $\exp(T)$ are constant to within 5%. Thus over the range from about 1.867K to 1.88K, there is a contribution to the total heat capacity that is constant. The electronic contribution of the film's heat capacity is 80% of the total heat capacity of the film (see Appendix H, F) and the estimated amount of background heat capacity (from the mica, see Appendix F) is between 0 and 50% of the total heat capacity measured. Thus, in the constant region of the total heat capacity in Figure 21, the electronic heat capacity of the film represents between 80% (no mica contribution) and 40% (50% mica contribution) of the total measurement. This means that the normal state heat capacity, defined as $C_n = C_{\text{electronic}}$ for $T > T_c$, is between .4 and .8 relative units on the plot of Figure 21. One would expect that the B.C.S. discontinuous jump in the heat capacity at T_c for a film to be given by the usual equation, which is shown below.

$$\Delta C = C_s - C_n \text{ and } \Delta C = 1.43 C_n \quad (25)$$

Thus, one would expect the heat capacity in the superconducting state C_s near T_c to be equal to $2.43 C_n$. This means that the rise of the total heat capacity plotted in Figure 21 is between 5.5 and 11 times the expected B.C.S. jump, depending on what percentage of background contributions are present in the total measurement. This rise is occurring 18 mK below the MFT transition temperature (point A), as determined from an A.L. fit to the resistive transition. This rise is also very near (~ 2 mK) the temperature where the film's resistance becomes zero. It is possibly only a coincidence that the temperature range of the resolution of the experiment (P,P') is on the order of the temperature difference between point A and point B. The excess heat capacity is defined as the difference between the normal and the superconducting heat capacities ($C_{\text{excess}} = C_s - C_n$), and should be zero far above T_c , and equal to ΔC far below T_c on the plot of Figure 21. The logarithmic plot of the excess heat capacity in the insert of Figure 21 is for the range in temperature indicated by the arrows. This plot indicates a linear relationship between the logarithm of the excess heat capacity and temperature. Since the oscillations in temperature (ΔT) used in this heat capacity measurement are considerably less than the thermal fluctuations of the sample ($\Delta T \sim 1 \mu\text{K}$, $T \rightarrow T \pm 10 \mu\text{K}$), the measurement is essentially a high speed average (averaging time = 1 cycle = 10^{-3} sec) over a region in temperature $10 \mu\text{K}$ wide. In principle, the method of correlation in R could resolve this width in temperature, but because long relative time constants are chosen for the electronics used in the

measurement (3 sec), and since the temperature of the film is continually increasing in time, the total heat capacity measured will always be an integrated measurement over a broader range in temperature. This is an inherent limit on the ability of the experiment to determine heat capacities changing very rapidly with temperature. As stated earlier, this limit is an average over, at most, 6 neighboring points in temperature. This means that the steeper part of the rise of the heat capacity in Figure 21 occurs over a region that is 1 mK wide at most. The total rise occurs over a range of about 6 mK. This width will be discussed later.

Electrical Conductivity

As stated in the theoretical section, the conductivity of the films would be studied to determine if their transitions were broadened by inhomogeneities. This determination comes about by fitting the resistive transition to the theoretical form of A.L. theory, given earlier. The width of the transition for this fit τ_0 is compared to the theoretically derived width $\tau_0^{A.L.}$. Inhomogeneities would tend to broaden the transition and make $\tau_0 > \tau_0^{A.L.}$. There are theoretical models that relate intrinsic broadening for ratios of $\tau_0 / \tau_0^{A.L.} > 1$ to an intrinsic pair breaking process determined by the value of R_D^N . This is discussed in Appendix H. Table 3 lists the fitted transition width for the particular films discussed here. Some values for R_D^N and the ratio $\tau_0 / \tau_0^{A.L.}$ are in agreement with the A.L. theory, but in disagreement

with the theory of Patton, discussed in Appendix H. These results are in better agreement with the work of Thompson, et.al.⁴³, except that only film #30 exhibited the D. C. current features they observed. Although some transition widths agree with A.L. theory, the films are probably not homogenous because of the long tails in the transition (as compared with the sharp transitions in Glover's work of amorphous Bi⁴⁶). Thompson, et.al., suggest that these tails in the transitions of dirty aluminum films are due to the thermally excited phase fluctuations in the coupling between grains of the film, destroying long range order and creating a resistance in the film, but still maintaining a non-zero value for the order parameter. Thus, the transition width determined from conductivity measurements is not a direct measurement of the width of the superconducting phase transition in aluminum films. The distribution of the transition temperatures of the grains in the film produces a premature transition at higher temperatures as a result of a few grains "shorting" out the contribution to the resistance from the majority of the grains. At the same time, phase fluctuations between grains will result in a finite resistance below the superconducting phase transition. Figure 22 shows the resistive transition for film #39. An A.L. fit with the parameters shown is also plotted. The insert of Figure 22 shows the excellent agreement of the A.L. theory with the resistive transition at higher temperatures. The parameters are determined by choosing a value for R_N that is consistent with the measured values of the film. Then the inverse

RUN #39 (H=0.0e)

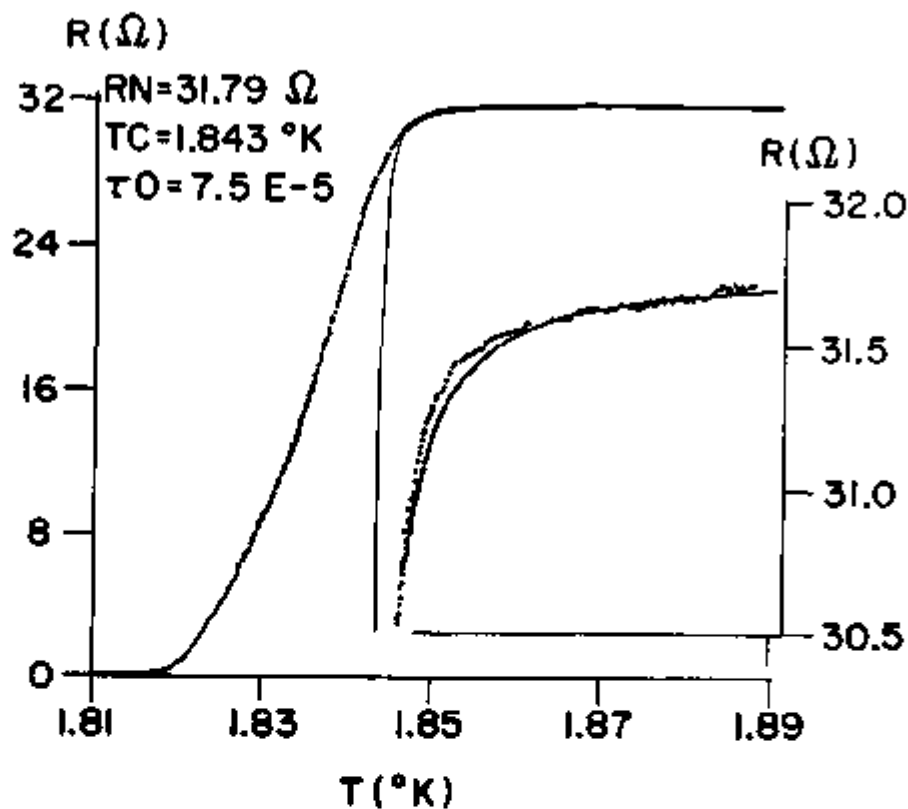


Figure 22.

Resistive transition for film #39. The plot is of 1020 discrete points. The A.L. fitted parameters are shown, along with the fit. R_N is approximated and is very close to the R_N (for $T \gg T_C$) measured. T_C , τ_0 are determined graphically (see Figure 23). The insert shows the good agreement with the fit at the high temperature end plotted on the same temperature scale.

of the excess conductivity (where $\frac{\sigma'}{\sigma_N} = (RN-R)/R$) is plotted in Figure 23, and a linear fit is used to determine the transition temperature T_c and the transition width τ_0 . This type of fitting can give varied results, depending on the region over the data which the theory is forced to fit. The parameters T_c , RN , and τ_0 can be varied over considerable ranges that result in fits over many separate regions of the transition. Obviously the theory cannot fit the whole transition, so that the choice of where the resistance of a film fits to the theory is extremely arbitrary. Roughly, the parameters vary the theoretical function for the film's resistance in the following way. The width parameter τ_0 determines the angle between the steep region of the transition and the flat region. The value for the normal resistance RN determines the value of the resistance and the slope at the high temperature part of the transition. And finally T_c moves the overall features up and down in temperature. These functional variations are not independent, but by the use of the Tektronix display mentioned in Figure 19 and used in all the plots of this section, one can see this rough variation of the theoretical transition by varying the parameters T_c , RN , τ_0 . In this way, the transition can be fit to the A.L. theory in any arbitrary region. It is quite possible that the premature transition brought about by the "shorting" of a few grains in the film is creating the slope at the high temperature end of the transition, which results in the high T_c obtained in the A.L. fit. It is more likely that the real transition is occurring

RUN # 39 (H = 0 Oe)

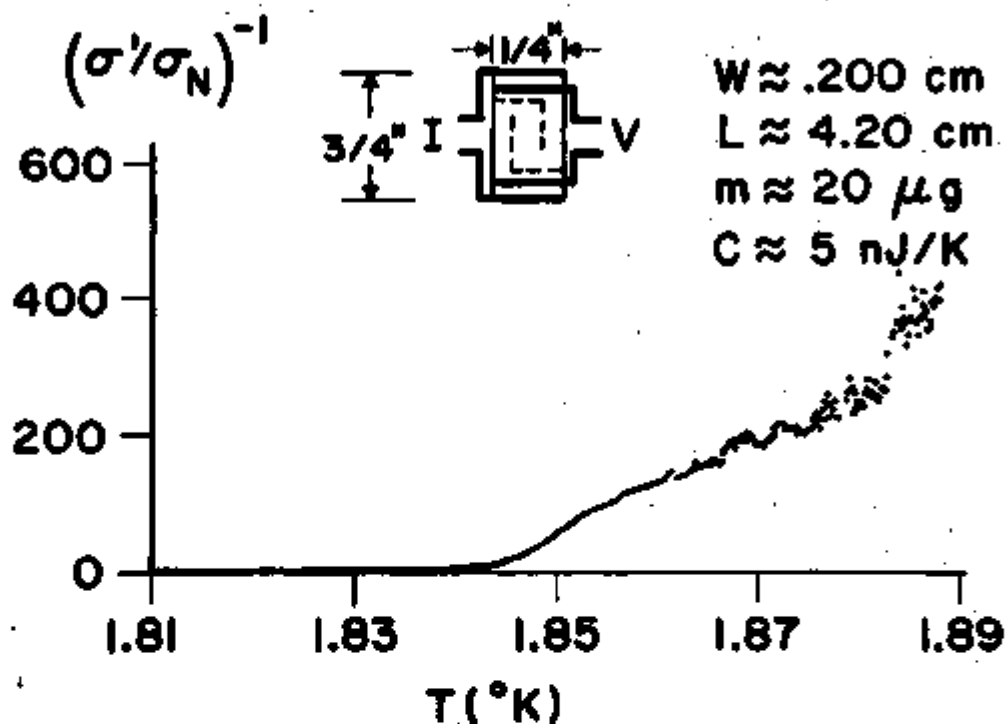


Figure 23.

Inverse of the excess conductivity ratio plotted vs. temperature for Run #39. The value chosen for RN is that used in Figure 22. A linear form is fitted to the data to obtain the T_c and τ_0 used in the fitted plot of Figure 22. The insert shows the film's geometry with typical parameters. The films are edged scribed and also scribed with the pattern scribe shown (to increase the film's resistance).

in a region where the majority of the grains are going superconducting, and would be at a temperature considerably lower than the fitted value for T_c used in Figure 23. Thus, it is believed that the real superconducting phase transition in dirty aluminum films cannot be determined by conductivity measurements and may actually be occurring in the region where $R \approx 0$. This idea is supported by work done in this lab which measured the excess tunneling current in Sn-Pb Josephson junctions for $T > T_c$ of the Sn⁴⁵. This work indicated that the phase transition, as determined by the excess tunneling current, was actually occurring near $R=0$ for the Sn film. Thus, although the conductivity of the films discussed in this section is in agreement with the A.L. theory, it is quite possible that their transitions are broadened due to the inhomogeneities brought about by the different transition temperatures of the various grains in the film. This model could possibly explain why the transition widths of the heat capacity results of Figure 21 are broader than $.69 T_0^{A.L.}$, which is determined from the film's conductivity; and it could explain why the rise in the heat capacity of the film is occurring at a temperature far below the T_c^{MFT} determined from the A.L. fit.

Heat Capacity

The general features of the total heat capacity plotted in Figure 21 were observed in 9 films. One of these films was a fully self-supported film (see Appendix H) that had a measured relative heat capacity on the order of that observed for the

films on mica substrates. This indicates that the total heat capacity measured for the films on mica might be a 100% measurement of the heat capacity of the film itself.

Figure 24 shows the total heat capacity measured for film #30, plotted for three ranges of temperature. The heat capacity exhibits a rise from a constant value at the low temperature end of the transition. The higher resolution in temperature shown in Figure 24c indicates a peaking of the total heat capacity. Using the same estimates as given earlier in Figure 21, this results in a rise of between 4.5 and 8.6 times the expected B.C.S. jump in heat capacity. The temperature width in this rising region is about 5 mK wide, which is considerably larger than the $\tau_0^{A.L.}$ width parameter from A.L. theory. But it is within a factor of 10 of the value for τ_0 that is used to fit to the resistive transition. Since the ratio of $\tau_0 / \tau_0^{A.L.}$ is greater than unity (≈ 17), this might be an intrinsically broadened film, although it is still in disagreement with the theory of Patton, discussed earlier (i.e., the ratio is too large for its value of R_{\square}^N). Another possibility for the observed peaking in Figure 24 may be a result of its granular nature. Since this film exhibits a strong dependence on D.C. current, and since it was prepared in a heavy oxidizing atmosphere, the Josephson tunneling between grains could cause large order parameter phase fluctuations between the grains. This peaking in the heat capacity may be related to a transition from a "paracoherent" coupling of the grains to a coherent coupling brought about by the electron tunneling, and thus the phase transition

RUN #30 I

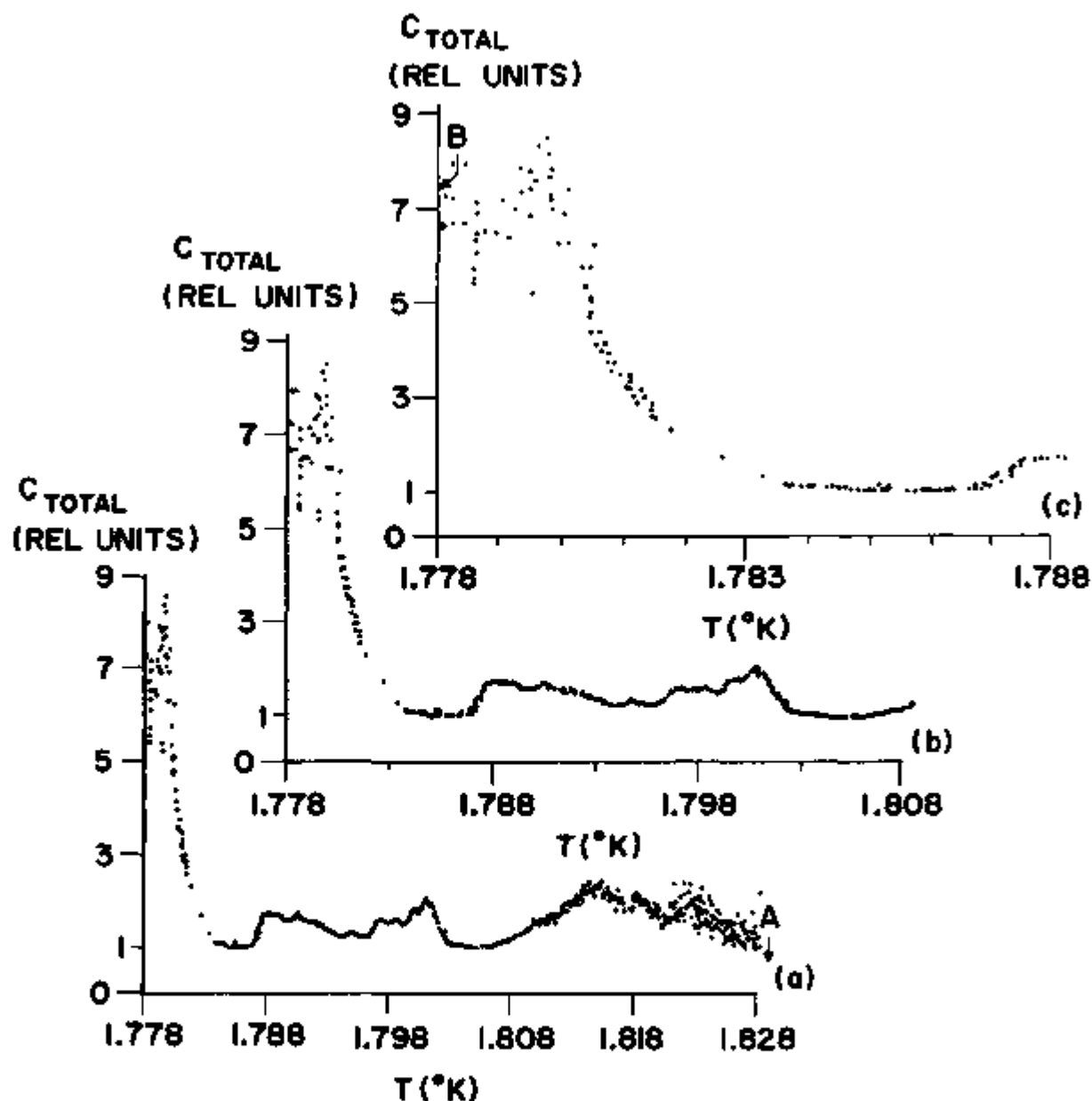


Figure 24.

Total heat capacity plotted for Run #30I. The temperature scales have been enlarged to show the rising heat capacity near point B. a) is 50 mK wide, b) is 30 mK wide, and c) is 10 mK wide. There is an apparent peaking and then a leveling off in the data near point B.

in the heat capacity may be a consequence of the ordering of the grains. This phase transition is discussed in Ref. 47 with regard to an interpretation of conductivity measurements made on bulk powdered Nb and Ta samples in which a precipitous drop in the resistive transition is observed at a low temperature tail.

Figure 25 shows the resistive transition of film #36. This film has a multiple transition, with the first transition at about 1.88K. Figure 26 shows the total heat capacity for film #36 with the resistive transition over the same temperature range superimposed on the plot. There is a definite peaking of the heat capacity over a region of 15 mK which rises to a value of between 12 and 25 times the B.C.S. jump, at a temperature of about 12 mK below the T_c^{MFT} (point A). But there is also a rise in the heat capacity of a similar nature at the low temperature region as seen in the previously mentioned films. This rise occurs over about a 5mK region and increases to a value of between 4 and 7.6 of the B.C.S. jump. Due to the multiple transition in the film, the thermometer in effect has a range that is extended below the transition of the first film, and thus allows the measurement of heat capacity below the first transition. The results of Figure 26 indicate a possible peaking in the heat capacity of the film at the first transition, and a consistent rise near $R=0$.

Magnetic Field Effects

Because of the predicted effects of the alteration of the heat capacity by the application of a small magnetic field,

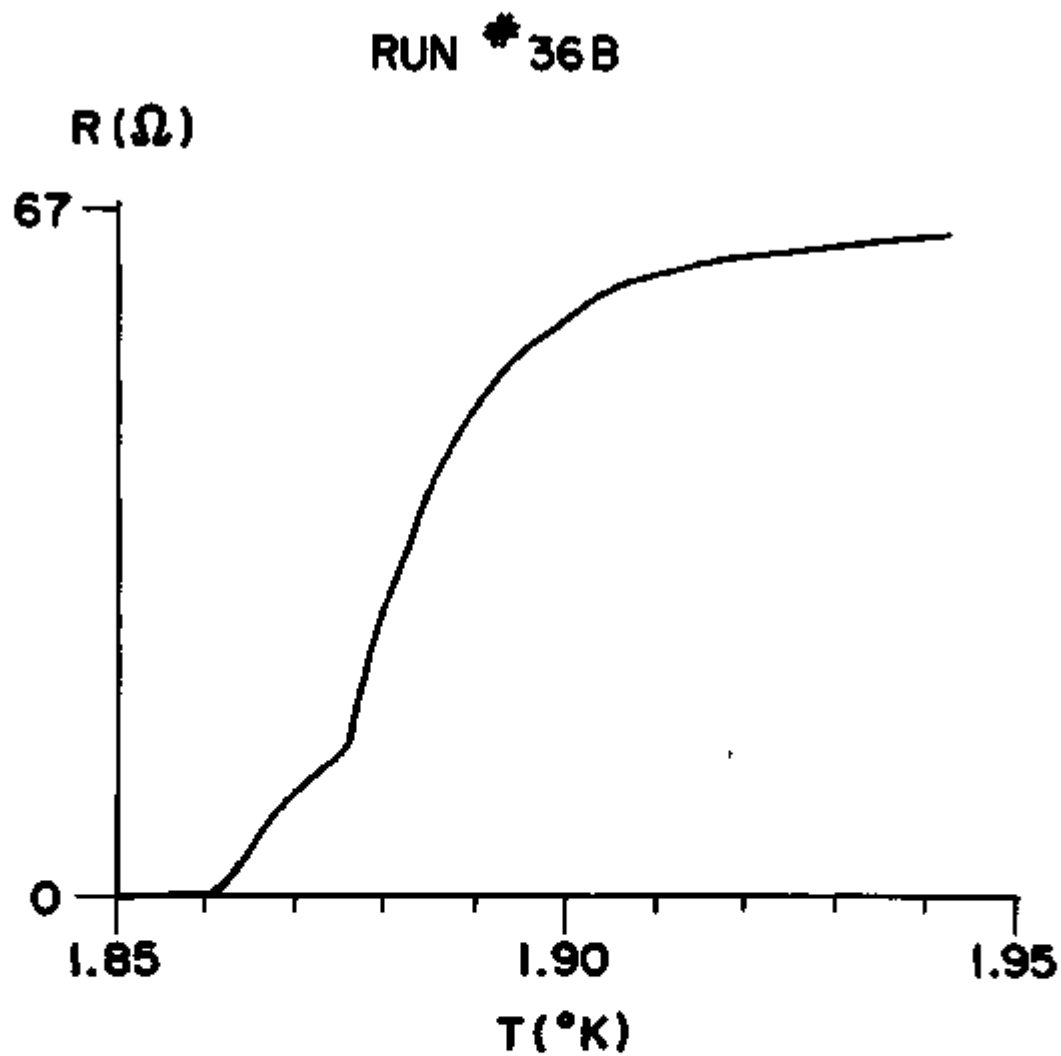


Figure 25.

Resistive transition for Run #36B showing the multiple transition.

RUN 36 B

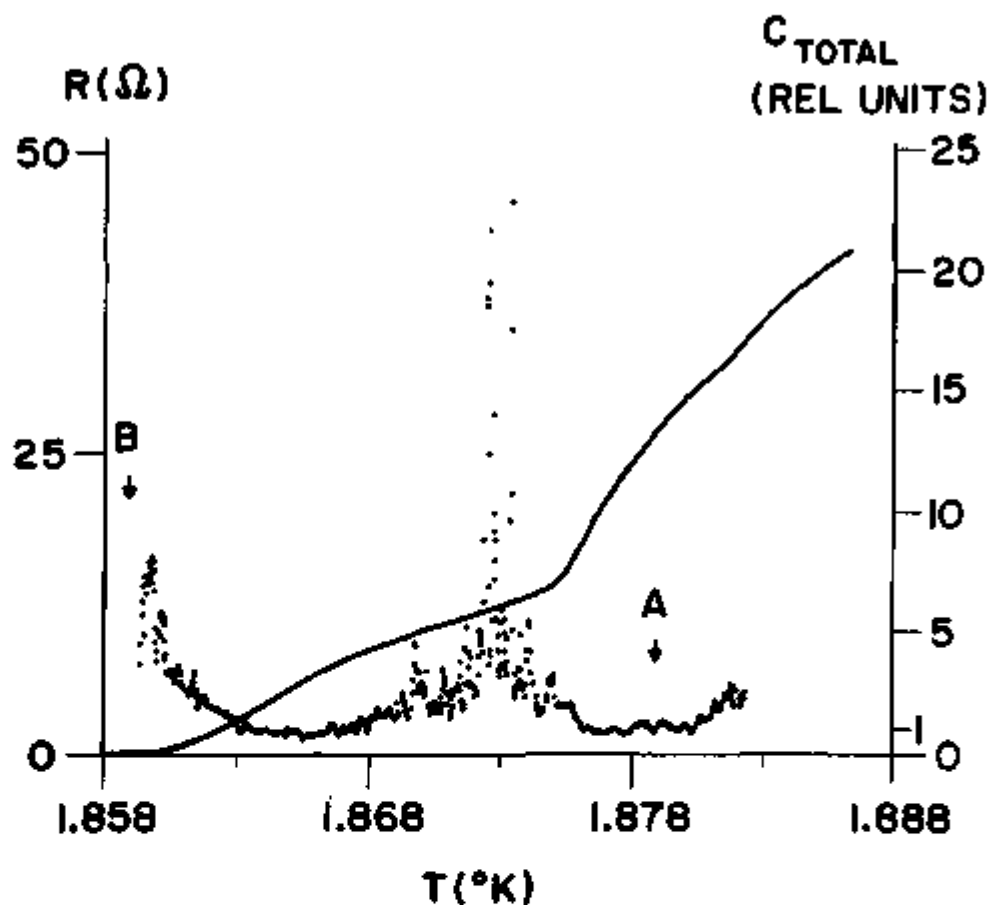


Figure 26.

Resistive transition and heat capacity for Run #36B. The resistance plot is of the tail of the transition shown in Figure 25. The heat capacity exhibits a peaking at a temperature below the 1st resistive transition and a slow rise at the low temperature end.

discussed in an earlier section, a run was made with a rather crude solenoid attached to the cryostat. This allowed for the application of moderate magnetic fields (although they were about 10% inhomogeneous), which is discussed in more detail in Appendix H. The heat capacity shown in Figure 27 is for run #39 and it is without an applied field. The excess heat capacity is plotted vs. temperature, and it is missing a section of data, due to the inaccurate choice of the background subtraction. This is reflected in the low values in the same temperature region on the logarithmic plot of the excess heat capacity of Figure 27b. Note the rather large peaking in the heat capacity at the low temperature end (16-32 BCS) near point B. The rise occurs over a range in temperature of 10 mK with the peak being on the order of 3 mK wide. The peaking occurs at a point about 25 mK below the T_C^{MFT} determined from the fit of Figure 22. The logarithmic plot varies linearly with temperature in the rising heat capacity region, in a manner similar to that of Figure 21. This might indicate a divergence, where the predicted peaking from the screening approximation discussed in an earlier section is just the first term of a series in powers of ϵ^{-1} (see Ref. 41). The inverse of the excess heat capacity is plotted in Figure 28. This type of a plot suffers from the inaccurate determination of the background heat capacity $C_{background}$ that is similar to the problem of the choice of RN used in the plot of Figure 23. The application of a 21.8 Oe magnetic field caused a change in the resistive transition, mentioned in Table 3 and shown in Figure H-5 of Appendix H. The major feature was to shift the transition to a lower temperature (point A is lowered in temperature)

RUN #39

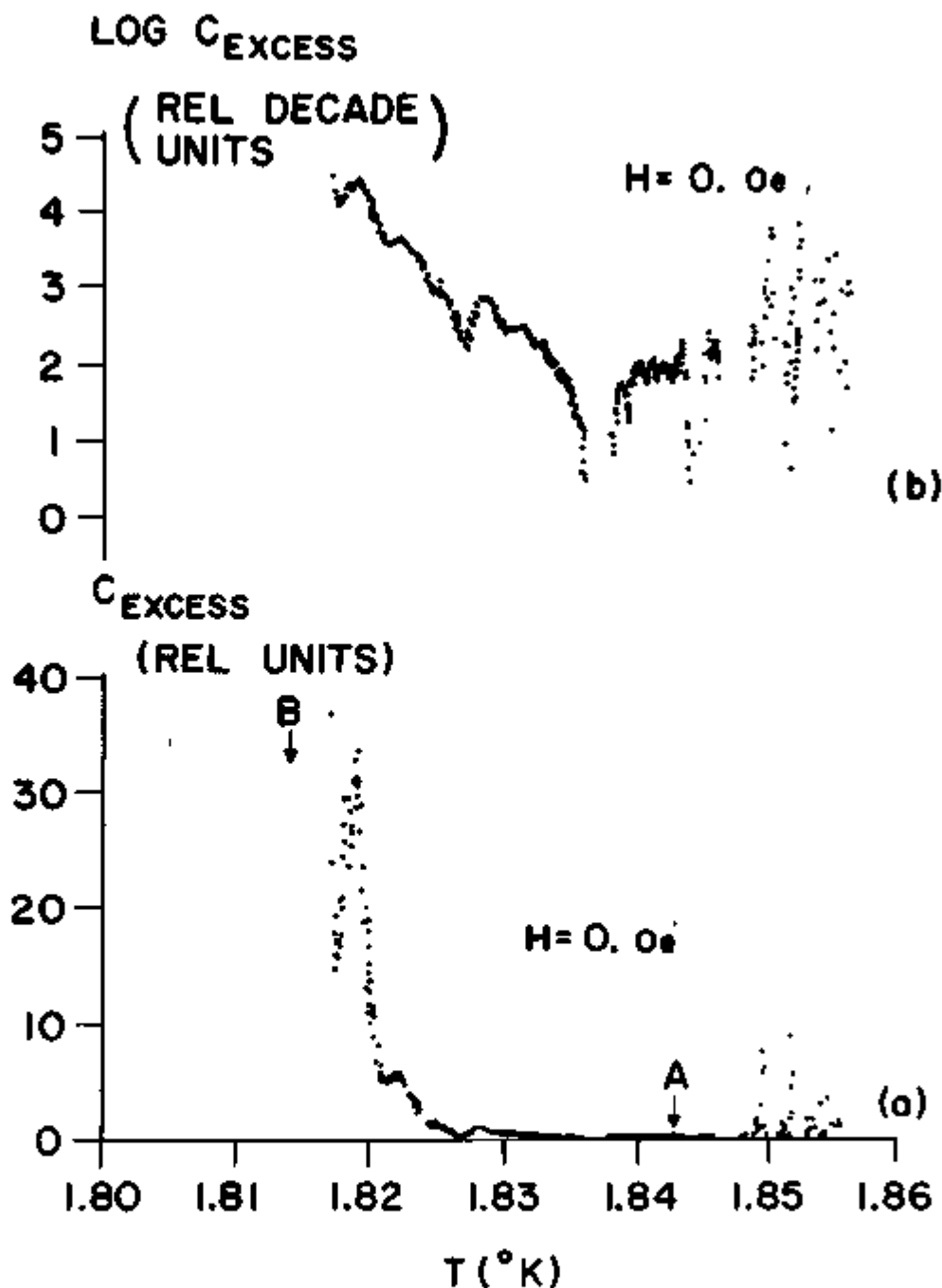


Figure 27.

a) Excess heat capacity plotted for Run #39. The $C_{\text{background}}$ used was just a constant value. Note that it was a little too large at about 1.835 K, and results in a negative (not shown) value for the excess heat capacity. This is reflected in the dip of the logarithmic plot of b). The rising region of a) has a linear form on the logarithmic plot of b) and exhibits a definite peaking.

RUN # 39

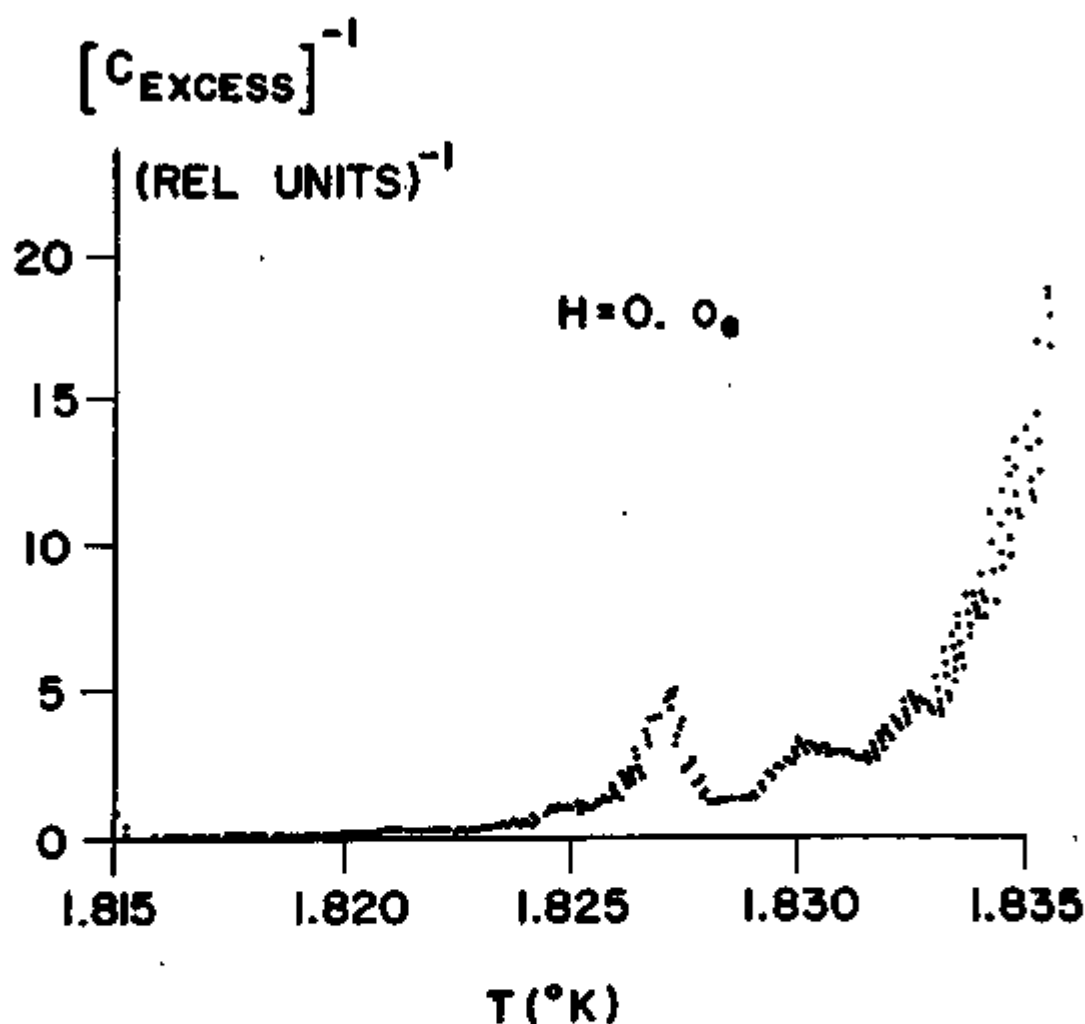


Figure 28.

Inverse of Excess Heat Capacity for data of Figure 27. The plot is over a temperature range where the background subtraction is not important. The determination of the subtraction constant is the same problem as the determination of RN used in Figure 23. Note the similarity in the low valued linear regions of the plot of Figure 23 and the plot shown here.

and to provide a tail in the transition that extended the thermometry (the difference between T (pt.B) and T (pt.A) is increased). The total heat capacity measured in a magnetic field is shown in Figure 29b with the zero magnetic field result also plotted over the same width in temperature. The dramatic result shown in Figure 29 is that the peaking of the heat capacity in zero magnetic field is reduced, broadened and shifted to a lower point in temperature when a magnetic field is applied. The shift is to a point 43 mK below the zero magnetic field result, and over a widened temperature range, which is on the order of 30 mK. The extended thermometry due to the tail in the resistive transition brought about by the applied field is probably related to magnetically induced phase slippage in the coherence of the Josephson coupling between grains. This extension allows for the determination of a plateau in the heat capacity of the film in an applied field, at a temperature below the rise seen in the heat capacity of films discussed earlier. One should notice the reproducible bumps in both Figures 29a and 29b in the region of rising heat capacity. The magnetic field results are in qualitative agreement with the fluctuation predictions presented in the theoretical section.

Discussion

The results presented earlier indicate a rather large rise in the heat capacity of the four films discussed at a temperature below the T_c^{MFT} (determined from conductivity measurements). The

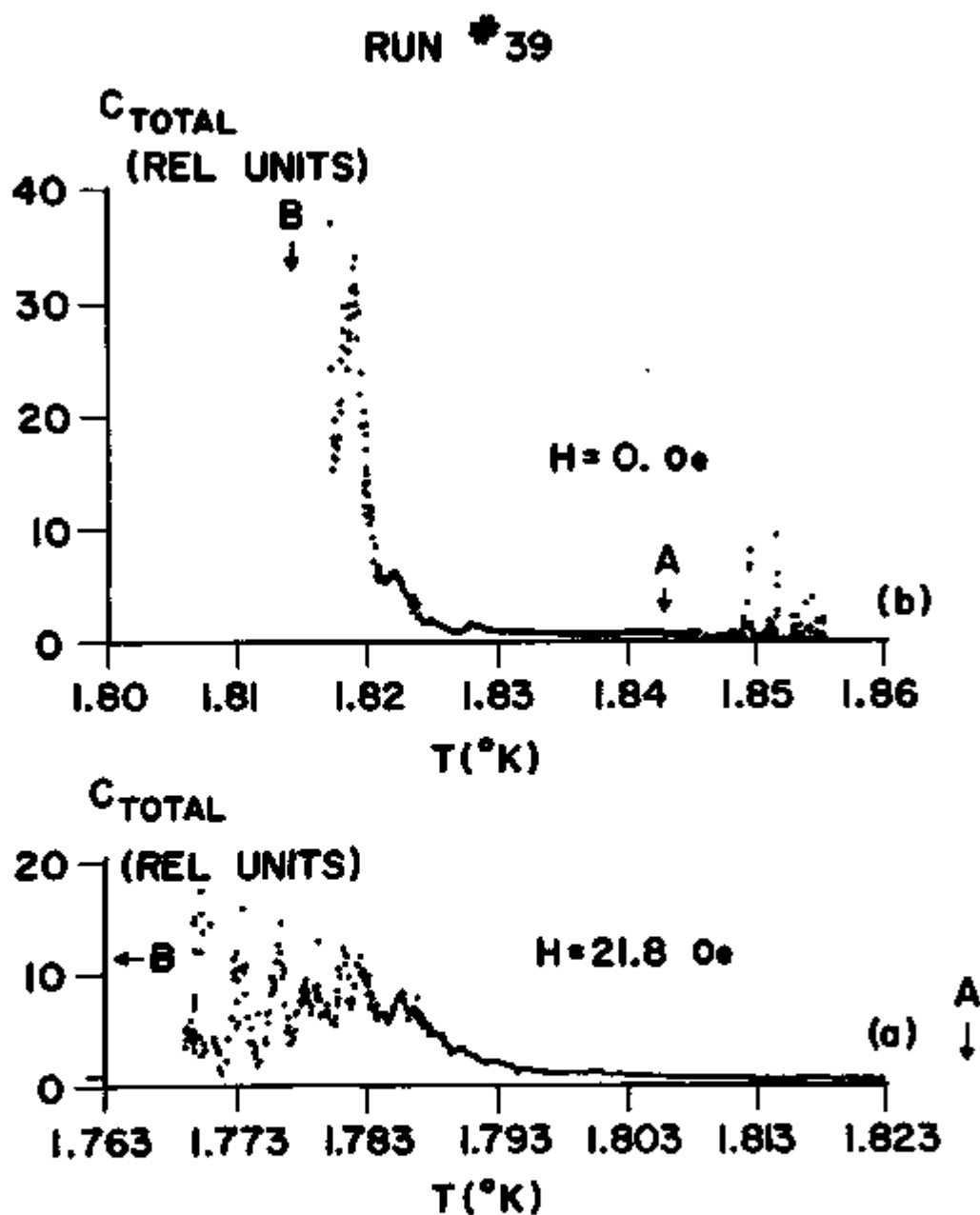


Figure 29.

Total heat capacity of run #39 plotted for two values of magnetic field on the same relative temperature range. a) is for a field of 21.8 Oe b) is for no magnetic field. The magnetic field shifts the transition to a lower temperature and broadens the region where the heat capacity is peaking. At the same time it reduces the size of this peaking of the heat capacity observed in zero magnetic field.

possibility of an error in the analysis of the data should be discussed because of the rather important nature of the results.

The possibility of pair breaking occurring in the film from the laser optical heating is discussed in Appendix F and is believed not to be involved in the present experiment, because the relative number of paired electrons is small at the temperatures of the films studied. Also the pair recombination time is so fast, relative to the heating frequencies, that any disturbed pairs will be recombined just after the end of each heating cycle. The most apparent result was that the resistive transition was unaffected with the laser on or off. This indicates that pair breaking mechanisms due to the optical heating can be ruled out.

A second possibility is that the rise in the heat capacity is associated with a latent heat brought about a local magnetic field. The residual fields ($< 10^{-4}$ gauss) and the induced fields from the measuring currents ($< 10^{-5}$ gauss) are far below the fields needed for such effects.

To be consistent with the bulk superconducting phase transition, the entropy associated with a rising heat capacity has to be less than the observed agreements mentioned earlier between the total heat capacity of the superconducting and the normal states. Cochran's result for Sn ($S_{\text{singularity}} < 10^{-3}$ J/mole K) indicates roughly an entropy for these films of about 10^{-10} J/K associated with any heat capacity singularity. The entropy for the observed peak in the heat capacity is just its width ΔT_p , times the heat capacity

peak C_p , divided by the temperature at which the peak occurs T_p . The resultant entropy associated with the transition is about 10^{-10} J/K (roughly $C_p \sim 10C_S \sim 10^{-7}$ J/K, $\Delta T_p \sim 10^{-3}$ K, $T_p \sim 2$ K). As discussed earlier, King et.al. found agreement to about 5% for the entropy difference between the normal and superconducting states. This means that the entropy associated with a phase transition ΔS_p has to be less than 5% of the total entropy S_T . Since S_T is just equal to the normal state heat capacity at T_c , the requirement of $\Delta S_p < 5\% S_T$ is just the requirement of

$$\frac{C_p \Delta T_p}{T_p} < 5\% C_n .$$

This reduces to

$$\frac{C_p}{C_S} \frac{\Delta T_p}{T_p} C_S < \frac{5 \times 10^{-2}}{2.43} C_S .$$

For the largest peak observed ($C_p/C_S \sim 20$, $\frac{\Delta T_p}{T_p} \sim 10^{-3}$) this condition is satisfied.

It should be noted that the prediction of no phase transition in a 2-D system, mentioned in the theory section, relies on the fact that the order parameter correlation function of the 2-D superconductor does not exhibit off diagonal long range order (ODLRO). It actually states that in 3-D, there is ODLRO, and hence one can have a divergence in the heat capacity. But in 2-D, where one does not have ODLRO, one may or may not have a divergence.

The fact that the data is analyzed by an equivalent circuit may also be a reason for the observed heat capacity. But the

equivalent circuit used is understood very well, and nine films, all with very different sets of raw data and different resistive transitions, had similar overall features.

The disagreement between the peak width ΔT_p and the $\tau_0^{A.L.}$ from the conductivity measurements, and the disagreement between T_p and T_c^{MFT} is not surprising in view of the discussion of conductivity measurements. It might be possible to use a Gaussian distribution in T_c 's similar to that of Cochran to represent the grain inhomogeneities contributing to the broadening of a narrow intrinsic peak. In this case, the coefficient of the diverging term (α) would be varied to get the correct height of the peak, and the range of integration would be over the width of the peak. This model might also explain the disagreement in the conductivity and heat capacity transition widths.

Finally, it should be mentioned that in this laboratory,⁴⁴ there has been other observed behavior of a possible critical region in very similar aluminum films. In the measurements of the inverse peak current of Pb-Al Josephson junctions below the T_c^{MFT} (13 mK below), there is a region 10 mK wide where the GL M.F.T. breaks down.

Conclusion

Because of the theoretical interest in phase transitions, the heat capacity of a two dimensional superconductor has been measured in the transition region. Previous experimental work (ZM) was limited by the arbitrary fitting schemes used in the data

analysis. The previous work was also limited by the ultimate sensitivity of the experiment. The work reported here used unconventional methods to measure the heat capacity of a 1000 Å⁰ granular aluminum film with an unprecedented sensitivity. The film was heated optically and the film's resistive transition was used as its own thermometer. The electrical conductivity and heat capacity results for the four films presented were in qualitative agreement with similar results observed in five other films.

The heat capacity measured from the data on the four films presented increased with decreasing temperature where the films' resistances were zero. The rise was over a range of 1 to 5 mK and to a height of up to possibly 32 times the B.C.S. discontinuous jump. Two films exhibited a definite peaking of the low temperature region of this rising heat capacity. This peaking occurred at a point about 20 mK below the MFT transition temperature determined from the conductivity measurements. It is believed that the granular nature of the films broadens the resistive transition to give an arbitrarily wider transition, such that the temperature associated with the onset of order over most of the sample is not in agreement with the T_c^{MFT} determined from a fit to the resistive transition. The phase transition is most likely occurring in the region where the film's resistance is going to zero. An applied magnetic field caused the observed peak of one film to be reduced in height, broadened, and shifted to a lower temperature.

The observed peaking of the heat capacity of these granular aluminum films may be an actual broadening of a much narrower

intrinsic peak due to the distribution in grain size. It might also be the result of a phase transition associated with the coupling between grains due to pair tunneling producing a transition from a "para-coherent" to a coherent state.

These results are in partial agreement with the predicted non-monotonic behavior, but the peak in the heat capacity is much larger than the results of the most recent calculations.¹⁵ However, these calculations are just the first order corrections to the Hartree approximation and the inclusion of higher order terms may cause the heat capacity to diverge.

The measurements were limited to the transition region because of the limited sensitivity in using the film's resistive transition for a thermometer. The requirements of thermal equilibrium in measurements of the heat capacity and the very low mass of the samples make an intrinsic measurement of the film's temperature essential. In this work, an intrinsic measurement was obtained using resistive thermometry. It might also be possible to couple a small tunneling junction to the film, with the film being one of the superconducting electrodes. With this arrangement, one could use a feature of the temperature dependent tunneling characteristic (such as the pair field susceptibility mentioned earlier) to extend the measurements outside the transition region. This would then enable the intrinsic temperature dependence of the heat capacity of the film to be determined outside the transition region.

In conclusion, the heat capacity of a thin aluminum film has been measured in the transition region. A peak has been observed

in a region where the film's resistance is becoming zero. This peak is in partial agreement with predictions, but it indicates a qualitatively larger value than that predicted. This implies that the predictions are only a first order correction to the Hartree approximation and that higher order corrections have to be considered.

List of References

1. H. E. Stanley, Intro. to Phase Transitions and Critical Phenomena, Oxford University Press, N. Y. 1971.
2. L. P. Kadanoff, et.al., Rev. Mod. Phys., 39, 395 (1967).
3. D. ter Haar, Men of Physics: L. D. Landau, 2, Pergamon Press, New York, 1969. See pg. 61 which is a translation of the original paper appearing in Phys. Z. Soviet Un. 11, 26 (1937).
4. J. Bardeen, L. N. Cooper, J. R. Schrieffer, Phys. Rev. 108, 1175 (1967). A comparison can be made from the presentations in Superconductivity of Metals and Alloys by P. G. De Gennes, W. A. Benjamin, New York (1966). A review article showing the explicit relationship is given by M. Cyrot, Rep. Prog. Phys. 36, 103 (1973). It was the work of Gor'kov (Sov. Phys. JETP 9, 1364 (1959) that showed that Ginzburg-Landau theory is just a limiting case of B.C.S. near T_c (i.e., $\Delta = V \langle \psi_+ \psi_+ \rangle$, the pair potential).
5. H. Schmidt, Z. Physik 216, 336 (1968).
6. R. A. Ferrell, J. Low Temp. Phys. 1, 241 (1969).
7. W. E. Masker, S. Marčelja, R. D. Parks, Phys. Rev. 188, 745 (1969).
8. P. A. Lee, S. R. Shenoy, Phys. Rev. Letters 28, 1025 (1972).
9. S. Grossman, P. H. Richter, C. Wessel, Solid State Comm. 11, 433 (1972).
10. W. E. Masker, S. Marčelja, R. D. Parks, Phys. Rev. 188, 745 (1969).
11. Shang-keng Ma, "The Renormal. Group and the Large n Limit", preprint, U of Calif., San Diego, La Jolla, Calif., 92037. It should appear in the J. Math Phys. about August 1974.

12. L. W. Gruenberg, L. Gunther, Phys. Letters 38A, 463 (1972).
13. L. Gunther, L. W. Gruenberg, Solid State Comm. 10, 567 (1972).
14. A. J. Bray, G. Rickayzen, J. Phys. F: Metal Phys. 2, L109 (1972).
15. D. J. Scalapino, R. A. Ferrell, A. J. Bray, Phys. Rev. Letters 31, 292 (1973). The "Screening" approximation itself is discussed in the paper by R. A. Ferrell, D. J. Scalapino, Phys. Rev. Letters 29, 413 (1972).
16. D. J. Thouless, Ann. Phys. 10, 553 (1960).
17. A. P. Levanyuk, Sov. Phys. - Solid State 5, 1294 (1964).
18. W. Weller, Phys. Letters 5, 35 (1965).
19. T. Tsuzuki, Progr. Theoret. Phys. 41, 296 (1969).
20. L. P. Kadanoff, G. Laramore, Phys. Rev. 175, 579 (1968).
21. H. Schmidt, "Fluctuation in Superconductors Above T_c ", Int. Low Temp. Conf. #11, pg. 798 (1968).
22. H. Schmidt, Z. Physik 232, 443 (1970).
23. L. G. Aslamazov, A. T. Larkin, Phys. Letters 26A, 238 (1968).
24. L. G. Aslamazov, A. T. Larkin, Sov. Phys. - Solid State 10, 875 (1968).
25. K. Maki, Progr. Theoret. Phys. 40, 193 (1968).
26. J. B. Parkinson, J. Phys. F: Metal. Phys. 2, 966 (1972).
27. R. F. Hasing, R. R. Hake, L. J. Barnes, Phys. Rev. Letters 30, 6 (1973).
28. R. F. Hasing, J. W. Wilkins, Phys. Rev. B7, 1890 (1973).
29. S. Grossmann, P. H. Richter, Physics Letters 33A, 39 (1970).
30. B. R. Patton, Phys. Rev. Letters 27, 1273 (1971).

31. S. Marčelja, Phys. Letters 35A, 335 (1971).
32. W. E. Masker, S. Marčelja, R. D. Parks, Phys. Rev. 188, 745 (1969).
33. R. A. Craven, G. A. Thomas, R. D. Parks, Phys. Rev. B7, 157 (1973).
34. J. F. Cochran, Anns. Phys. 19, 186 (1962).
35. L. J. Barnes, R. R. Hake, Phys. Rev. 153, 435 (1967).
36. R. F. Hasing, R. R. Hake, L. J. Barnes, Phys. Rev. Letters 30,
6 (1973).
37. G. D. Zally, J. M. Mochel, Phys. Rev. Letters 27, 1710 (1971).
38. G. D. Zally, J. M. Mochel, Phys. Rev. B6, 4142 (1972).
39. R. L. Greene, C. N. King, R. B. Zubeck, Phys. Rev. B6, 3297 (1972).
40. W. Buckel, Ch. Ohlerich, "Specific Heat of Strongly Disordered
Crystalline and Amorphous Films", Int. Low Temp. Conf. #13, Boulder,
Colorado, August 1972.
41. G. Rickayzen, A. J. Bray, "Fluctuations in Superconductors:
The Screening Approximation in Two Dimensions", to be published
in J. Phys. F: Metal Phys. 3 (August 1973).
42. Note that this assumes that ΔV is a constant voltage source. If
the problem is formulated with a constant current source and
continuity of currents is used ($I_{DC} = I_R + I_Z$), the results
differ only by a constant which is possibly unity.
43. R. S. Thompson, M. Strongin, O. F. Kammerer, J. E. Crow,
Physics Letters, 29A, 194 (1969).
44. R. V. Carlson, A. M. Goldman, "Superconducting Order Parameter
Fluctuations Below T_c ", submitted for publication to the Physical
Review Letters (August 1973).

45. J. T. Anderson, indirect private communication.
46. R. E. Glover, Physics Letters 25A, 542 (1967).
47. P. Pellan, G. Dousselin, H. Cortès, J. Rosenblatt, Solid State Comm. 11, 427 (1972).
48. Measurements were made without a transformer with large temperature excursions ($\sim .1$ mK) that verified the results obtained with a transformer and using this equivalent circuit.

Appendix A. A.C. Bridges and Thermometry.

The thermometry for the experiment involved accurate measurement of the resistance of both carbon and Germanium resistors, the later being commercially available and calibrated¹ by a log R (resistance), log T (temperature), extrapolation between points traceable to the N.B.S. (absolute accuracy ~ 1 mK).

The A.C. Resistance Bridge (Figure A-1) is a variation of the bridge used previously in our laboratory.² The bridge is referenced with a voltage from a lock-in amplifier (P.A.R. - #HR-8) and the signal from the null output is phase sensitive detected by the lock-in amplifier until both the ratio box and capacitance box settings give a null voltage on the lock-in output. The equation for the voltage output of the HR-8 is:

$$V_{out}^{HR-8} = \frac{1}{\tau} \int_0^{\tau} dt I_R \left\{ R_s \left[1 + R_s^2 \left(\frac{L' - C'}{\omega L' C'} \right)^2 \right]^{-1/2} \right\} e^{i\phi_s} \\ \times G \alpha \left\{ 1 - e^{i(\phi_x - \phi_s)} \left[\frac{R_x \left[1 + R_x^2 \left(\frac{L - C}{\omega L C} \right)^2 \right]^{-1/2}}{\alpha R_s \left[1 + R_s^2 \left(\frac{L' - C'}{\omega L' C'} \right)^2 \right]^{-1/2}} \right] \right\} e^{-i\Delta\phi_r} \quad (A-1)$$

where

$$\omega \sim 2.4 \text{ KHz} \quad \alpha = \text{bridge factor including ratio setting} \\ \phi_s = \tan^{-1} \left[\frac{\alpha R_s (L' - C')}{\omega L' C'} \right] \quad \phi_x = \tan^{-1} \left[\frac{R_x (L - C)}{\omega L C} \right]$$

A.C. RESISTANCE BRIDGE

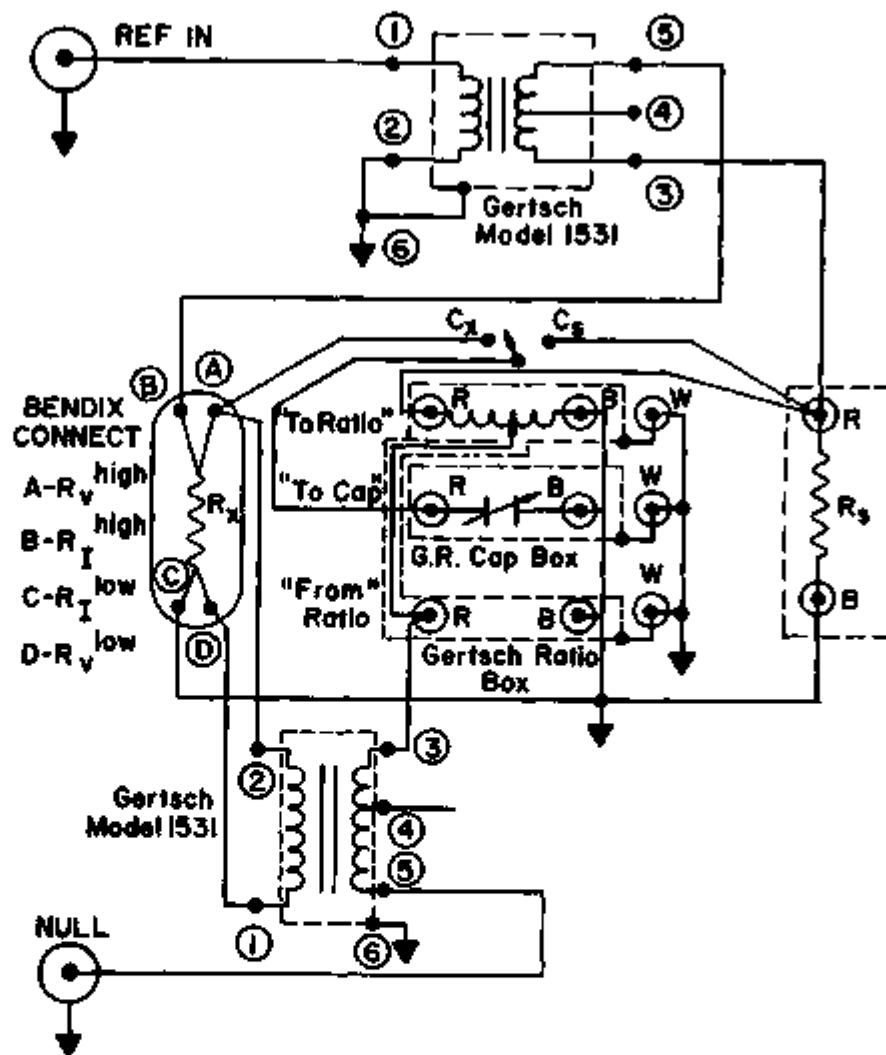


Figure A-1.

(continued)

L, C are inductance and cap. impedances on the R_x
(unknown resistor) side;

L', C' are inductance and cap. impedances on the R_s
(standard resistor) side;

G, τ, I_R are gain, time constant, and reference current for HR-8;

$\Delta\phi_r$ = difference in reference current phase and mixer signal
phase which is set on the HR-8.

(A-1)

The bridge is balanced by setting C_x , or C_s to zero, and the ratio setting is set to zero. The lock-in output is maximized with the phase setting $\Delta\phi_r$ for low sensitivity settings (G-gain). The ratio is changed until a null reading is read. The phase is changed by 90° ($\Delta\phi_r + \Delta\phi_r + 90^\circ$) and the cap. setting is changed until a null is read. The time constant (τ) is set at some appropriate value (~ 1 sec). The above procedure is continued for higher sensitivities, until the thermal fluctuations of R_x enter in and inhibit more sensitive nulls. For $R_x \sim 10K$, $I_R \sim 10^{-6}$ amp, these are about 10 nV, or 10 μ K fluctuations. At this state equation (A-1) reduces to:

$$V_{out} = 0 \Rightarrow \left\{ 1 - e^{i(\phi_x - \phi_s)} \left[\frac{R_x \left[1 + R_x^2 \left(\frac{L-C}{\omega LC} \right)^2 \right]^{-1/2}}{\alpha R_s \left[1 + R_s^2 \left(\frac{L'-C'}{\omega L'C'} \right)^2 \right]^{-1/2}} \right] \right\} \approx 0$$

$$\alpha R_s \sim R_0$$

$$\Delta\phi_r \neq 0$$

since the coeff. is non-zero

(A-2)

$$\begin{aligned}
 &V_{out} \approx 0 \\
 &(L'-C')/L'C' \approx (L-C)/LC \\
 &\Delta\phi_r = 90^\circ
 \end{aligned}$$

combine with (A-2) $\rightarrow \phi_s \approx \phi_x$
and definition of ϕ_s, ϕ_x .

(A-3)

$$\alpha R_s \approx R_x \frac{\left[1 + R_x^2 \left(\frac{L-C}{\omega LC}\right)^2\right]^{-1/2}}{\left[1 + R_s^2 \left(\frac{L'-C'}{\omega L'C'}\right)^2\right]^{-1/2}}$$

(A-4)

if one chooses the standard near to R_x then to second order:

$$R_x \approx \alpha R_s$$

with a known "unknown" one can measure the bridge factor with the ratio setting and thus measure unknowns, just by knowing the ratio setting.

It should be noted that the bridge factor is dependent on the value of R_x , and thus all experimental values are corrected with this in mind. Also, if one is close to null, and $V_{out} \approx 0$, one can approximate equation (A-1) by:

$$V_{out} \approx I_R G R_s \alpha \left[1 - R_x/\alpha R_s\right]$$

which is linear in R_x and thus to about 5% in experimental cases, one can use the off null voltage as a linearly varying function of R_x .

(A-5)

By setting the bridge balance to the center of the varying value of R_x , and knowing the starting value of R_x , and the final value of R_x , one can approximately continuously monitor R_x , by monitoring the off null changing voltage (subtracting off the D.C. base line) out

of the HR-8. This method is used not only to obtain a continuous temperature reading, (for example taking the resistive transitions as a function of the germanium resistance), but to use the voltage as a temperature error in an A.C. servo loop (as will be discussed later).

The Self-Balancing Bridge (Figure A-2) is a modification of the A.C. Bridge, where a variable resistor (optically coupled transistor) is added to the standard resistor ($R_S \Rightarrow R_S + R_T$ (variable)). The off null of the HR-8 is filtered to allow essentially only D. C. changes (see Filter Box in a later appendix) and is converted into a negatively feedback current (by a $V \rightarrow I$ circuit, see Ref. 2) that changes the value of R_S to balance the changes of R_X . By monitoring the current fed back, one has a means of knowing the changes of R_X with a balanced bridge. For $R_T = 1K$, $R_S = 10K$ one can get a change in $R_S \sim 30\Omega$ for a current of $0 \rightarrow 50$ ma. By appropriate choices one can match the values of R_T and R_S to cover a sizeable range of self-balancing operation.

The A.C. Bridge was also used to measure the resistance of the superconducting films used in the experiment. One should note that at balance, there are a number of sources of error, one being the current flowing in the film causing heating, and another being the lead's resistance from the film giving a potential drop and noise error in the measurement. When one has very low resistances ($\sim .5\Omega$), it is difficult to get accurate readings with the above bridges, and hence, a Kelvin Bridge (Figure A-3) was constructed.

SELF-BALANCING BRIDGE

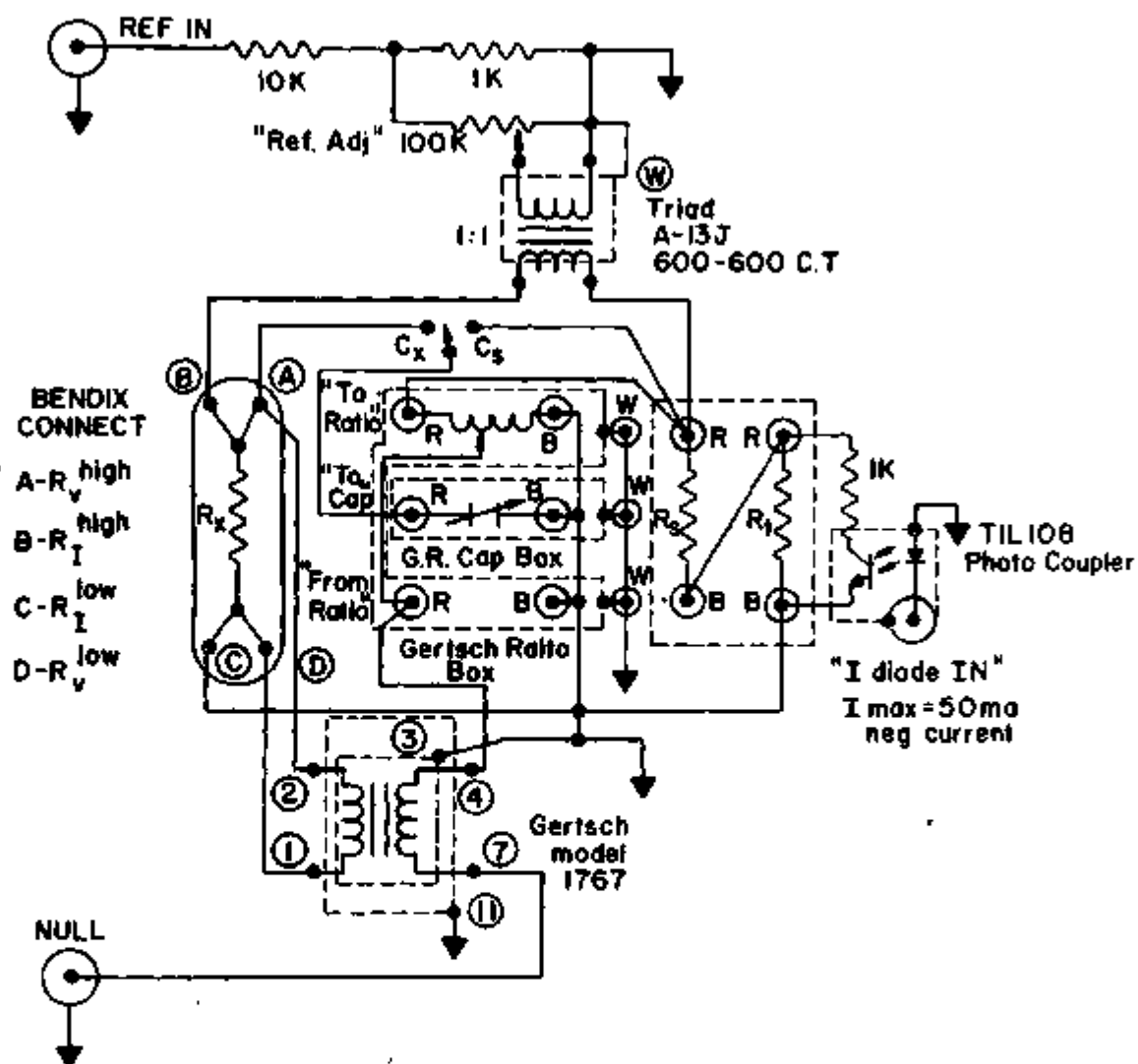


Figure A-2.

A.C. KELVIN BRIDGE *

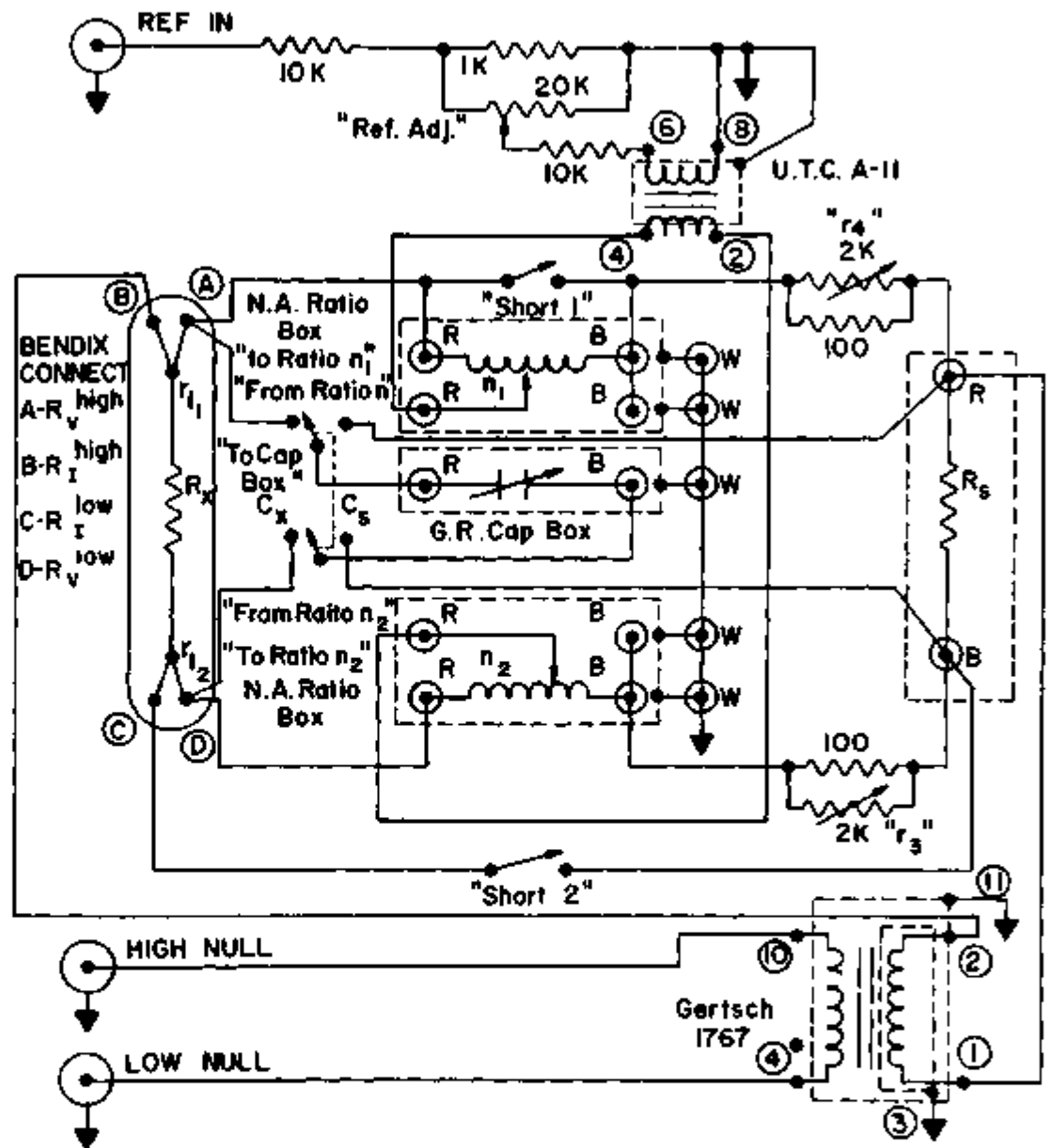


Figure A-3.

* Sometimes called a Double Ratio Bridge.

This form originally was a resistance ratio bridge, but due to the sensitivity of A.C. phase sensitive detection schemes, and accurate ratio boxes ($1pp10^7$) this bridge has been modified to an impedance bridge. Hill and Miller³ did the original work, which has eventually led to a commercially available unit (although quite expensive) of similar design.⁴ With the commercially available 16 bit D/A converters, one could expand this idea to a self-balanced high resolution bridge. It should be noted that the bridge is symmetric under an interchange of the reference and detector. Also, at null the current in the unknown resistor is zero, and the lead resistances are nulled out of the measurement (but, changes in them are a large source of noise, i.e., bumping cables). The procedure for nulling is as follows:

- 1) Adjust ratios n_1 , n_2 as for other A.C. bridge until a null is reached with "short 2" in place. Then

$$\frac{n_1}{1-n_1} \approx \frac{n_2}{1-n_2} \approx \frac{R_x}{R_S}$$

- 2) Put in "short 1" as well as "short 2" and re-null bridge by adjusting r_4 . Then we have:

$$r_{L1}/r_4 \approx \frac{n_1 - r_{L1}}{(1-n_1) - r_4}$$

- 3) Take out both shorts and adjust r_3 for a null. Then we have:

$$r_{L2}/r_3 \approx \frac{n_2 - r_{L2}}{(1-n_2) - r_3}$$

- 4) Put "short 2" back in and readjust n_1, n_2 . This procedure is continued until all steps give nulls. Then:

$$R_x = \alpha \left(\frac{1-n_1}{n_1} \right) R_s \quad \text{where } \alpha \text{ is the bridge factor.} \quad (\text{A-6})$$

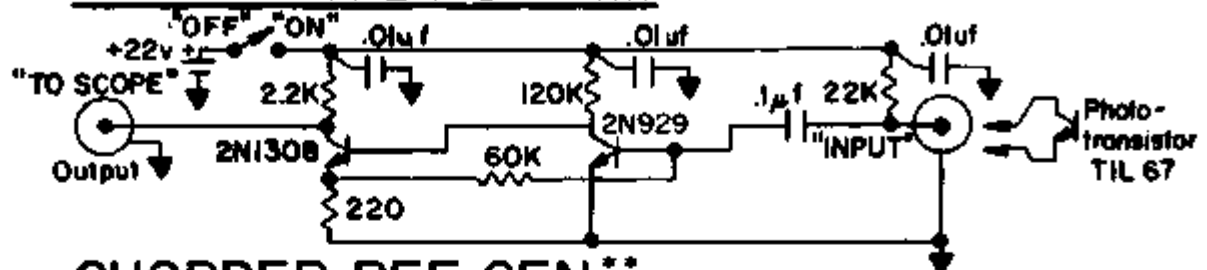
One should always let $n_1=n_2$ in all measurements to speed up the process. There are ganged transformers that work quite well in place of n_1, n_2 , so that one always has $n_1=n_2=n$. (An example is the Gertsch Model #1000 A. C. Ratio Standard). This bridge has an accuracy and sensitivity for low power dissipations ($\sim 10^{-12}$ watts) of less than $1 \text{ m } \Omega$.

The Germanium resistors were fitted to a logarithmic series in temperature using the calibrated points supplied by the manufacturer. A table was generated that allowed resistance measurements to be looked up for their temperature equivalent in steps of about $8 \mu\text{K}$. The carbon resistors and the superconducting films were calibrated from the values of the Germanium resistor when both were in thermal equilibrium. These bridges allowed temperature measurements to better than $10 \mu\text{K}$ and resistance measurements to better than 1 part in 10^3 (for low resistances $\sim 1 \Omega$) and to 1 part in 10^5 (for high resistances $\sim 10 \text{ K } \Omega$).

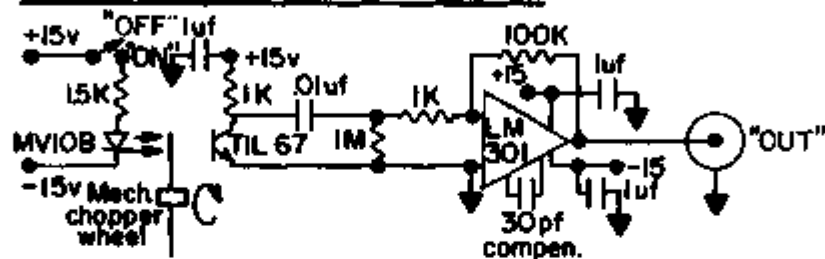
Appendix B. Optical Systems.

Since the experiment involved optical heating, systems for heating the film, as well as detecting correct system operation, were constructed. Light Emitting Diodes (L.E.D.) were used first (being in the visible region for ease of optical alignment, etc.). Their output was monitored in the low temperature cryostat with Si photo-transistors, using the Detector Box shown in Figure B-1. The operation of these devices at low temperatures is discussed elsewhere (see Ref. 5). The diode and detector were optically coupled in a block of lucite, that was at 4.2 K, and the emitted radiation was shone onto the sample via a plastic light guide (see Ref. 6). This system could heat the sample at high frequencies (~ 100 KHz), at relatively high powers (~ 500 μ watts). The system had certain drawbacks that led to its termination. The LED's, while putting out high powers, are quite inefficient and dissipate to the local environment ~ 100 m watts of power which is quite unacceptable for a low temperature environment. They also have a threshold before they emit light, which limits them for low power use. But, their major drawback is that relatively large currents (~ 50 ma) are introduced into a low signal level environment and produce undesirable electrical coupling that is indistinguishable from optical heating, since the optical signal and the driving voltage are at the same frequency. For these reasons the LED system was discarded.

DETECTOR BIAS + AMP. *



CHOPPER REF. GEN. **



OPTICAL ISOLATOR ***

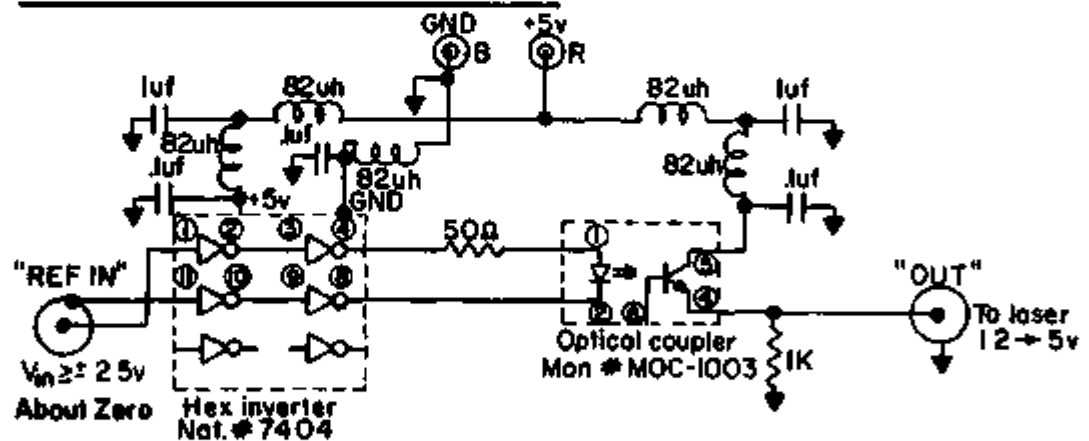
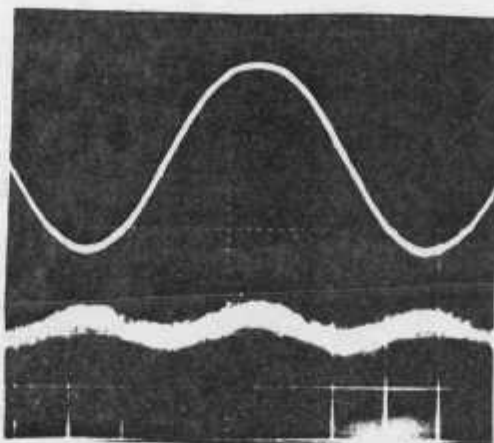


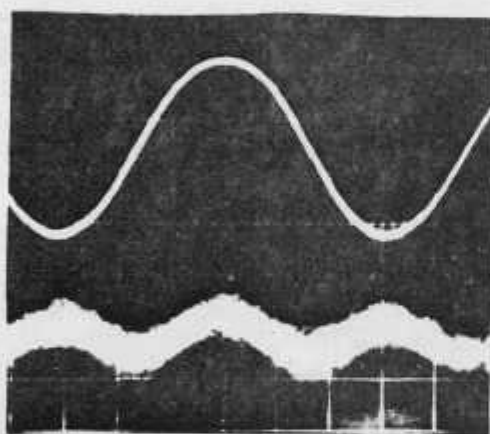
Figure B-1.

* See Texas Inst. Appl. Notes. ** Built by David Winkler.

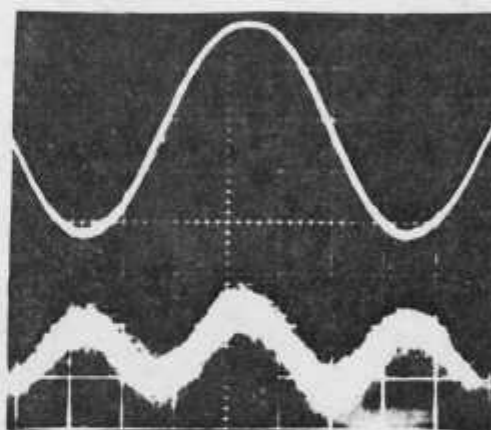
*** Built by Gary Wandersee.



T = 300 K



T = 77 K



T = 4 K

Figure B-2

Lower trace is the light intensity of light bulb (lower trace @ 10 mv/div) as seen by a detector (T1L67 Photo-transistor) at room temperature optically coupled to the light bulb via plastic light guide. The detector output was monitored with the circuit shown in Fig. B-1. The light bulb was driven by a constant voltage source (upper trace @ 1 v/div) at a frequency of 10 KHz (Horizontal axis @ 20 μ sec/div). There is little change in the light output for the three temperatures shown.

The next optical system used involved very small tungsten filament light bulbs (see Ref. 7). The bulbs will operate at 4K and experience no problems in cycling to room temperature. It is necessary, however, to have the entire bulb heat sunk in some fashion (i.e., in an oil or LHe bath) in order that thermal gradients won't occur along the length of the bulb. It is believed that this is the cause for observed bulb failure in gaseous He at 4K. The bulb has a continuous D.C. power output from zero up to about 400 μ watts. When the bulb is operated in an A.C. mode, the power output is a combination of an A.C. power and a D.C. power, with the ratio of A.C. to D.C. power decreasing linearly as a function of frequency, probably due to the inductive nature of the spiral filament (both physically and thermally) affecting the A.C. power, when driven by a constant voltage source. This ratio falls off to about 10^{-4} at 10 KHz. When the bulbs are driven by a constant voltage source, the power emitted from the bulb, varies as the square of the driving voltage, and hence a driving frequency of ω , will be emitted at twice the driving frequency (i.e., 2ω). Figure B-2 illustrates this point at three different temperatures, and shows that the light emitted is at twice the driving frequency. This method was at first considered an asset, because the signal would be detected at twice the driving frequency, and thus reduce coupling problems encountered earlier. But, the maximum rejection of the detection methods was only 80 db, and thus a coupled signal at frequency ω , detected at 2ω , would look like a real 2ω signal. Extensive measurements reduced

this coupling to a level where there was no longer any signal.

It was because of the problem in distinguishing whether a detected signal was due to optical heating or E.M.I. coupling, that the experiment finally went to a room temperature optical source. The light was coupled via a plastic light guide, that was thermally sunk to the 4K bath, and terminated in a copper sink from which it shone onto the sample. The light guide had an optical vacuum feed through that allowed separation of the light guide between the cryostat and the room temperature optical source. Due to the transmission characteristics of the light guide (Ref. 6), the heat leak of the light guide was negligible. This optical system reduces the entering light from the room temperature source by a factor of 10^3 . Thus, this reduction, together with the small light guide area, caused the need for a relatively large flux room temperature source. The advantage of this method is that one can block the light entering the guide, without changing the electrical structure, and thus distinguish between optical heating and electrical coupling.

A number of room temperature sources were used. A large movie light output was optically focused and mechanically chopped before it entered the light guide. A reference signal for the detection methods was derived using the circuit shown in Figure B-1. This was three times the minimum light output needed, but the frequency of this optical source (1 KHz) was not readily adjustable due to the mechanical chopping nature. Since frequencies greater

than 1 KHz were desired, a large (10 mW) HeNe laser was used that was modulated by varying the D.C. discharge current at frequencies up to 50 KHz. But, it had inherent stability problems, and due to its size (4 ft. long) had to be coupled over a long distance to the cryostat which resulted in considerable beam attenuation. Finally, a D.C. modulated 1 mW He-Ne laser (Metrologic Model #382) was used. It could be coupled quite closely to the cryostat, and thus provided a variable frequency (D.C.-500 KHz) light source of sufficient size to produce an optical heating signal. There were at first EMI coupling problems due to the radiation of the D.C. modulating plasma in the tube, but an isolator (Figure B-1) was constructed that removed these problems. Thus, although some of the earlier optical heating sources satisfied the heating requirements, the modulated He-Ne laser, optically coupled to the sample, provided the most versatile and convincing source.

Appendix C. Cryostat and Isolation.

Because the experiment involved measuring very low level signals, particular attention had to be given to electrical isolation. But also, because a vibrating film in a magnetic field would generate noise currents, isolation from vibration and magnetic fields also had to be provided.

Figure C-1 shows the basic dewar system with the different isolations. Vibrational isolation was provided by using bellows coupling links for all hoses to the dewar stand, and by mounting the stand on a vibration isolation platform. Tests were made using step hammer pulses as a driving force, and an accelerometer as a detector. The springs on the lower mount isolated frequencies up to about 200 Hz by a factor of 20. The "waffle" pad isolated frequencies up to about 600 Hz by a factor of 2, and the foam pad-lead combination isolated frequencies up to a few KHz by a factor of 10. The system is essentially 3 high pass filters in series, with the last filter being the highest cutoff. This gives the overall system the ability to essentially reduce vibrations by a factor of 400 for all low audio frequencies and below. The system does allow for direct accoustical coupling in the air, but this proved to not be a noise problem.

Magnetic isolation was achieved by three concentric high permeability shields (the third being directly in the He bath, to reduce domain noise). Considerable isolation could be achieved by degaussing the shields. Although direct A.C.

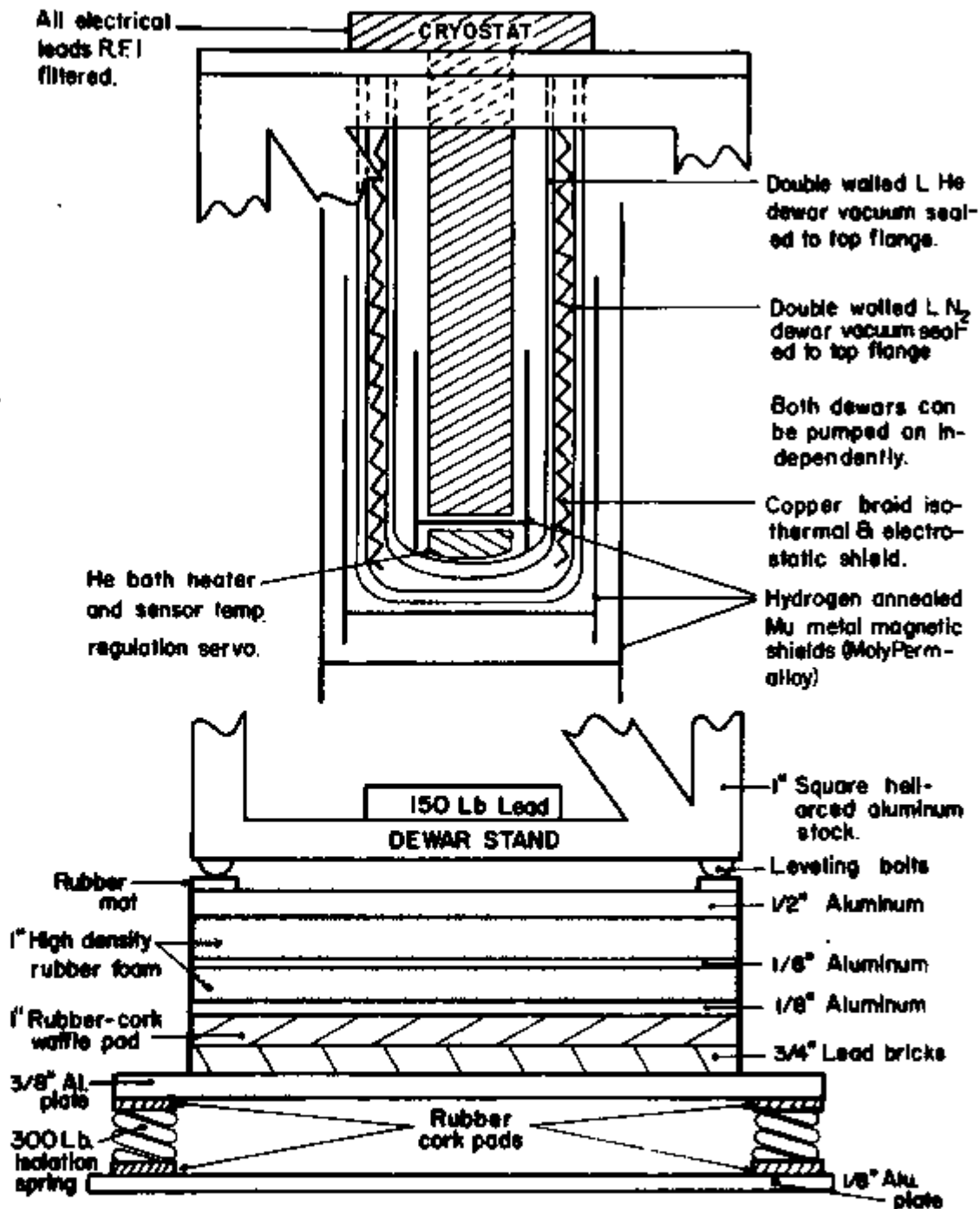


FIGURE C-1

currents in the shields, and low frequency (1 Hz) D.C. currents were tried for degaussing, simple 60 Hz solenoid coils on the shields proved to work best. By using 3 variable transformers in series, at peak currents of about 10 amps, one could slowly reduce the degaussing field to a negligible amount. Best results were achieved by first reducing any magnetization in all three shields, and then degaussing from the outer shield first, to the inner shield last. Magnetic field (both transverse and axial) profiles were taken using a H.P. ammeter with a magnetometer probe (flux gate type). The field had two field reversals about the average minimum, which was about 7×10^{-5} gauss at about 1/3 the way up from the bottom of the inner shield. This was also the region occupied by the sample when the cryostat was correctly positioned. It is interesting to note that the inner shield was removed for a brief time and placed in the earth's field, and then returned to its original position. It gained magnetization of about 1μ gauss/sec which would mean it would take about 10 days to accomplish a linear saturation in the earth's field.

The dewars were the usual double walled glass dewars. They were sealed to the upper flange by rubber washer seals to facilitate pumping on both the LN₂ and LHe baths. Copper braid was hung around the He dewar above the ring seal, and allowed to be in contact with the LN₂ bath. This was to place an isothermal shield around the He dewar (with some E.M.I. shielding abilities) and to provide a isothermalizing effect on the LN₂ bath when it was pumped on. Due to the layered freezing effect when pumping

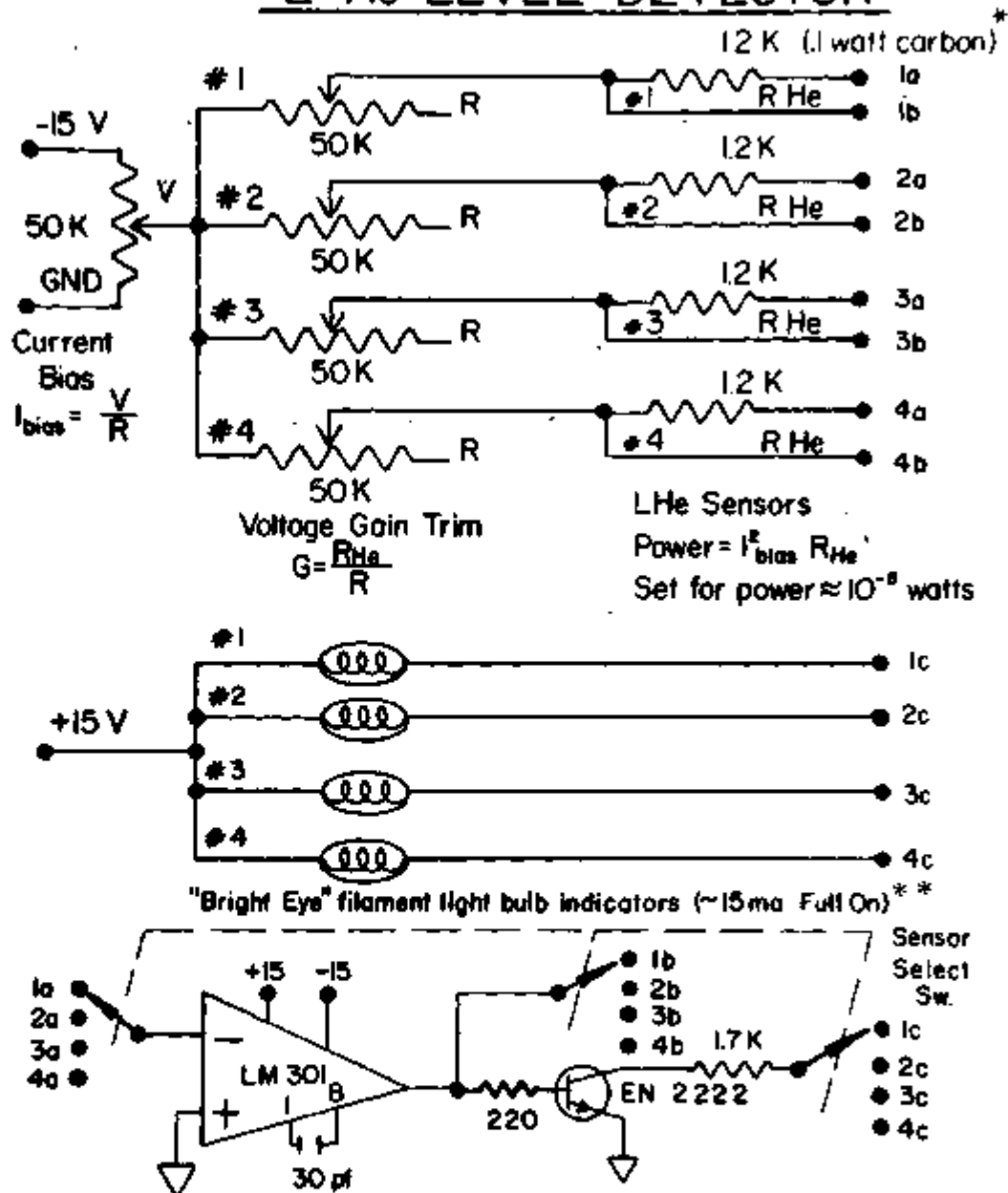
on LN₂ and the sequential "explosion" of the lower liquid vapors through the frozen N₂ crust, the bath was only slightly pumped on for test purposes, and was never done so during a run. The main purpose was to reduce vibrations from the bubbling LN₂, but this never proved to be a problem. The He bath was pumped to about 1.6°K and servoed to about 1 mK with a carbon resistor-manganin heater combination.

Figure C-2 is the schematic for the He level detector system. The sensors were in a teflon tube that ran down the inside of the He dewar and was held in place with masking tape. The indicators were on the front side of the dewar stand and at the same spatial points as the sensors. Thus, one could see when there was no longer LHe above a certain level by switching to the appropriate sensor. The system only needed minor trim adjustments over a two-year period of use. The indicators were essentially 100% accurate.

The cryostat (See Figure C-3) consisted of an outer O.F.H.C. copper can that was immersed in the bath. All leads entering the can had been electrically isolated using sub-miniature "pi section" low pass filters* that gave about 60 db filtering above 5 MHz. The leads were in direct contact with LHe and pass through epoxy feed thrus (Stycast) into the outer can. The inner can was attached to a copper tube thermally tied to

*They were a combination of the Allen Bradley "pi section" kit CK68-5N in series with a Lenox-Fugle 82 μ h shielded inductor. This design was suggested by W. Wehmann.

L He LEVEL DETECTOR



OPERATION: Gain Trim is adjusted for light "just on" with sensor in L He with particular current bias setting

- * Resistors are inside Teflontube on side of He dewar
- ** Displayed on dewar stand

Figure C-2.

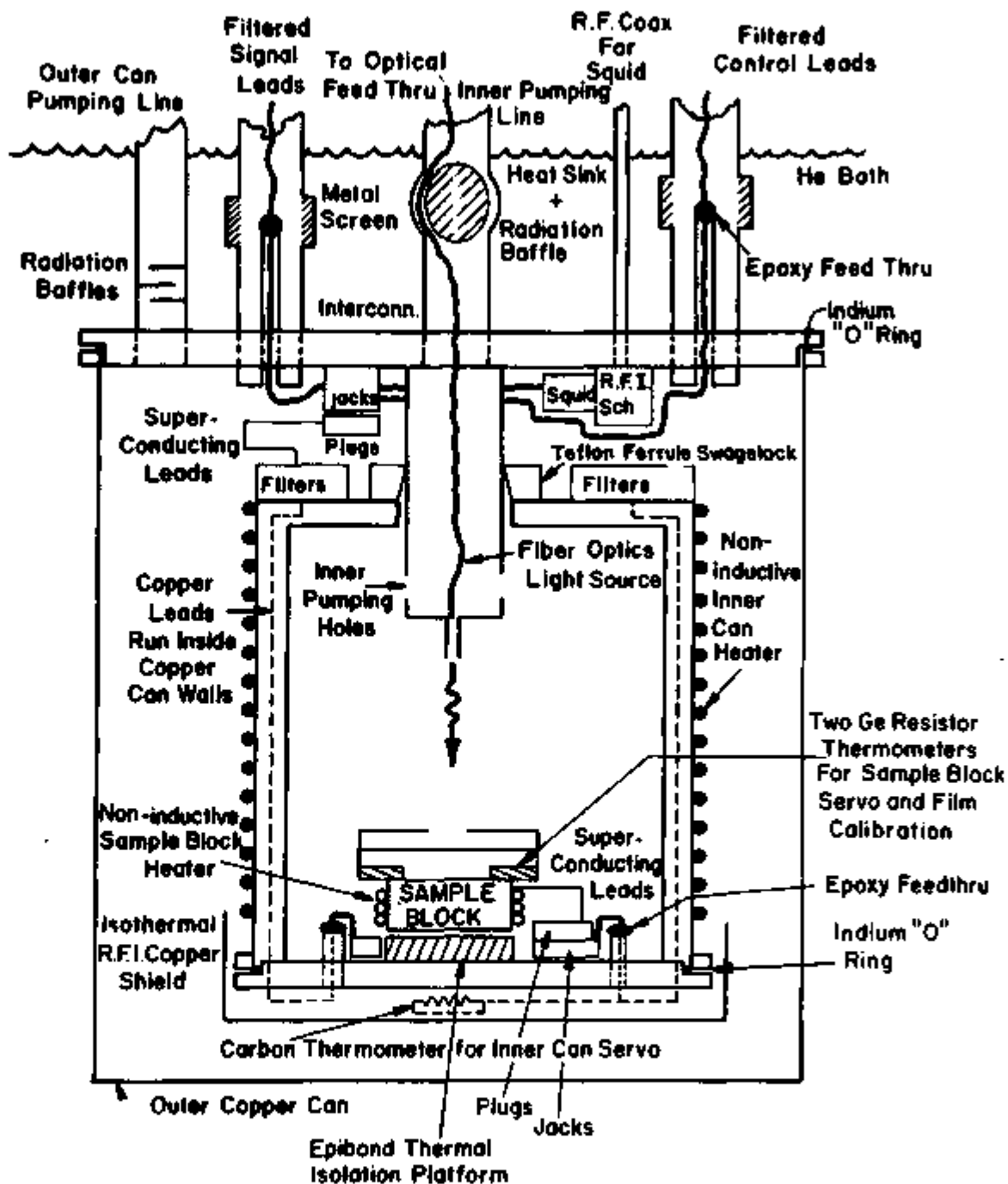


Figure C-3. Cryostat for Experiment.

the bath by a "swage lock" with a teflon ferrule in order to provide thermal isolation, and facilitate optical focusing of the light source onto the film sample. The fiber optics used to conduct the light from the room temperature source, ran down the inside of the inner can pumping line and was thermally tied to the bath. The SQUID system was completely shielded (see SQUID section) so that no R. F. could "leak" into the low level signal environment. To further facilitate this, the inner can was completely electrically shielded, and all leads entered a second set of filters that gave attenuation above about 10 MHz at 4°K. The inner can was thermally isolated from the outer can (the one in contact with the bath) by using superconducting leads. It was independently servoed to provide a temperature regulation independent of the bath. Inside, and thermally isolated from the inner can by an epoxy platform and superconducting leads was the sample block. It was positioned directly below the light source. It had two independent Ge-resistor thermometers (Cryo Cal). One was used for temperature calibration and the other was used with a manganin heater to servo the block. Since 80% of the heat is conducted to those sensors through their wires, care was taken to insure accurate readings. The copper leads were spliced to superconducting leads and pressed in a copper-lense paper sandwich and bolted directly to the sample block to insure good thermal contact. With both cans evacuated one could achieve thermal isolation times of about 20 minutes from the inner can to the outer can and a few hours from the sample block.

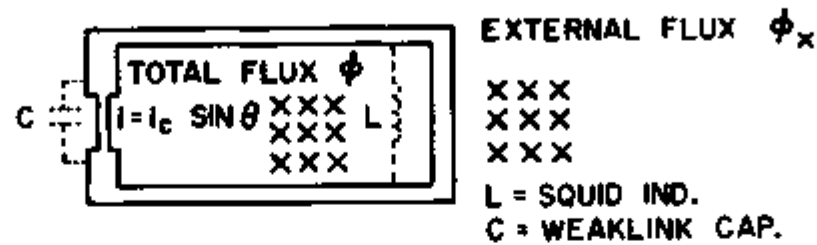
to the outer can. The block could be regulated to about $10 \mu\text{K}$ or better by the servo system as independently measured with the second Ge-resistor.

All measurements were made inside an electrically shielded room. The cryostat and dewar assembly allowed the experiment to be performed in a noise free environment with excellent magnetic, thermal, vibrational, and electrical isolation.

Appendix D. SQUIDS

The SQUID (Superconducting QUantum Interference Device) is a very sensitive device for measuring magnetic fields. In this heat capacity experiment it became obvious that in regions of low thermal sensitivity ($\frac{dR}{dT}$ film was small) the voltages, corresponding to A.C. heating of the film, would be very small. Typically for a $dR/dT \sim 1\Omega/^{\circ}K$, A.C. heating of 10^{-5} $^{\circ}K$, D.C. bias current of 10^{-6} amp, one is trying to measure 10 pico volt signals. For this reason a SQUID system was desired. At first, SQUIDS were made and adjusted without success. Then, a commercially available system came onto the market and was purchased. This system was improved, but finally abandoned for conventional electronics due to problems discussed later. This appendix will not attempt to report on SQUIDS in general, but only as used in this work.

A SQUID is basically a weak link or region with "partial" superconductivity connected in series with a superconducting ring. Figure D-1 shows a weak link, which can be anything from two screws touching (point contact) to an anodized or scribed thin film (bridge). This weak link can be characterized by a current equation that is similar, if not identical to that obeyed by a Josephson Junction. The equation expresses the relationship between the phase differences of the order parameters of the superconductors joined by the link (θ), the maximum current that can flow through the link at zero voltage (I_c), and the



- (1) JOSEPHSON LINK $i = I_c \sin \theta$
- (2) CLOSED SUPERCONDUCTING LOOP $\theta = \phi / \phi_0 + 2\pi n$ $\phi_0 = 2 \times 10^{-7}$ GAUSS-cm²
- ϕ = TOTAL LOOP FLUX
- (3) COMBINED CIRCUIT \Rightarrow NON-LINEAR EQUATION: (EQ. 1+2)

$$\phi / \phi_0 = \phi_x / \phi_0 - (L I_c / \phi_0) \sin(\phi / \phi_0)$$

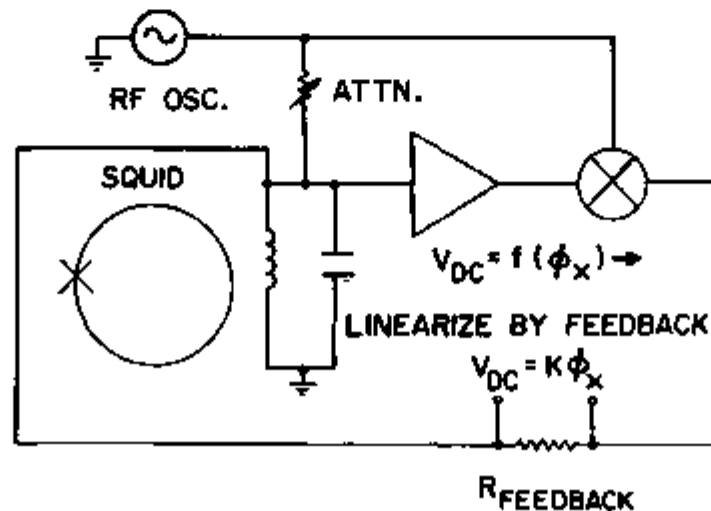


Figure D-1.

actual current in the link (\hat{I}). There is a capacitance associated with the link that will be left out of this introductory discussion. The link is then in series with a closed superconducting loop (with some inductance L), and thus the phase difference around the loop must be related to the total flux in the loop (ϕ) which is defined modulo 2π . By combining these two requirements, a non-linear equation relating the total flux in the loop to the externally applied flux is derived.

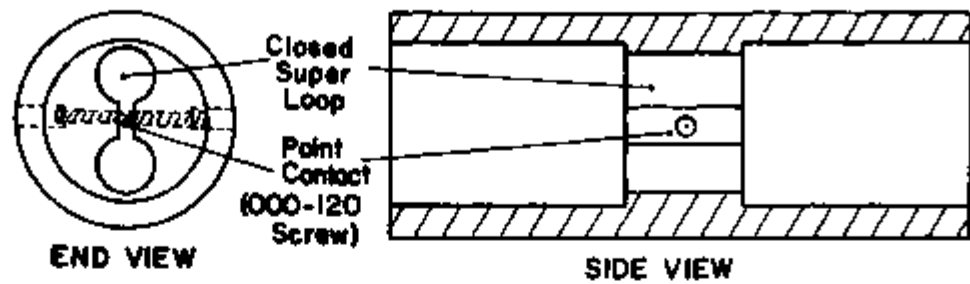
In the real world, one wants to measure changes in the total flux of the loop (coupled in by currents from external experiments). One method of doing this is to weakly drive a tank circuit with an R. F. signal where the coil is placed in the loop. This will cause changes in the total flux to be reflected in a non-linear way in the level of the R.F. driving voltage. By amplifying and mixing out the R. F. driving voltage, one obtains a non-linear voltage function of the total flux in the loop (See Figure D-1). By taking the average of this output voltage and feeding it back as a current (through a high impedance) to the tank inductance, one completes a feedback loop to the superconducting loop, and thus linearizes the voltage function of the total flux in the loop. Then, by monitoring the feedback current, one has a direct measurement of the total flux in the loop, within the bandwidth of the feedback system. There are many treatments of not only the models for the SQUID, but mechanical analogs for the

non-linear equations and other SQUID biasing schemes in the literature.⁸

The particular SQUID used in this experiment was of the symmetric design.⁹ It was made of either Nb or NbTi, was about 1" long and 3/8" in diameter (see Figure 0-2). The point contact (or weak link) was made by a blunt and sharp pointed set of 000-120 screws. The SQUID contains two holes that form two astatic loops, such that the current in the SQUID responds to only gradients in external flux. This feature, along with the superconducting cylindrical extension, allow the SQUID to be somewhat immune to local magnetic noise. Biasing and external signals are coupled into the SQUID through coils placed in the holes.

As mentioned earlier a commercial SQUID system was purchased,¹⁰ which included an adjusting kit. One of the major drawbacks of the SQUID outlined above is that precise adjustment of the point contact is needed in order for the SQUID to behave as a weak link. The S.H.E. system measures the inductance of the SQUID at room temperature, and by setting the screws at a pressure, such that the change of the inductance is about 1% relative to the contact fully open, the SQUID has a reasonable chance of being in adjustment at 4K. By the use of a probe, it can then be tested in a He storage dewar to verify correct adjustment. By this method one can get an adjusted SQUID on the average in about two to three attempts (although sometimes it may take 15 adjustments). Some tricks to mention for success are: 1) blow the gas through the

SYMMETRIC SQUID (Nb or NbTi)



SQUID BIAS

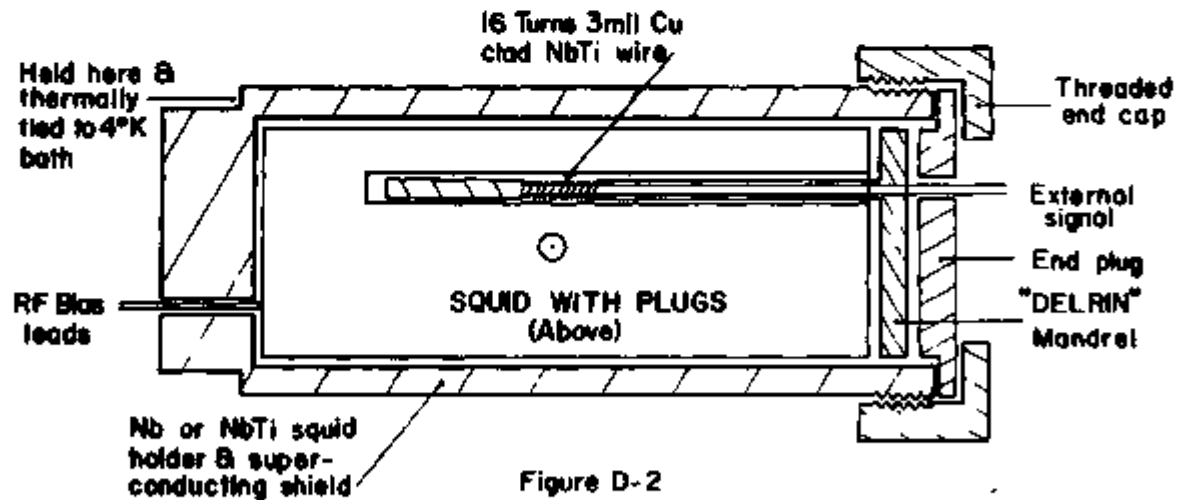
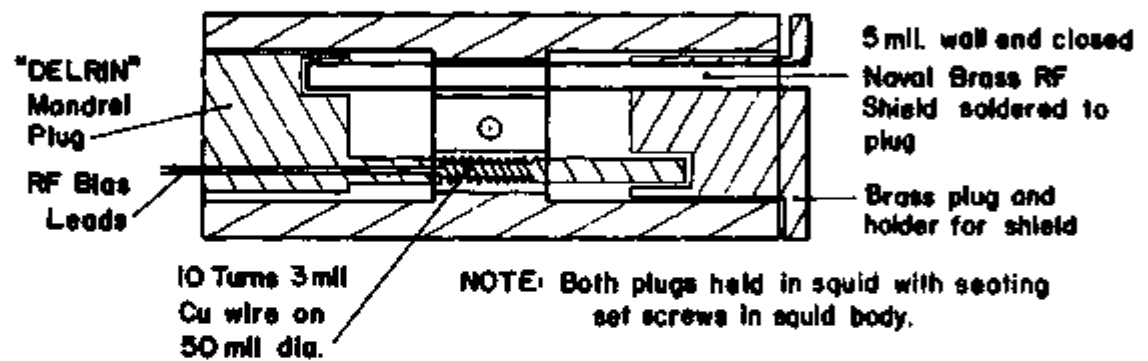


Figure D-2

SQUID just before entering the storage dewar; 2) take at least 5 minutes to enter (and leave) the storage dewar; 3) enclose probe in a bag of He gas upon exit from dewar until it has warmed to room temperature; 4) the pointed screw should be a "blunted" not a "tapered" point so that it doesn't dimple the flat surface or crush itself upon contact. These precautions (along with others mentioned later) will aid in removing thermal effects on the adjustment of the SQUID.

Some basic modifications were done to arrive at the SQUID system developed. First, the SQUIDS used on this experiment had a locknut for the screws that had a smooth flange so that upon "locking" the nut, pressure would be applied evenly, and not disturb the screw setting. Tests with the SQUID system indicated a need for shielding of the RF bias from the experimental signal leads. Figure D-2 shows the symmetric SQUID with a "Delrin" holder for the bias R.F. coil, and a similar brass plug that had a thin-walled tube, to shield against any R.F. leakage out of the SQUID and back into the external signal lead coil which was coupled into the other hole. The whole SQUID was in a superconducting tube that could be mounted at one end in any position in the cryostat. This brass sleeve shielding scheme is similar to that used by the Cornell Group¹¹ except their enclosure was also filled with the gas and sealed off. The system described above was in a vacuum exchange can, and thus did not need to be sealed off.

There were some basic problems with the SHE electronics bias

package that led to the construction of a new electronics system. First, the SHE package had a "Pierce" type oscillator with a third overtone cut crystal. This type of oscillator is primarily used for a fundamental cut crystal and consequently the SHE package would frequently jump to 1/3 the frequency of RF oscillation. Also, this oscillator put out a rather large level signal ($\sim 3v$) that was difficult to attenuate to get the low bias level needed for the SQUID. The SHE package used a rather crude means of a varying ground plane to adjust and attenuate the level. Figure D-3 shows the improved electronics package. By using a tunnel diode oscillator, one maintained a constant frequency source at a much lower level and with a variable gain amplifier feeding a capacitive divider network, a ten turn pot could be used to vary the R.F. level precisely over any predetermined range (ex. ten turns to the first R.F. D.C. field pattern).

The SHE package also used a cascode type preamplifier that feed a series of capacitive coupled R.F. op-amps and was detected with a peak diode detector. The cascode preamplifier has an inherent feedback scheme (Miller effect) that causes self-oscillations due to the capacitive coupling in the transistor from the output to the input. By using a dual gate MOS-FET (capacitive coupling $\sim 1/20$ of normal FET's) for the cascode circuit and using good shielding techniques, this effect could be reduced significantly (See Figure D-4). Also, an inductively coupled R.F. op-amp stage also reduced noise coupling. Finally, a synchronous mixer stage was used (see Figure D-3) to detect the R.F. output,

that, while it had a somewhat reduced average value (not peak detection), it had an increased signal to noise ratio. The whole system was mounted in two sides of a carved aluminum box. It has an overall gain of about 15,000 in the R.F. amplifier, with a Q of 20 and with a peak to peak noise of less than about 1 μ v.

The SQUID was to be used as a null detector in a bridge circuit (See Figure D-5, "Access chimney"). A standard resistor would be in series with the superconducting film resistance and the sensing coil in the SQUID. By biasing the film from a constant current source (I_0), and using the off null of the current in the SQUID coil (fed into the "D.C.IN" part of Figure D-5) to set the level of a counter current (I_F), one then has at null the relation that the ratio of the resistances, $R_{\text{standard}}/R_{\text{film}}$, is equal to the ratio of the currents, I_0/I_F . This allows one to use the feedback circuit of Figure D-5 to continuously measure the film's resistance (at " R_{out} "), providing one knows the biasing current (I_0) and the standard resistance. The standard resistor was made of a short length of manganin wire. All leads were superconducting and each leg of the bridge was shunted by a low valued N.P.O chip capacitor to reduce any R.F. leakage from the SQUID onto the film. The whole bridge was at first built in an enclosure like the one around the SQUID, with leads running to the SQUID and the film, as well as to the "Feedback Box" of Figure D-5, which was mounted on top of the cryostat. Later the bridge was reduced to in line splices of the wires directly on the film sample block (see sample preparation and cryostat sections). Because the

SQUID D.C. BIAS AND FEEDBACK BOX

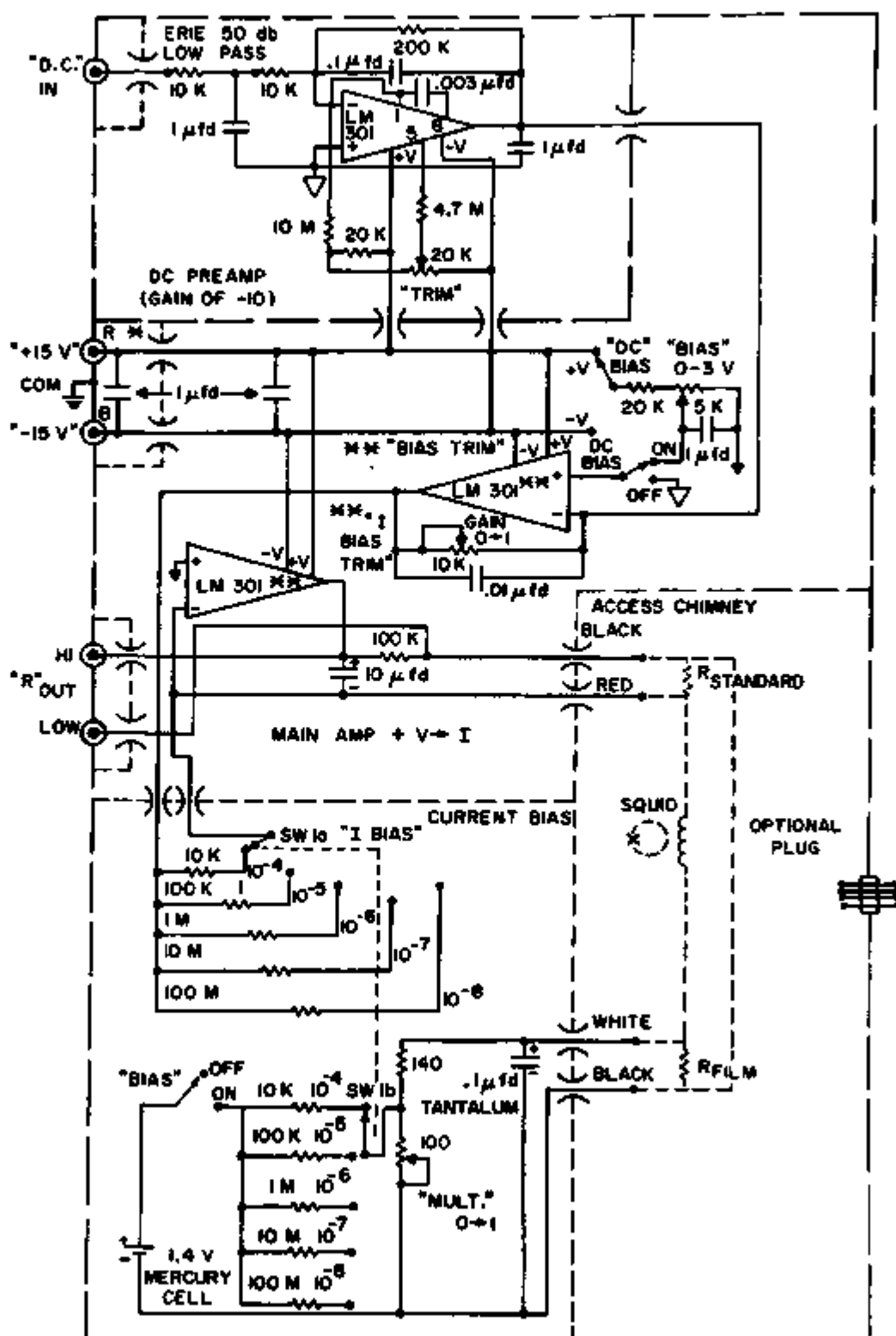


Figure D-5. *1000 pf Cap. Feed-thru unless otherwise noted.
 ** Same trim and compensation as for Preamp.

procedure of the experiment was to measure both the film's resistance and an A.C. heating component of the film's resistance, the feedback current would have to be analyzed not only for its D.C. value but also for the A.C. heating component.

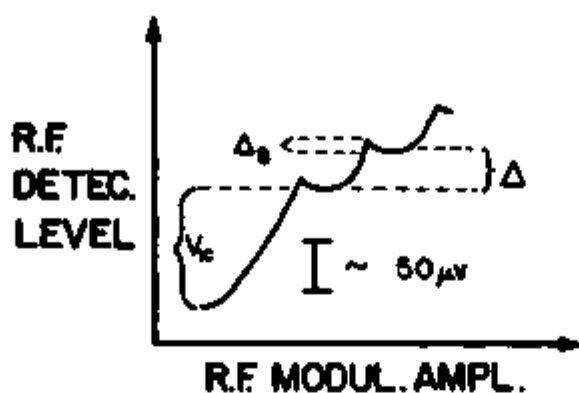
Problems developed with the SQUID system as outlined above, that eventually led to using conventional electronics in the experiment. The first problem was that of the inherent mixing in a SQUID of any two signals due to the non-linear current equation. Mixing was found between any two frequencies used in separate and independent feedback schemes. For example, a D.C. current could linearly vary a phase sensitive detected 1 KHz signal by 180° (i.e., from full positive to full negative maximum detected output). This is essentially like varying the phase at which the P.S.D. is demodulating. Also, frequencies of low (50 Hz) and high (10 KHz) values would mix with each other. This problem would make independent determination of the films resistance (D.C. or low frequency), and the heating component (A.C. or high frequency) quite difficult. One method around this suggested much later by Kamper (at N.B.S. in Boulder) was to use a high frequency carrier (~ 150 KHz) and feed it back with all other signals riding as side bands on this carrier and detected in the feedback loop.

A more important problem that developed was the fact that the critical current of the weak link (I_c^*) was temperature dependent. The SQUIDS were adjusted at 4.2 K in a storage dewar, but were used in a cryostat at about 1.5 K. This changed the critical current behavior enough to make the SQUID inoperative at the desired

operating temperature (1.5 K). Other workers have claimed both immunity to this problem and similar difficulties as mentioned above. The safest solution to the problem is to have a lever arrangement to adjust the contact in situ. The basic behavior observed was a dramatic increase in the critical current of the contact (I_c) as the temperature was lowered. Reference 8 mentions this behavior and also references the work of Strait.¹² Strait's conclusion was that "dirty" contacts (heavily oxidized) had mechanical stability, but a large temperature dependence in the critical current, while "clean" contacts (honed surfaces) had little temperature dependence, but mechanical instabilities. Because of the ambiguous behavior of the adjusted point contact, a run was made, monitoring the SQUID characteristics of a set of NbTi contacts that had been oxidized for 2 hours at 500°F in air. When SQUIDS are R.F. biased, one cannot independently determine the critical current (I_c) since it is related to the kinetic inductance of the SQUID (L), and to the mutual inductance between the SQUID and the R.F. bias coil (M). The measured quantity is the average R.F. voltage level on the tank (\overline{V}_{1c}), at a current just before the current in the loop surpasses the critical current, i.e., at the first "step" in the usual staircase trace of a R.F. average voltage vs. R.F. modulated field. The distance between the steps in the staircase (Δ) is related to the number of flux jumps and the mutual inductance (M). This does not independently determine the critical current of the loop as a function of temperature since the quantities L and M can be temperature dependent. During the test run with the SQUID, an

unusual feature was observed as the temperature was lowered. "Spikes" were observed (Δ_S) at the onset of each step that can be related to further quantities in the experiment. From Reference 9 one can construct a set of three equations (See Figure D-6) that contain three temperature dependent parameters. In this way, the equations were solved by taking the experimentally determined parameters (V_{IC}, Δ, Δ_S) and then extracting the temperature dependence of the critical current (See Figure D-6). This behavior was in qualitative agreement with that of Strait.

It was thus concluded that the reliability of the SQUIDS used was questionable and in view of the complexity of the experiment, and the problems of mixing and therefore ambiguous interpretation, it was decided to do the experiment with conventional electronics.



NOTE :

Actual trace of R.F. level
on oscilloscope Temp.
is= 1.46 K

* From Ref. 9

$$a) V_{ic} = \frac{\omega L L_1 i_c}{M}$$

$$b) \Delta_s = \frac{\phi_0 \omega M}{L}$$

$$c) \Delta = \frac{\omega \phi_0 L_1}{M}$$

 i_c = CRITICAL CURRENT

L = SQUID INDUCTANCE

 ω = RF FREQUENCY

L = RF BIAS COIL INDUCT.

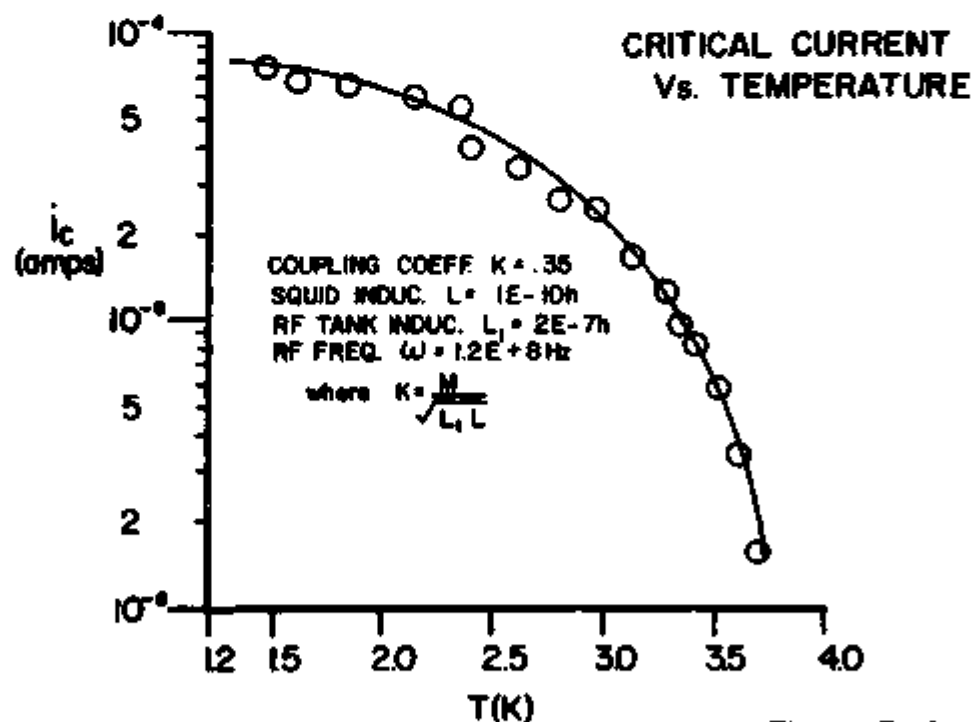
M = MUTUAL INDUCT OF RF
BIAS COIL AND SQUID ϕ_0 = QUANTA OF FLUX

Figure D-6

The upper graph shows the observed "spikes" in the normal staircase pattern of an R.F. biased SQUID. The lower curve shows the critical current (i_c) vs. temperature as determined from the three equations (a,b,c) relating the three temperature dependent experimental parameters (V_{ic} , Δ , Δ_s) and an average value of the slowly varying parameters (K , L) was used in the plot shown.

Appendix E. Functional Differentiation and Numerical Analysis

In the experiment, the resistive transition of the thin superconducting film is used as its own thermometer. The film's resistance is calibrated in temperature when it is in good thermal contact with a Germanium thermometer, and thus from this calibration, the film's temperature can always be determined by knowing its A.C. resistance. A more subtle problem in the experiment is to determine the slight temperature rise (ΔT) associated with the A.C. optical heating, which produces a slight change in resistance (ΔR) and creates an A.C. signal at the optical heating frequency. Using a Taylor series expansion about R_0 , the average resistance value at any temperature where $\Delta R \ll R_0$ for all values of R , we have:

$$\Delta R \equiv |R(T) - R(T')| = \left. \frac{dR}{dT} \right|_{R_0} \Delta T + \frac{1}{2} \left. \frac{d^2R}{dT^2} \right|_{R_0} (\Delta T)^2 + \dots \quad (E-1)$$

where $\Delta T = |T - T'|$

A first order approximation would relate ΔR to ΔT by:

$$\Delta R = \left. \frac{dR}{dT} \right|_{R_0} \Delta T \quad (E-2)$$

This is a crude approximation, since higher order terms are present in most resistive transitions. But, if the interval is small over which the slope of the transition ($\frac{dR}{dT}$) is determined, then a linear approximation will work, and higher

order terms can be neglected. The function $\frac{dR}{dT}(T)$, which is the slope of the resistive transition, was determined by a number of methods. Since in the experimental data taking process, the temperature is increased at a constant rate in time ($\frac{dT}{dt} = r$ (rate)) from below to above the transition, the function that is needed can be modified to the function below:

$$\frac{dR}{dT} = \frac{dR}{dt} \frac{dt}{dT} = \frac{dR}{dt} \frac{1}{r} \quad (E-3)$$

It was independently verified that r was a constant in time by plotting $(T_i - T_{i+1})$ vs. time $(\Delta t \times i)$ to obtain a straight line, where $T_i(\Delta t \times i)$ was the digital form of temperature. Three methods were used to determine $\frac{dR}{dT}$ and hence $\frac{dR}{dt}$. The first two were analog methods that were hindered by analog noise. The third method was a digital technique that was hindered by digital noise due to the sampling. But, by using digital filtering techniques and a fine sampling grid (1020 points), the noise could be significantly reduced. The digital method was used in all subsequent data analysis.

Since the dynamical resistance is a voltage, linearly related to R , then $\frac{dR}{dt} \propto \frac{dV_R}{dt}$. Thus, one only has to differentiate this voltage (V_R). The basic analog circuit for differentiation is shown in Figure E-1. It is simply a high pass filter, such that the fastly varying functions are not attenuated, and hence it is a differentiator. The problem is that noise pulses will also get

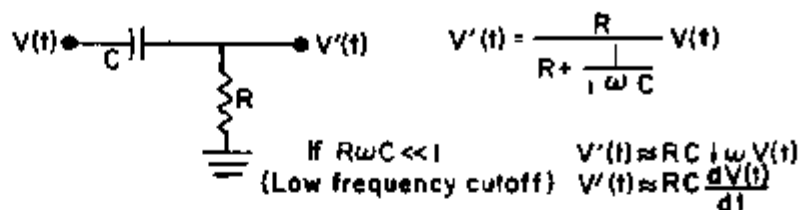
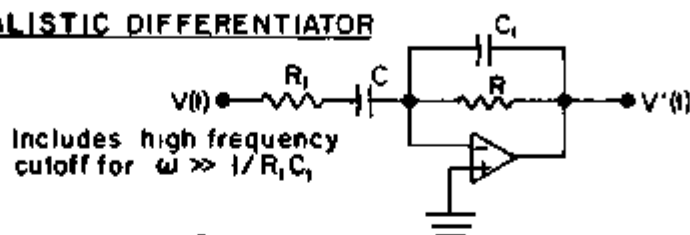
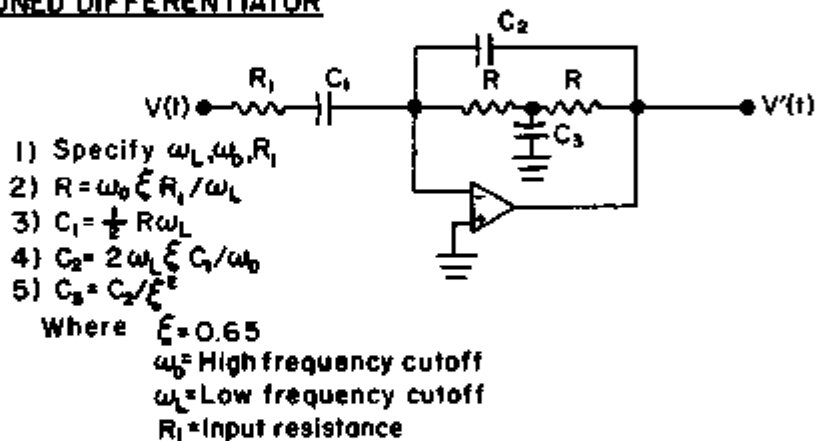
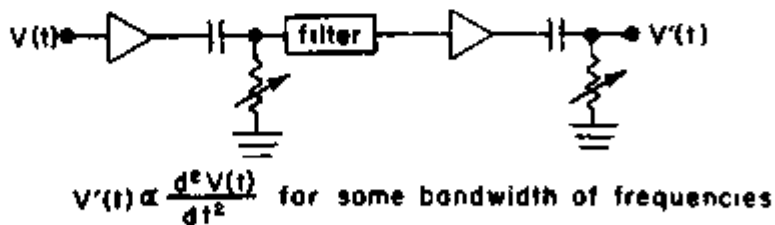
BASIC DIFFERENTIATOR**REALISTIC DIFFERENTIATOR***** TUNED DIFFERENTIATOR****** TUNED DOUBLE DIFFERENTIATOR**

Figure E-1.

Different analog methods of differentiating a time varying voltage with respect to time.

* See Ref. 13.

** See Ref. 14.

through the filter, and thus the derivative of a signal includes the full bandwidth of noise allowed by the filter. A more realistic version of a differentiator is shown in Figure E-1, where a low pass filter is included to act as a cutoff on the high frequency noise. A more complete idea of using a cutoff is to have a tuned differentiator that only looks at a narrow range of the Fourier components of a derivative. Finally, one can do a double differentiation with filtering, and then integrate the output. The first three filters shown were built and tested using analog circuits. The major limitations were that the signal to noise ratio was never very large (~ 20) and the maximum range of "frequencies" using conventional components was only three orders of magnitude (i.e., for $C \sim 10 \mu\text{fd}$, $R \sim 1 \text{ M}\Omega$, $\frac{dV}{dt} = 10^{-4} \rightarrow 10^{-1} \text{ v/sec}$; with higher ranges for lower values of C).

A second method of analog differentiation involves using feedback or modulation techniques to extract the derivative of a voltage signal. The feedback method, shown in Figure E-2, involves positive and negative feedback. This circuit was constructed, but went into oscillation (due to the positive feedback) whenever the limit of true differentiation was met ($\alpha = 1$). This meant it still was an approximation to the derivative of the signal. The second method shown in Figure E-2 involves using P.S.D. (Phase Sensitive Detection). This method actually works quite well if one knows the form of the derivative. In principal one adjusts the phase (ϕ) of the reference channel to let $\sin \phi = 0$.

But, because of the large size of $\omega_0 V(t)$ (especially at high frequencies) relative to $\frac{dV(t)}{dt}$, the adjustment of phase is crucial in order to remove any signal but the derivative. In practice, a difference of two tenths of a degree was enough to distort the derivative. The method of Figure E-3 is more complicated and is used primarily for tunneling work where the voltage wanted is that which is linear to dV/dt (or higher differentials). But, when the function that is wanted is dR/dt , then equations (E-3-5) through (E-3-8) show the difficulty of obtaining the function dR/dt without other derivatives complicating the problem. Nevertheless, this method was also tried without success. The final analog form tried was that of modulating the voltage, which varied linearly with $R(t)$. Figure E-4 shows the derivation of the result that by detecting at twice the frequency of the voltage modulating square wave, the detected output would be proportional to the derivative at high frequencies. But, at high frequencies the modulation is non-linear, and there is some attenuation in the voltage paths of the experiment, so that this method also included other forms besides the $\frac{dR}{dt}$ function. Thus, in general, the analog methods are hindered by noise. The noise problems can be reduced at the cost of distorting the derivatives' waveform. Because the derivative of the transition was not known, one would be unable to detect distortion in the true derivative. For this reason, digital methods were used.

The digital method of determining the derivative has the

Figure E-3

Higher Order Harmonic Detection Method*

First modulate resistance $R(t)$ with a current such that:

$$V(t) = V_0 + A \sin \alpha t \quad (E-3-1)$$

Therefore, the current is: $I = f(V)$ which we assume is analytic.

Then, expand $f(V)$ as a Taylor series:

$$f(V) = f(V_0) + f'(V_0)(V-V_0) + \dots \quad (E-3-2)$$

Then

$$I = I_0 + \frac{dI}{dV} (V-V_0) + \frac{1}{2} \frac{d^2I}{dV^2} (V-V_0)^2 + \dots \quad (E-3-3)$$

where the assumption $(V-V_0) = A \sin \alpha t \ll V_0$ is valid. Then,

grouping the harmonic terms:

$$\begin{aligned} I = & \left[I_0 + \frac{A^2}{4} \left(\frac{d^2I}{dV^2} \right)_{V_0} + \dots \right] \text{ D.C.} \\ & + \left[A \left(\frac{dI}{dV} \right)_{V_0} + \frac{A^3}{8} \left(\frac{d^3I}{dV^3} \right)_{V_0} + \dots \right] \sin \alpha t \text{ Fundamental} \\ & + \left[\frac{A^2}{4} \left(\frac{d^2I}{dV^2} \right)_{V_0} + \frac{A^4}{48} \left(\frac{d^4I}{dV^4} \right)_{V_0} + \dots \right] \cos 2\alpha t \text{ Second Harmonic} \\ & + \dots \text{ Higher Harmonics} \end{aligned} \quad (E-3-4)$$

Since $R(t)$ is driven by a constant current source

$$V(t) = I(t) R(t) \quad (E-3-5)$$

$$dV = dI R(t) + dR(t) I \quad (E-3-6)$$

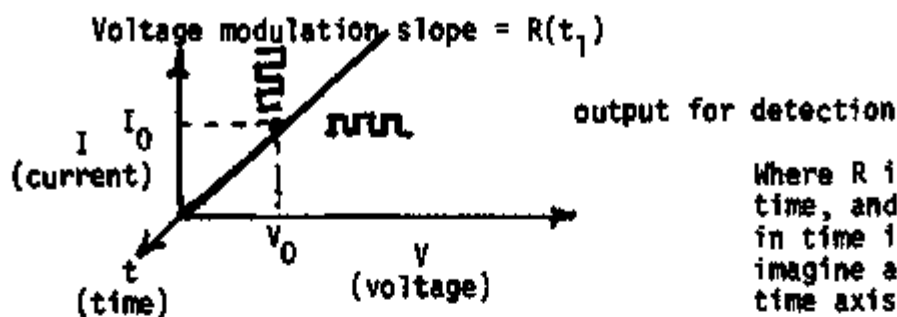
$$\frac{dV}{dI} = R(t) + \frac{dR(t)}{dI} I \quad (E-3-7)$$

$$\frac{d^2V}{dI^2} = 2 \frac{dR(t)}{dI} + \frac{d^2R(t)}{dI^2} I \quad (E-3-8)$$

Thus, the complications to evaluate dR/dt from the coefficients of higher order harmonics in the voltage signal.

Ref. 16.

Small Modulation Differentiation*



- 1) Assume $R(t)$ is ohmic $\Rightarrow V(t) = I(t) R(t)$.
- 2) Then the D.C. value of $V(t)$ is proportional to $R(t) \Rightarrow \bar{V}(t) = I_0 R(t) = V_0(t)$ for $I(t) = \text{constant}$ and either D.C. or Low Freq.
- 3) Then the time derivative of $V_0(t)$ is $\Rightarrow V_0'(t) = I_0 \frac{dR(t)}{dt}$.
- 4) Thus, by using a high frequency voltage modulation at $\omega (=1/\tau)$ of $V_0(t)$, such that $V_0(t) \Rightarrow v_0(t) \times \left[\text{SQ wave of period } \tau \right]$.

Then

$$v_0(t) = \frac{[V_0(t) - V_0(t + \frac{\tau}{2})]}{\tau/2} \sin 2\omega t + \dots$$

- 5) Thus the detected value of $V_0(t)$ of 2ω detection

$$\bar{V}_0(t)_{2\omega} = \frac{1}{\tau} \int_0^{\tau} \frac{[V_0(t) - V_0(t + \tau/2)]}{\tau/2} dt$$

and

$$\bar{V}_0(t)_{2\omega} = \frac{1}{\tau} \int_0^{\tau} I_0 \frac{[R(t) - R(t + \tau/2)]}{\tau/2} dt$$

Then in the

$$\lim_{\tau \rightarrow 0} \bar{V}_0(t)_{2\omega} = \frac{1}{\tau} \int_0^{\tau} I_0 \frac{dR(t)}{dt} dt = I_0 \frac{dR(t)}{dt} = \bar{V}_0'(t)$$

*Ref. 17.

Figure E-4

MULTIPLIER BOX

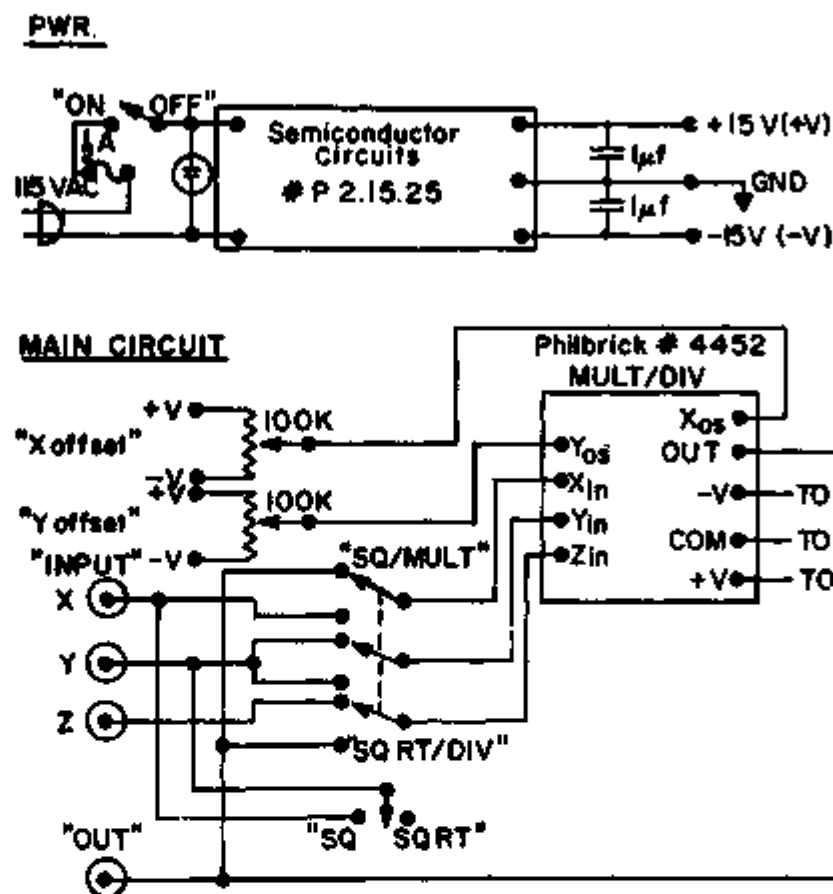


Figure E-5. Calibration and Use.

FOR: MULT ($|e_x|, |e_y| \leq 10; e_0 = \frac{-e_y e_x}{10}$) or SQ ($|e_x| \leq 10; e_0 = \frac{-(e_x)^2}{10}$)

SET: $x = 0, y = \pm 10 \text{ v @ } 100 \text{ Hz}$ SET: $y = 0, x = \pm 10 \text{ v @ } 100 \text{ Hz}$

ADJ: x_{0s} for null out THEN ADJ: y_{0s} for null out

FOR: DIV ($e_z \leq e_y, 0 < e_y \leq 10, |e_z| \leq 10; e_0 = -10 e_z / e_y$)

SET: $y = +10, z = 0$ SET: $z = +10, y = +10$

ADJ: x_{0s} for null out THEN ADJ: y_{0s} for -10 v out

FOR: SQRT ($-10 \leq e_z \leq -1; e_0 = \sqrt{-10 e_z}$)

SET: $z = -10 \text{ v}$ SET: $z = -1 \text{ v}$

ADJ: y_{0s} for +10 out THEN ADJ: x_{off} for +3.16 v out
then repeat

NOTE: In divider mode 1%, except for $z = 3 \rightarrow 6 \text{ v}$, then 5% error, for $y = 10 \text{ v}$.

same problem as that of the analog methods. The problem is that noise is introduced by the frequency of the sampling, where the more frequent the samples, the higher the amount of white noise that enters into the sampling.

The essential method is to determine from a grid of points sampled from a continuous function, a line tangent to any point (i.e., the slope) relative to nearby points. There are many schemes for determining this slope. The inherent problem of this method is that by working with sampled data, there is a noise error in that data associated with the frequency of sampling. Then the formed function, which involves the ratio of differences $\left(\frac{dR}{dT} = \frac{(R_i - R_{i+1})}{(T_i - T_{i+1})} \right)$ will be greatly modulated by this noise, especially for fluctuations in the denominator. Blackman and Tukey¹⁸ present a means of determining a power spectrum for a set of digital data. From this spectrum, one can design a digital filter that will filter out high frequency fluctuations in the sampled data, and yet retain the major part of the power spectrum. The second consideration was to adjust the sampling methods to be consistent with the time constants of the system (see Ref. 19, page 82). The sampling rate is such that the time constant of sampling is slightly less than the time constant of the lock-in, but at a frequency compatible with the cutoff frequency in the power spectrum, so that higher fluctuations (noise) are reduced from the data. The filter finally used on the data (for both R, T) was of the form:

$$f_i = (f_{i+1} + 2f_i + f_{i-1}) / 4 \quad (\text{E-4})$$

followed by,

$$f_i = (f_i + f_{i+1} + f_{i+2}) / 3 \quad (\text{E-5})$$

where f_i is the value of the function at the i^{th} point in time. Because the rate of temperature change when the transition is taken is constant ($\frac{dT}{dt} = r$) and since fluctuations in the denominator (dT of $\frac{dR}{dT}$) can increase dramatically the fluctuations of the function ($\frac{dR}{dT}$), the derivative was formed by:

$$\left. \frac{dR}{dT} \right|_i = \frac{R_{i+1} - R_{i-1}}{2\Delta T} \quad \text{where } \Delta T = rt_{\text{total}} / \# \text{ samples} \quad (\text{E-6})$$

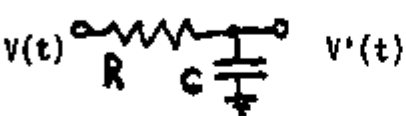
This was filtered by the above filter (eq. E-5) to give:

$$\left. \frac{dR}{dT} \right|_i = (R_{i+3} + R_{i+2} - R_i - R_{i-1}) / (3\Delta T) \quad (\text{E-7})$$

The resulting function was filtered again by both filters (eqs. E-4, E-5) This gave a satisfactorily varying slope that was consistent with all the time constants of the system, and thus did not arbitrarily alter the data. The proof of this was that successive applications of the filters did not alter the results, indicating that fluctuations were then below the cutoff frequencies of the filters.

It should be noted that the problem of noise in the analog

differentiation schemes is the exact problem of noise associated with the digital schemes. In fact, one can approach the analog problem using finite differential methods and draw an analogy between a specific analog circuit, and a specific form of a digital filter. A simple example would be of the form:

<u>Analog</u>	<u>Digital</u>
	$V(t) = V_n(\Delta t_n)$
$V'(t) \sim \frac{1}{RC} \int V(t) dt$ <p style="text-align: center;">where $RC = 3\Delta t$</p>	$V'_n(\Delta t_n) = \frac{V_n + V_{n-1} + V_{n-2}}{3}$

Because the data was in digital form to $2 \text{ pp}10^4$ and the many forms of later analysis could be made available to recorded digital data, the analog schemes for differentiating were discarded. Another possible form of differentiation is to fit the digital data to a polynomial, and then take the analytic differential of that polynomial and generate the derivative of the original data. This method was not used due to the inherent errors of differentiating a polynomial that sometimes has very fastly changing regions. It was believed that one should stay as close to the raw data as possible, and thus, that was why only slight smoothing was incorporated in calculating the derivative, $\frac{dR}{dt}$, of the resistive transition.

The derivative became a sizeable contribution to the error in

the experiment, especially with "kinky" resistive transitions. But, by using the digital differentiation method outlined above, this error could be reduced, without distorting the true functional form of the derivative of the resistive transition.

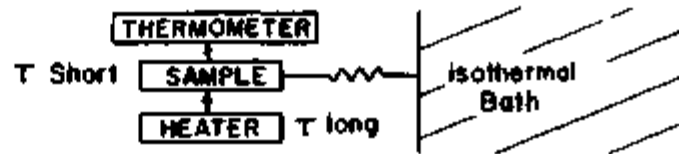
Appendix F. A.C. Calorimetry and the Heat Conduction Problem

The measurement of samples with small heat capacities has recently been expanded by the A.C. Calorimetry method. The method was first proposed by Sullivan and Seidel,²⁰ who used it to measure the superconducting transition of Indium in a magnetic field. The basic idea is that the sample, heater, and thermometer used in the heat capacity measurement have a characteristic time constant that is considerably smaller than the time constant of coupling this system to an isothermal bath. Then, one continuously applies heat pulses of a length long enough to allow the calorimeter to be in equilibrium, and yet short enough so the isolation link to the isothermal bath does not have time to conduct the heat pulse away. Figure F-1 gives a brief description of this idea. A further requirement on the isolation link, is that it has to couple the sample well enough to the bath so the D.C. rise in temperature of the sample due to the integration of the A.C. heat pulses is not too large. In this experiment, the sample's D.C. temperature is increased in time anyway, so that this requirement is not as important.

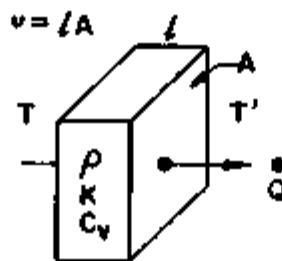
In analyzing the thermal relations of this experiment, it is quite helpful at times to formulate the problem in such a way as to lend a direct analogy with an equivalent electrical circuit problem. In Figure F-1, a thermal problem involving a slab of material with density ρ , thermal conductivity K , heat capacity

A.C. Calorimeter

Heat is Pulsed at a Rate ω , Such That
 $\omega T_{\text{Short}} \ll 1$
 $\omega T_{\text{Long}} \gg 1$

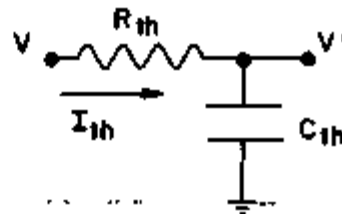


Thermal Problem:



Temp. Referenced To Isothermal Bath

Electrical Analog



Note Direction of Filter With Respect to Heat Flow.

Voltage Referenced To Electrical Gnd.

Superconducting Calorimeter

Electrical Equivalent

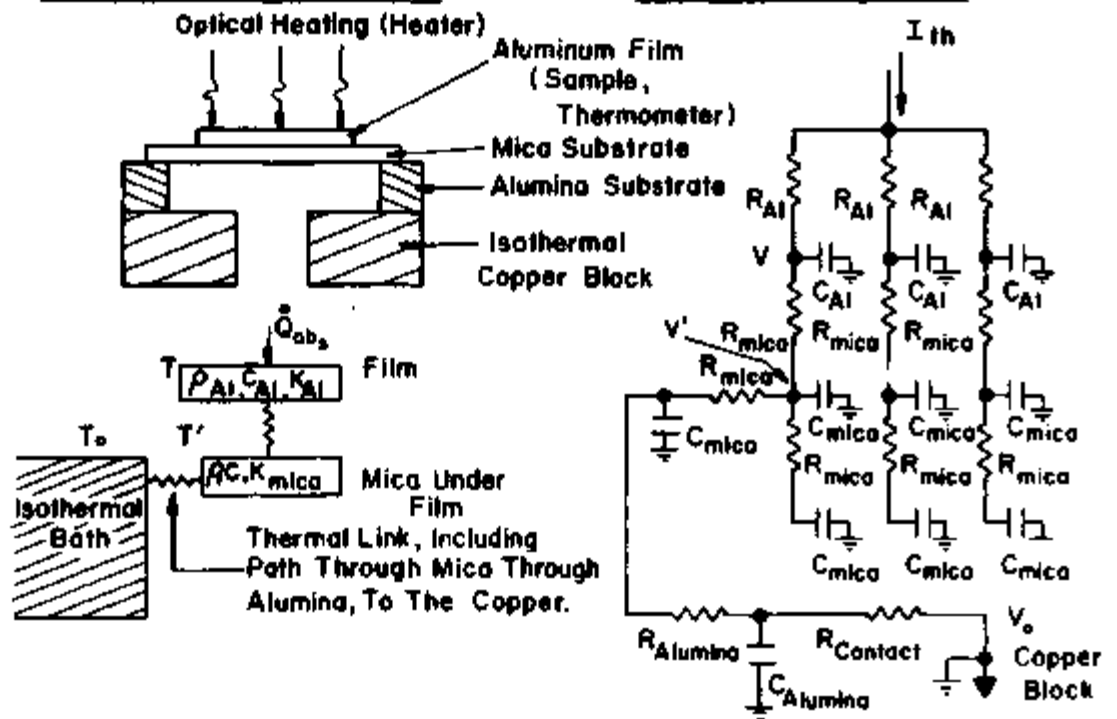


Figure F-1.

The A.C. Calorimetry method is shown with an equivalent electrical analog. For further details see text and Appendix C.

per mass C_v , and length ℓ , and area A is shown (all in C.G.S. units). A power of \dot{Q}_{abs} is conducted through the slab in the direction shown and is terminated off at some isothermal bath, such that all temperatures are really temperature differences relative to the bath ($T_0=0$). The electrical analog shown in Figure F-1 has an equivalent circuit that involves two temperatures (V, V'), a heat flow (I_{th}), a heat capacity (C_{th}), and a thermal resistance (R_{th}). In Table F-1, the analogy is shown in more exact detail, where an internal heat source (in the slab) is included. The electrical equivalent to this heat source is to have an internal current source (a battery in series with a large resistance, and in parallel with R). The three equations in a differential time dependent thermal problem are shown first in Table F-1. F is the power flow/area, and " a " is the internal heat source which is equal to an energy density/time. The electrical equations are written in such a way that they have a one to one correspondance to the familiar thermal problem. Integration by parts over a very short path integral is used in deriving the third equation (i.e., $\frac{1}{V} \int_x^{x+\Delta x} \frac{\alpha V}{\alpha x} \cdot dA \approx \frac{\alpha^2 V}{\alpha x^2}$ for Δx small). I_{int} is the internal current source of the resistor R . Once this analogy has been established, a finite difference approach (i.e., $\alpha T \rightarrow \Delta T$, $\alpha V \rightarrow \Delta V$, $\alpha x \rightarrow \ell$) can be used to restate the problem. The second set of equations restate the thermal problem in an electrical form, with appropriate thermal capacitances, resistances, and time constants. The electrical current flow is referred to positive current flow in order to obtain the familiar potential

Table F-1
Electrical Analogy to Heat Flow

<u>Quantity</u>	<u>Heat</u>	<u>Electric</u>
I. Electrical eqs. in heat form:		
1) resistance where $F = \dot{Q}/A$	$F = -K \frac{\partial T}{\partial x}$	$J = -\sigma \frac{\partial V}{\partial x}$ where $\frac{dq}{dt} = \int J \cdot dA$
2) capacitance	$\frac{\partial F}{\partial x} + \rho c \frac{\partial T}{\partial t} = a$	$\frac{dq}{dt} + C \frac{\partial V}{\partial t} = I_{int}$
3) dynamics (eq. 1+2 combined)	$\frac{\partial^2 T}{\partial x^2} - \frac{\rho c}{K} \frac{\partial T}{\partial t} = -\frac{a}{K}$	$\frac{\partial^2 V}{\partial x^2} - \frac{C}{\sigma v} \frac{\partial V}{\partial t} = \frac{-I_{int}}{\sigma v}$
II. Heat eqs. in electrical form:		
1) thermal resistance	$\Delta T = -\frac{dQ}{dt} R_{th} = -I_{th} R_{th}$	$V = -\frac{dq}{dt} R = IR$
	$R_{th} = \ell / KA, I_{th} = \dot{Q}$	$R = \frac{dx}{\sigma A}, I = -\frac{dq}{dt}$
	$\Delta T = (T - T') = -T_R, \ell = dx$	$\Delta V = (V - V') = V_R, dx = \ell$
2) thermal capacitance	$I_{th} + C_{th} \frac{dT'}{dt} = I_Q$	$\frac{dq}{dt} + C \frac{dV'}{dt} = I_{int}$
	$C_{th} = \rho c v, I_Q = av$	
3) dynamics	$T_R = I_Q R_{th} + \tau_{th} \frac{d(T_R + T)}{dt}$	$V_R = -I_{int} R + \tau \frac{d(V_R - V)}{dt}$
	$\tau_{th} = \ell^2 / \kappa = C_{th} R_{th}, \kappa = \frac{K}{\rho c}, \text{ and } T \text{ is always referenced to same } T_0 \text{ (isothermal bath)}$	
	$\tau = RC, \text{ and } V \text{ is always referenced to same } V_0 \text{ (voltage grnd.)}$	
and the two systems are connected by power exchange		
4) power exchange	$P_{th} = \frac{T_R}{R_{th}} \text{ (joules)}$	$\rightarrow P = \frac{V_R^2}{R} \text{ (joules)}$

differences. Thus, although equations II-1 differ in appearance (the minus sign), they are the same physical concept. The equations II-3, showing the dynamics, are also equivalent. This is because T and V are constants in time, and one refers to positive potentials for negative electrons flowing backwards (the sign in front of I_{int}). These equations can be converted back to the differential form of equations I-3 by using the finite difference substitutions. Note that there is no need for thermal inductances. Equation II-4 of Table F-1 relates the power in the two systems. As will be shown in a later appendix, one can interface an electrical circuit to a thermal problem, by formulating the thermal problem in electrical form and equating powers in each system through some thermal constant resistance (heater-thermometer barrier) using equation II-4. Thus, the electrical analogy shown in Figure F-1 is complete for the thermal problem, in the limit of small thicknesses and for the low pass filter to be oriented in the correct direction relative to the heat flow. The differences in the signs of the analogy of Table F-1 is related to the potential drop for positive current in the electrical problem, and an energy loss for the heat flow in the thermal problem.

Originally, an attempt was made to solve the problem by normal analytical methods using the thermal equations of Table F-1, part I. The problem was formulated as that of a 1000 \AA aluminum film, heated by optical pulses (6328 \AA), in contact with a $50,000 \text{ \AA}$ alumina substrate in contact with an isothermal copper block.

Since the attenuation constant of the light in the aluminum is about $6 \times 10^5 \text{ cm}^{-1}$,²¹ almost no light is transmitted by the film, and since 92% is reflected, about 8% of the incident radiation is absorbed by the film. This compares with transmission measurements of the films which show $\sim .1\%$ transmission. This reduces the problem to that of a source driving the film throughout, and since the film's thermal time constant ($\tau_{th} = \frac{L^2}{\kappa} \sim 10^{-13} \text{ sec.}$) is much smaller than the driving frequencies, we can assume it to be isothermal.

The problem in the analytic solution is in matching the boundary conditions at both the vacuum interface (on the exposed aluminum side) and on the aluminum-alumina interface. An attempt was made to solve the problem by the method of finite differences, where essentially the differential equations of Table F-1 are transferred to finite differences amounts. The one spatial dimension is divided into small increments $\Delta x = h$, and time is divided into increments $\Delta t = rh^2$, which are normalized by the medium's thermal diffusivity constant ($\Delta t = \Delta t_{real} \kappa_{medium}$) such that:

$$\frac{\partial^2 T}{\partial x^2} = \frac{\partial T}{\partial t} \rightarrow T_{j,k} = T(j\Delta x, k\Delta t) \text{ being the temperature at the } j^{\text{th}}, k^{\text{th}} \text{ increments.}$$

(F-1)

Equation (F-1) is then:

$$T_{j,k+1} - r\theta(T_{j-1,k+1} - 2T_{j,k+1} + T_{j+1,k+1}) = T_{j,k} + r(1-\theta)$$

$$\times (T_{j-1,k} - 2T_{j,k} + T_{j+1,k}) \text{ where } \theta \text{ is an arbitrary parameter,}$$

$$\text{and } r = \Delta t / (\Delta x)^2 \quad (F-2)$$

As pointed out by Crandall,²² for different values of θ , we have different forms of the finite differences equations. The two most well known are the Implicit ($\theta = 1$) and the Explicit ($\theta = 0$) and possibly the Crank and Nicolson form ($\theta = 1/2$). The problem with the explicit form is that $r (= \Delta t / (\Delta x)^2)$ has to be less than 1 ($\sim 1/2$), or otherwise unstable, oscillating solutions result. This constraint is equivalent to the heat flow reversing direction between difference evaluations. Crandall²² varied r and θ in an arbitrary way to map out the solutions. One can get stable solutions as in the methods mentioned before, but the accuracies are not to orders higher than $\theta(h^4)$. By choosing $r = 0.2236$, $\theta = 0.1273$, he found stable solutions to an accuracy of $\theta(h^6)$. The boundary condition imposed on the problem is that $\Delta t_1 = \Delta t_2$, for the two media (aluminum, alumina). Since $r < 1$ implies $\frac{\Delta t_{\text{real}}}{(\Delta x)^2} \leq 1$, this sets a constraint on the maximum size of time increment. And $\Delta t_1 = \Delta t_2$ sets a size on the grid ratios of the two mediums (i.e. $\Delta x_1 = \sqrt{\frac{\kappa_1}{\kappa_2}} \Delta x_2$). Essentially one normalizes the grids so the problem looks like one medium. But since $\sqrt{\frac{\kappa_{\text{Alumina}}}{\kappa_{\text{Aluminum}}}} \approx 10^{-2}$, we need 100, $\Delta x_{\text{aluminum}}$ increments to have

just one $\Delta x_{\text{alumina}}$. And, since only two $\Delta x_{\text{alumina}}$ means $\Delta x_{\text{aluminum}} = \frac{1000\text{\AA}}{2 \times 10^2} = 5 \times 10^{-8} \text{ cm}$, our stability requirement means that our maximum time increment is:

$$\Delta t = \frac{(\Delta x)_{\text{aluminum}}^2}{k_{\text{aluminum}}} = \frac{(5 \times 10^{-8})^2}{10^4} \sim 10^{-20} \text{ sec.}$$

One can see that a computer solution is going to be quite costly to monitor even just one second of time in the problem. The basic nature of the problem, that of a very thin, fast thermal material, in contact with a very thick, slow thermal material, means that one has to have many increments in space to normalize the sizes, and many increments in time to normalize the thermal responses.

One can take the problem directly over to an electrical analog problem and try to do an analog solution with an equivalent electric circuit. But, the same constraints are there, and one is talking about hundreds of R, C networks.

The problem was attempted on a 6600 in varying degrees of approximations, but was not concluded due to the large computer times involved and the simplification arguments presented later. Most graphical solutions²³ are not useful since they are not in the ranges needed.

A better way to analyze the problem is to assume the aluminum is an isothermal slab, following the oscillations of the optical heating. This is justified since the light is absorbed throughout the film, and the film has a time constant very much smaller than the period of heating ($10^{-3} + 10^{-4}$ sec). Thus, if one is heating

a self-supported film, without any substrate, the heat capacity would be:

$$C_{\text{film}} = \frac{\Delta Q}{\Delta T} = \frac{\dot{Q}_{\text{abs.}} \tau_{\text{osc}}}{\Delta T_{\text{measured}}} \quad (\text{F-3})$$

If the film was attached to a substrate, like the problem of an aluminum film on an alumina substrate, the heat capacity would be different. Now an amount of the substrate would follow the film's temperature oscillations, and thus reduce the ΔT measured. This amount is just the area (A) of the substrate under the film times the thermal length, where $\lambda_{\text{thermal}} = \sqrt{\tau_{\text{osc}} \kappa_{\text{sub}}}$. Then the heat capacity of equation (F-3) becomes:

$$C_{\text{film}} = \frac{\dot{Q}_{\text{abs.}} \tau_{\text{osc}}}{\Delta T_{\text{measured}}} - C_{\text{sub}} A \sqrt{\tau_{\text{osc}} \kappa_{\text{sub}}} - C_{\text{other}} A \sqrt{\tau_{\text{osc}} \kappa_{\text{other}}} \quad (\text{F-4})$$

where the other contribution could be from an adsorbed He film. Equation (F-4) is just a 1st order approximation to the problem. A more complete description would be related to the temperature pulses measured (ΔT) for the heating pulses applied. By constructing a number of low pass filters in series, one can approximate the problem. Thus, by going to higher frequencies in heating, one has a shorter time constant associated with the temperature oscillations, and equation (F-4) becomes (F-3). This is the same as saying the low pass filters become larger impedances to the high frequency heat pulses, and thus do not attenuate the temperature oscillations (ΔT). Figure F-2 shows such behavior for an analog solution to a

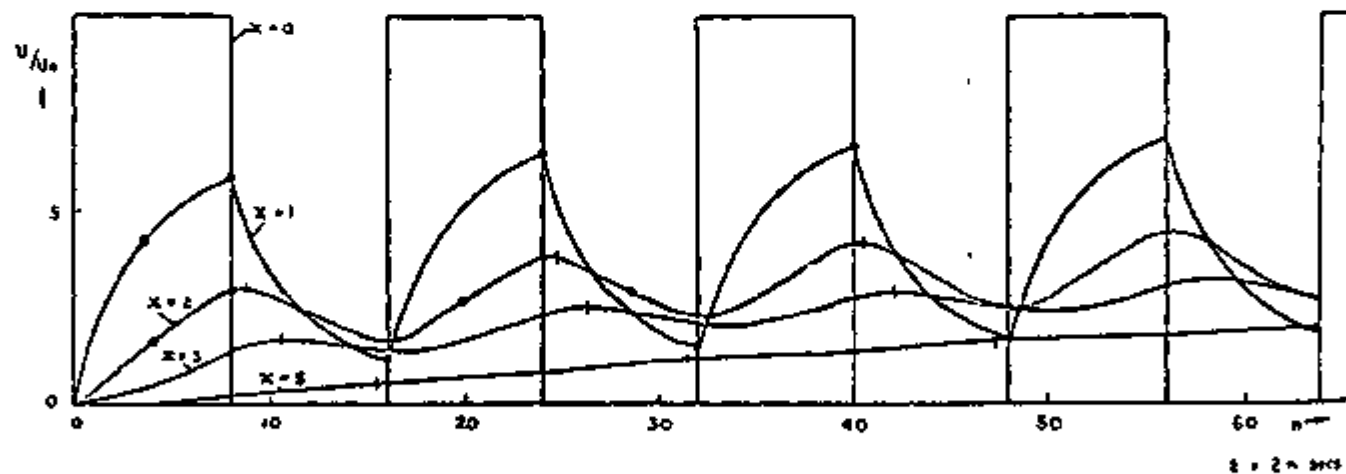


FIG. 13. TEMPERATURE DISTRIBUTION AS FUNCTION OF TIME AT SEVERAL POSITIONS x IN SEMI-INFINITE LINEAR HEAT-INSULATED STEEL BAR HEATED PERIODICALLY AT $x = 0$
 $(D = 0.125 \text{ cm}^2/\text{sec}, H = 2 \text{ sec})$

Figure F-2.

The temperature profile for an analog solution of the heating of a steel bar by a step temperature pulse at one end ($x=0$) monitored at successive points down the bar ($x=1,2,3,5$) as a function of time. Note that after a short time a steady state situation results, with only the first few monitor points following the temperature pulses. (from G. Liebmann, Trans. of ASME, 78-1, 655, (1956)).

heated steel rod. Figure F-7 shows the transformation of the discrete thermal problem in the experiment to the equivalent, 1st order electrical circuit. This circuit is only a guide, and is in no way the exact equivalent, since the constraints on a finite difference grid have not been applied. To determine the thermal time constants of the materials, one needs ρ , K , C . It should be noted that even if C or K for the film were diverging quantities, they still could never change the films' time constant (10^{-13} sec) enough to be on the order of the heating (10^{-4} sec). Mica was chosen as a substrate because of its layered nature. Operating at 1.5K, might produce a rather large Kapitza boundary resistance between the layers and thus give it a very small effective transverse thermal conductivity (K). Films evaporated on the mica substrates did not at first have an A.C. heating signal. At first this problem was thought to be related to the film being too closely coupled to the substrate, and thus it could not heat up at all. Later, it turned out to be a problem in the electronics. But, because of the initial failures, self-supported films were made and tested. These films could be optically heated. Since by this time the electronics problem was solved, films on mica and glass were also tried. They both give optical heating, (up to 20 KHz) although the signals were not as large for the films on glass. A rough comparison is given below:

Run #	Substrate	ΔT	\dot{Q} (approx.)	τ	C
30I	mica	$7 \times 10^{-6} K$	$2 \times 10^{-12} W$	$10^{-3} sec$	$2.85 \times 10^{-10} J/K$
32	glass	$4 \times 10^{-7} K$	$10^{-12} W$	$10^{-3} sec$	$2.5 \times 10^{-9} J/K$
26D	self-support.	$1 \times 10^{-5} K$	$2 \times 10^{-11} W$	$10^{-3} sec$	$1 \times 10^{-9} J/K$

The film on glass is measuring a larger heat capacity for roughly the same film as the film on mica. This would indicate that the film on the glass substrate was closer coupled to the substrate than the film on mica. The self-supported film had a different light source, and so it quite possibly is an inaccurate comparison to the other two films. As an independent check on the coupling of films on mica, a measurement of the transverse diffusivity of mica was made. A manganin heater was evaporated on the back side of a film (100 Ω and same area as film) on a piece of mica. In this way, heat pulses could be created on one side of the $\sim .2$ mil. thick piece of mica, and detected on the other side by the superconducting film. The geometry of the films was verified by measuring the capacitance of the two films with mica as the dielectric. The heater was driven with a voltage biased heating power at a frequency of ω , and the film was monitored for heating at both 2ω , and ω (indicating just electrical coupling). From frequencies as low as 2Hz up to 10KHz, no A.C. heating pulse could be detected, that was not just an electrical coupling of the voltage at ω detected at 2ω . By knowing the power of the heating pulses and the sensitivity of the detector, a lower limit on the

heat capacity of the mica could be determined. Thus the heat capacity of the mica between the film and the heater (area $\sim 1.2\text{cm}^2$, thickness $\sim 5 \times 10^{-4}\text{cm}$) could be estimated as being greater than 10^{-4}J/K (1KHz measurements) $\rightarrow 10^{-3}\text{J/K}$ (2Hz measurements), which does not compare to a calculated value of $C \sim 8 \times 10^{-8}\text{J/K}$ using the data of Table F-2. But, this is assuming a steady state, and if the transverse thermal conductivity was very small, then the time constant of the heat pulses was too short for the equilibrium time between the heater and the film. A diffusivity measurement was also made of the mica. The heater was driven with a step pulse, and the temperature of the film was monitored. For large pulses of the heater, the film would rise with an exponential time constant of 1 sec to a higher level. It took $2.5\mu\text{W}$ to raise the film $.7\text{mk}$ over a time of 1 sec. For the thickness of the mica and a thermal time constant of 1 sec, this gives a diffusivity of $2.5 \times 10^{-7}\text{cm}^2/\text{sec}$ for a power of $2.5\mu\text{W}$. Since the heat capacity and the density are somewhat better known (or estimated, see Table F-2) for mica, this would indicate a thermal conductivity of $K \sim 2.85 \times 10^{-11}\text{W/mk}$ at 2K. This would also indicate why A.C. heating at 2Hz did not produce thermal steady state conditions. It should be mentioned, that if the data for the pulse testing is used to calculate an equivalent heat capacity to absorb the heat within the time constant measured, one finds an equivalent heat capacity of $C_{\text{equiv}} \sim 3 \times 10^{-3}\text{J/K}$ (where $C_{\text{equiv}} = \frac{Q_{\tau}}{\Delta T}$), which agrees with the levels set by the A.C. heating measurements. Thus from these pulse and A.C. heating

Table F-2. Thermal Properties at Low Temperatures of Materials Used.

Material	Thermal Conductance (K)	Density (ρ)	Heat Capacity (C)	Diffusivity (κ) Calculated $\kappa = K/c$	($\tau = L^2/\kappa$) Comments
Mica	If like epoxy at 2K $K \sim 1.4 \times 10^{-4}$ W/cmK. Similar to muscovite @ 100 K, $K \sim .72 \times 10^{-2}$ W/cmK (ref. 28). Then if $K \propto T^3$ @ 2K $K \sim 5 \times 10^{-6}$ W/cm K.	$\rho \sim 2.85$ gm/cm ³ @ 2K since $\rho = (2.6-3.2)$ gm/cm ³ @ 300 K (ref. 25, pg. F-1) and solids have very little density change to 4K (<1%)	If like epoxy at 2K $C \sim 1.44 \times 10^{-4}$ J/gm K if like H_2SiO_3 at 100K $C \sim .5$ J/gm ³ K (ref. 29). Then if $C \propto T^3$ at 2K $C \sim 4 \times 10^{-5}$ J/gm K. (see ref. 55)	$\kappa \sim 4.4 \times 10^{-4}$ cm ² /sec for $K \sim 5 \times 10^{-6}$ W/cmK $\kappa \sim 6.3 \times 10^{-3}$ cm ² /sec for $K \sim 7.2 \times 10^{-3}$ W/cmK	Very little low temp. data on mica. The number for κ was in- dependently measured. See text.
Glass (pyrex)	@1K $K \sim 1.2 \times 10^{-4}$ W/cmK (ref. 24, pg. 30)	@2K $\rho \sim 2.6$ gm/cm ³ since @ 300K $\rho \sim (2.4-2.8)$ gm/cm ³ (ref. 25, pg. F-1)	@2K $C \sim 2.4 \times 10^{-4}$ J/gmK (ref. 25, pg. 139)	$\kappa \sim 1.9$ cm ² /sec @ 2K	
Aluminum (dirty)	@ 2K $K \sim 4.8 \times 10^{-1}$ W/cmK (ref. 26, pg. 876)	@2K $\rho \sim 2.7$ gm/cm ³ since same at 300K (ref. 24, pg. 274)	@2K $C \sim 1.5 \times 10^{-4}$ J/gmK (ref. 27) where α/β $= 20.1$, $T_c = 2.06$ for this data, where the "dirt" was about 35% Al_2O_3 .	$\kappa \sim 1.2 \times 10^3$ cm ² /sec @2K	The transverse time constant of a 1000 Å film is then 10^{-13} sec.
He ⁴ (monolayer) on copper	Normal fluid $K \sim 3 \times 10^{-4}$ W/cmK @ 4K, if including Kapitza boundary resis- tance $K_{eff} \propto T^{1/2}$ for $1K < T < T_\lambda$, if like 1000 times copper at room temp. $K \sim 3 \times 10^{-4}$ W/cmK in superfluid (ref. 31, page 10).	$\rho \sim .146$ gm/cm ³ @ 0K (ref. 31, pg. 40) for liquid	$C \sim .4$ J/gmK @ 2K (ref. 30)	$\kappa \sim 5 \times 10^{-3}$ cm ² /sec to 5×10^4 cm ² /sec depending on it being a super or normal fluid	The monolayer may not be a superfluid and also the Kapitza boundary re- sistance will also reduce K.
Gas	$K \sim 4 \times 10^{-5}$ W/cmK @2K (ref. 31, pg. 98)	$\rho \sim 179 \times 10^{-3}$ gm/cm ³ (ref. 24, pg. 8) at STP	$C \sim 5$ J/gmK at STP ρC varies linearly with pressure	$\kappa \sim 4$ cm ² /sec ($\frac{760}{P}$) $\sim 5 \times 10^4$ for $P \sim 1$ mm	He gas at low pressures has a very small diffusivity

measurements, it can be assumed that at 2Hz, a significantly smaller thermal penetration length than 5×10^{-4} cm exists, and that the thermal diffusivity for the mica at 2K is $\kappa \sim 2.5 \times 10^{-7}$ cm²/sec.

To completely understand the thermal nature of the experiment, a final measurement of the D.C. thermal conductivity of mica was needed. A film was evaporated onto a mica substrate (5.08×10^{-3} cm thick) and the mica was well bonded (Eastman 910 glue) to an isothermal copper block. The film was biased with an A.C. voltage to determine its resistance, and a D.C. current to create a power flow through the mica and thus cause a temperature gradient. Measurements were made for different power levels at two points in the film's transition. He gas was admitted and the film's resistance was calibrated to the temperature of the isothermal block. An attempt was made to determine the power of the laser light absorbed by the film by measuring the conductivity with it on and off. This measurement put an upper level on the power of $\sim 10^{-12}$ W (this is discussed in another section). The results of the transverse thermal conductivity were quite revealing. They showed an exponential behavior of the conductivity vs the power for both sets of measurements for powers greater than 2×10^{-11} W. It had the form shown below.

$$K_{\text{mica}} \sim 8 \times 10^{-14} \text{ watts/cm} \frac{e^{6.6 \times 10^2 \Delta T}}{\Delta T} \quad (\text{F-5})$$

If no power is dissipated in the film, this would give a ΔT of zero relative to the copper block and give a meaningless thermal

conductivity. Since there is always power dissipated in the film due to the measurements taken, this would limit the ΔT to be greater than 10^{-3} K. This would give a thermal conductivity of $K \sim 1.5 \times 10^{-10}$ W/cmK. One might expect an exponential form for small temperature differences because of the layered nature of mica. One might associate a threshold with each layer (which can be quite thin, i.e., a few atomic layers) and each successive layer involves the reduced power in a new threshold, and thus a total conductivity is like a series of resistors going R, R^2, R^3 , etc. The thermal conductivity measured in this way agrees reasonably well with the thermal conductivity calculated from the diffusivity. Thus, it is quite reasonable to expect a film on mica to be quite decoupled from the substrate.

Now that the values for the materials of interest are reasonably well known, one can calculate the measured heat capacity at any frequency using Table F-2. It will be:

$$C_{\text{total}} = A \sqrt{\tau} \left(\sum_i \rho_i C_i \sqrt{\kappa_i} \right) \quad (\text{F-6})$$

where A is the area and $1/\tau$ the heating frequency. For the materials in the calorimeter (neglecting He, since it is only admitted after the measurements), this becomes:

$$C_{\text{total}} = A \sqrt{\tau} \left(\rho_{\text{Al}} C_{\text{Al}} \sqrt{\kappa_{\text{Al}}} + \rho_{\text{mica}} C_{\text{mica}} \sqrt{\kappa_{\text{mica}}} \right) \quad (\text{F-7})$$

Using the numbers for these materials:

$$C_{\text{total}} = A \sqrt{\tau} (1.4 \times 10^{-2} + 3.7 \times 10^{-7}) \text{ J/Kcm}^2 \text{sec}^{1/2} \quad (\text{F-8})$$

This implies that if the aluminum was always thick enough, the total heat capacity at any frequency would always be the film. But, for a thin slab of aluminum, one has to compare the sizes of the measured heat capacities themselves. For $1/\tau = 1 \text{ KHz}$ they are:

$$C_{\text{film}} = 4.8 \times 10^{-9} \text{ J/K} \quad (\text{F-9})$$

$$C_{\text{mica}} = 2.0 \times 10^{-9} \text{ J/K for } \ell_{\text{thermal}} = 1.5 \times 10^{-5} \text{ cm} = \sqrt{\kappa\tau} \quad (\text{F-10})$$

Early measurements were actually made with a slight background of He gas ($P \ll 1 \text{ mm}$). This background only slightly affected the A.C. signal strength, while greatly affecting the D.C. thermal conduction. This would imply that the diffusivity of the He was very small. In view of the K_{eff} mentioned in Table F-2, this could quite possibly be the case.

The fact that an A.C. heating pulse is measured for films on mica, and is considerably larger than for films on glass, implies that the aluminum films are quite decoupled from their mica substrate. At most (for $1/\tau = 1 \text{ KHz}$) the mica is only $1/2$ of the total heat capacity measured. If one considers the dramatic possibilities

that the Kapitza boundary resistance might have in influencing the measurements, it is quite possible that an even smaller percentage of the total heat capacity is the mica. Also, the heat conduction paths in general are those shown in the equivalent circuit in Figure F-1. This means that less heat is conducted down into the mica (because it is not terminated) and more is conducted out to the edges. This implies that the films are actually decoupled at high frequencies from the substrate, and appear as if they were self-supported.

The conclusions presented above make it possible to try to use a superconducting film as a bolometer, if the light is chopped at a high enough frequency. Martin and Bloor³² made a bolometer that is very similar to the apparatus used in this experiment. Their films were on a mica substrate, which was supported by nylon threads which had lead leads evaporated on them. The incoming light was chopped at 10Hz, and the film's resistance was monitored with an A.C. Bridge. It is interesting to note that their films (Sn) had broadened transitions, and their measurements of the thermal conductance (including the lead and nylon leads) also had an exponential form. In general, superconducting bolometers are only useful for high frequencies, where a bolometer with a fast response is needed. Rose and Bertin³³ have measured 20 nsec. pulses with a superconducting bolometer. Their model for the equivalent circuit of a bolometer however is in disagreement with that mentioned in the main body of the thesis. They describe two

modes of a bolometer operation. The first is just a thermal mode, and the second involves a sort of pair breaking scheme taking place in the superconductor. Comparing the superconducting bolometers to other bolometers, they find a decreasing linear relationship between the log of the sensitivity and the log of the time response of the bolometers. Superconducting bolometers do not have the ultimate sensitivity of other bolometers (doped Ge chips), but do have a faster response time. This increased response time may not be needed in I.R. Astronomy, but areas like Laser Physics might find a use for fast bolometers.

The question of a possible pair breaking mechanism taking place in the films used in this experiment is a serious one. If this was the case, the optical heating signal would not be a measurement of the heat capacity, but rather a measurement of the disturbance of the pair field in the superconductor. Testardi³⁴ and Parker and Williams³⁵ have shown disturbance of the pair field by optical radiation where $h\nu > \Delta_{\text{gap}}$. Owen and Scalapino³⁶ explain this by a disturbance in the pair field. Since the measurements in this experiment are always for $R > 0$, the superconducting system is essentially in a full quasi-particle state, with very few paired electrons. Then, there is no pair field to disturb with the laser radiation, and one has just a normal metal model for laser radiation absorption. This is confirmed by the fact that the resistive transition of the films is undisturbed in form with the laser on or off. Thus, pair breaking mechanisms

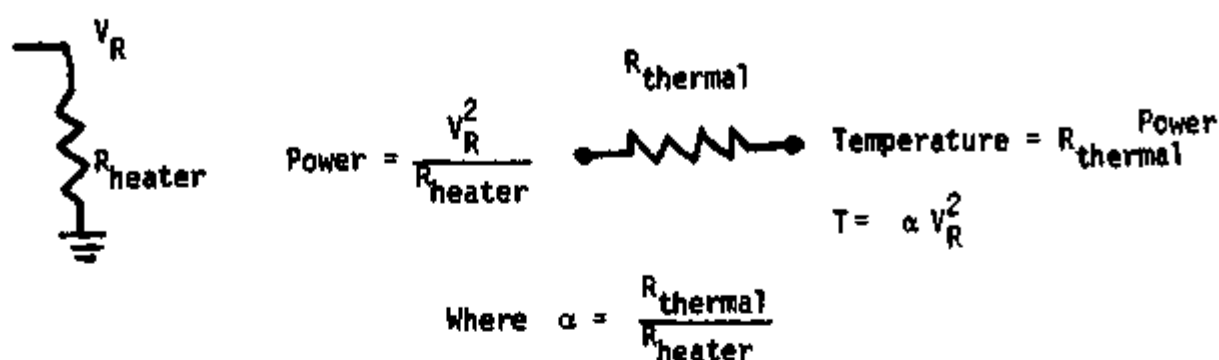
are not responsible for the A.C. heating measurements.

In conclusion, the A.C. calorimetry method outlined in this section is being used to measure the heat capacity of the films. Because of the choice of mica substrates, and the frequencies of heating used, the films behave as if they were self-supported, and the heat capacity measured can be predominately related to the film. This approach also has applications for use as fast bolometers. The thermal heating processes do not involve pair breaking mechanisms, so that one is truly measuring the heat capacity of the films. In this way one can measure the extremely small heat capacities ($\sim 10^{-9}$ J/K) quite well.

Appendix G. Analog Servo System.

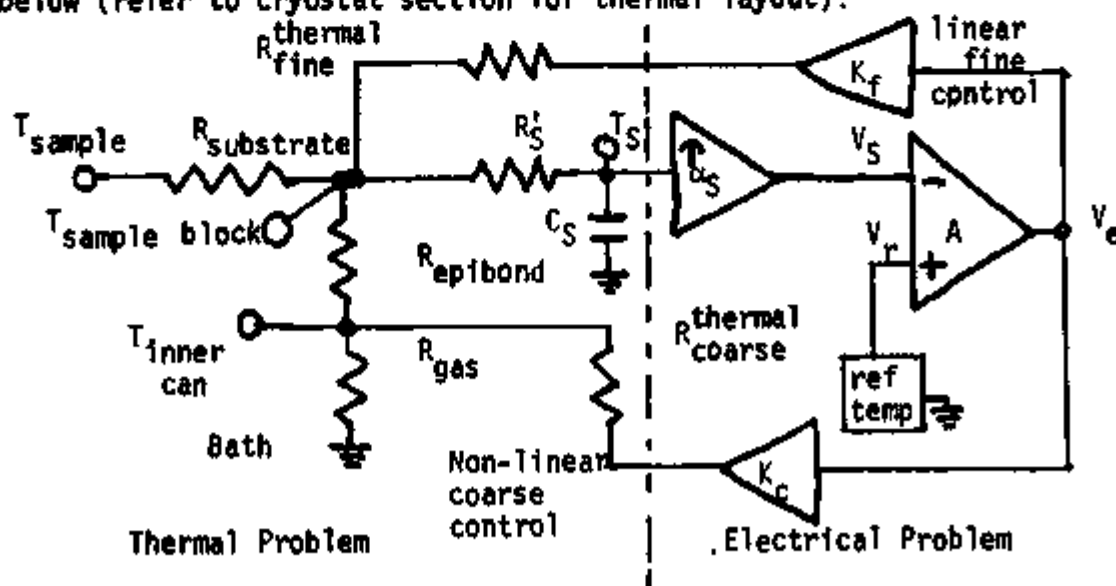
The experiment involved looking for effects over a temperature interval that corresponded to the critical region of the film. The width of this region was hard to calculate, but it was on the order of 10^{-6} K. This meant that the temperature of the sample would have to be maintained to that degree of accuracy. There are two possible ways of achieving high thermal stability. The first is to have the sample closely tied to a very large heat capacity like a bath of He^4 , thus causing an integrating effect on any small thermal fluctuations. This method was not used because of space available. A second method is to use a heater-sensor feedback loop to electronically regulate the temperature of the sample block. Because of the wide success of this method in general, it was chosen as the means for reaching high thermal stability. But, because of the high accuracy needed, it was decided to handle the servo problem in a much more sophisticated manner than the usual crude means of driving a heater with just the off null of an A.C. bridge reading the temperature sensor.

The first step was to transform the thermal problem of the relationship between the cryostat, the heaters, and the temperature sensors into an electrical analog along the lines mentioned in an earlier appendix. This was interfaced to the electrical feedback circuit by the relationship between power in the two systems, i.e.:



Because of the cryostat's construction with a rather large inner can isolating the sample block from the He^4 bath, it was decided to sense the temperature errors on the sample block and drive a local heater on the block in a linear fashion (fine heater), and drive the inner can heater (coarse heater) in a non-linear fashion from the same error, but only if the local heater could not handle the error correction.

A first approximation to the overall feedback circuit (including both the thermal and the electrical systems) is shown below (refer to cryostat section for thermal layout):



The error voltage (V_s) corresponds to a temperature error (T_s) as sensed by the sensor in the sample block. They are related by the gain of the lock-in of the A.C. bridge, and the change in voltage (resistance) of the sensor for a unit change in temperature. This is lumped into the parameter α_s . This error voltage is added to the reference temperature at which the system is desired to be at and then drives both the linear heater control and the non-linear heater control. These two paths of power flow into the thermal problem through their appropriate thermal impedances and complete the feedback loop. The restrictions on this feedback circuit are:

- 1) Stable operation--loop gain ≥ 20 db/decade
(12 db/octave)
- $$\tau_{\text{electrical}} = \tau_{\text{system}} \text{ where } 1_{\text{sec}} \geq \tau \geq 10^{-2} \text{ sec}$$
- 2) For the sensor not seeing thermal fluctuations of the inner can $10 \alpha_f A \gg 10^{-2}$
 - 3) For true feedback (high open loop gain) $10 \alpha_f A_1 \alpha_s \gg 1$

The electrical circuit was to produce a function that related the error voltage (V_s) to the correction voltage (V_e) by the graph of Figure G-1. The correction voltages are related to the correction temperature by:

$$T_{\text{corrected}}^{\text{coarse}} = \alpha_c V_e^c \qquad T_{\text{corrected}}^{\text{fine}} = \alpha_f V_e^f \qquad (G-1)$$

An analog computer was constructed that provided the relationships graphed as well as a wide range of the parameters and

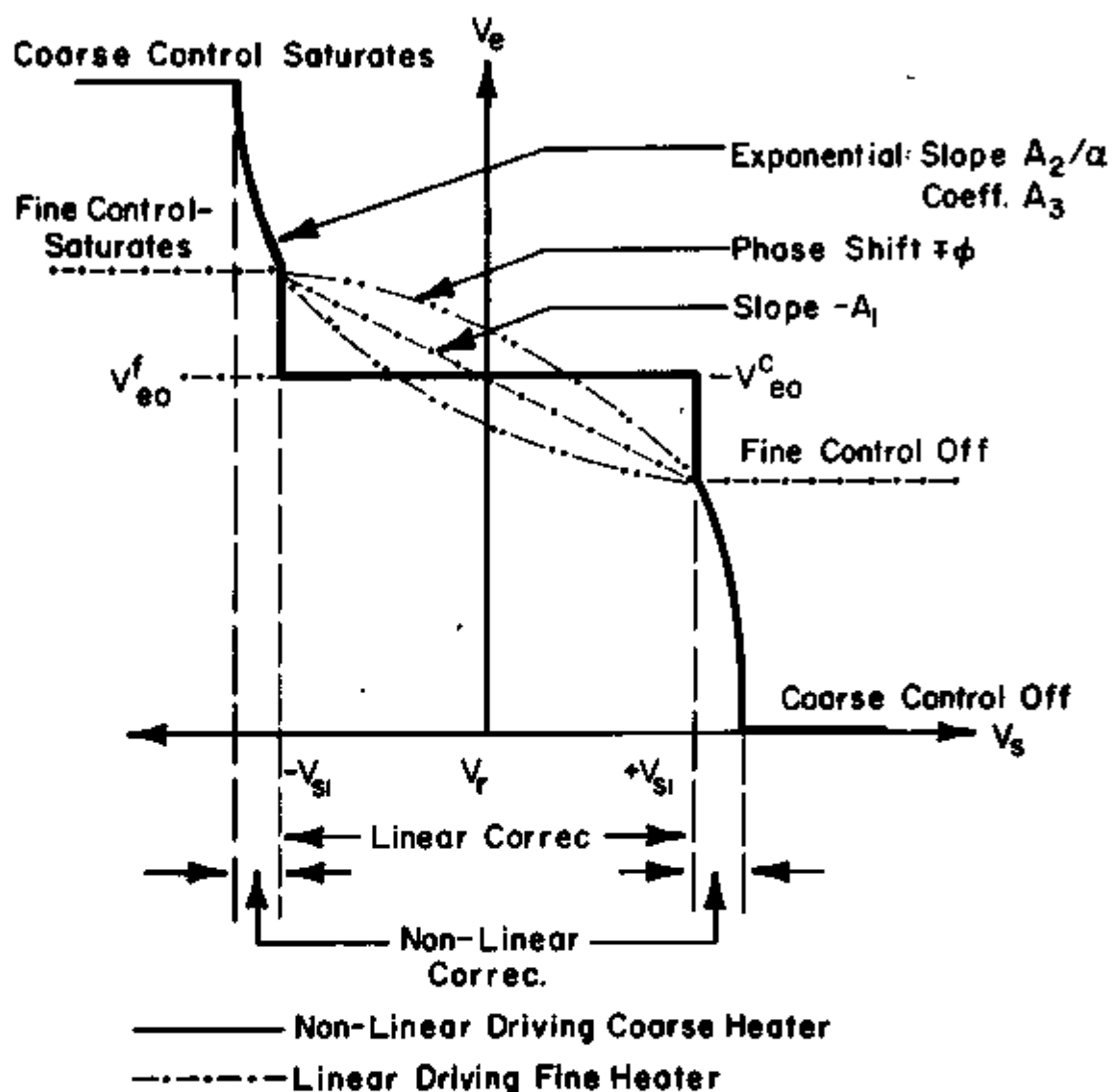


Figure G-1.

Linear and non-linear relationships between the error voltage V_e and the correction voltage V_s . Notice that hotter temperatures (less correction power) are to the right and colder temperatures (more correction power) are to the left about the quiescent bias point.

included meters to monitor the levels. The circuit is sketched briefly in Figure G-2 with all controls indicated. The functions that the analog computer produces are:

$$V_e^{fine} = A_1(V_r - V_s) + V_{eo}^f \quad (G-2)$$

$$I_R^{fine} = e^{\pm i\phi} \frac{\sqrt{V_e^{fine}}}{R_{fine}} \frac{\alpha_f'}{\alpha_f} \quad (G-3)$$

and thus:

$$T_{correction}^{fine} = \alpha_f' V_e^{fine} e^{\pm i\phi} \quad (G-4)$$

$$V_e^{coarse} = V_{eo}^c \pm A_3 (e^{\alpha|A_2(V_{ext} - V_s)|} + 1) \quad \text{where the sign is controlled by } V_s \text{ and the level } V_{st}. \quad (G-5)$$

$$I_R^{coarse} = \frac{\sqrt{V_e^{coarse}}}{R_{coarse}} \frac{\alpha_c'}{\alpha_c} \quad (G-6)$$

and thus:

$$T_{correction}^{coarse} = \alpha_c' V_e^{coarse} \quad (G-7)$$

The photos in Figure G-3 give an idea of the non-linearity possibilities of the coarse control. It was further necessary to filter the error voltage into three components. The error voltage would have a slowly varying (D.C.) term that would correspond to a slow temperature drift of the sample through the critical region. This voltage should not be servoed, but instead,

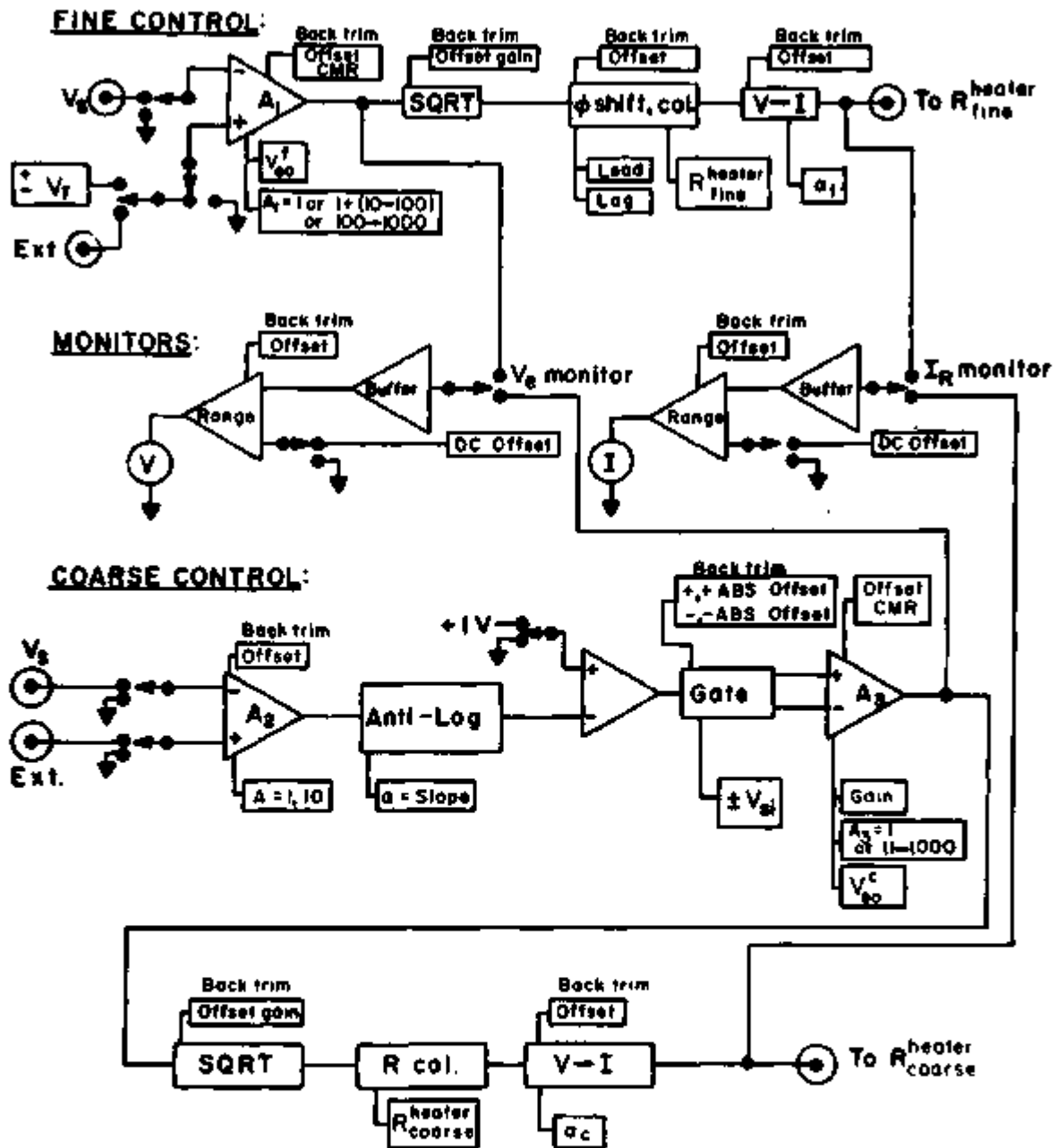
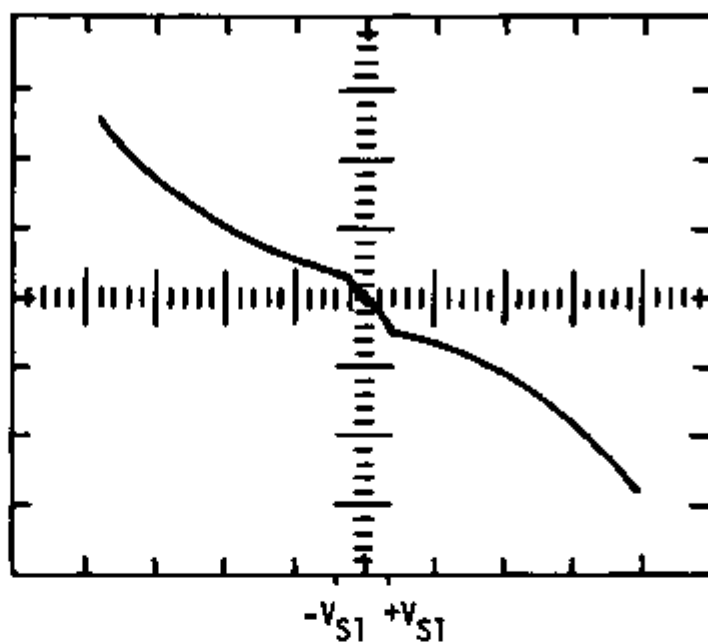
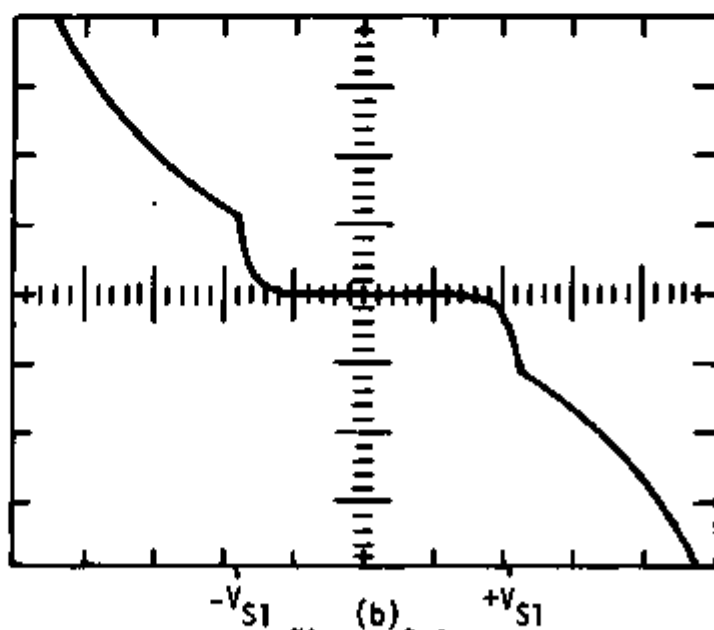


Figure G-2.

Block diagram of analog computer which was built to provide the correction curves of Figure G-1. Front panel controls are below the function and back panel controls are above the function.



(a)

(b)
Figure G-3.

Oscilloscope pictures of the non-linear functions produced by the analog computer of Figure G-2. The horizontal axis is the error voltage V_S , and the vertical axis is the correction voltage V_e (which is later converted to current). The figures are symmetric about the quiescent bias level. Figure a) has a low value for the gating voltage (V_{S1}) and Figure b) has a large value.

it should be feedback to a self-balancing bridge (see A.C. Bridges section), and thus is used to cancel the offset voltage. A low frequency component would be used for the slow drifts and a high frequency component would be used for the fast thermal feedback part. Originally the whole error signal would be fed into the analog computer as a single error signal, but later, the high frequency part was fed into the linear part, and the low frequency part was fed into the non-linear part. The active filter box, shown in Figure G-4 was constructed and accomplished this dissection of the frequency components of the error signal. The complete block diagram of the servo system is shown in Figure G-5.

The performance of the overall servo system was poor. The electronics operated perfectly, as designed, but the main problems were in the complexity of the system and the rather slow thermal time constants associated with the temperature sensor. The system operated in a stable mode with time constants of the lock-in at values down to 10msec. One could change the gain, in both directions (higher and lower), to go into unstable operation. This indicated true closed loop feedback stability. But spurious noise would throw the system out of stability and required extensive effort to get back in a stable mode. Also, the temperature regulation was only on the order of 10^{-4} K, which is quite poor by normal servo standards. To correct for the long thermal time constant between the sample block and the temperature sensor (Cryocal), two sensors were mounted symmetrically on the block and well greased to it

ACTIVE FILTER BOX

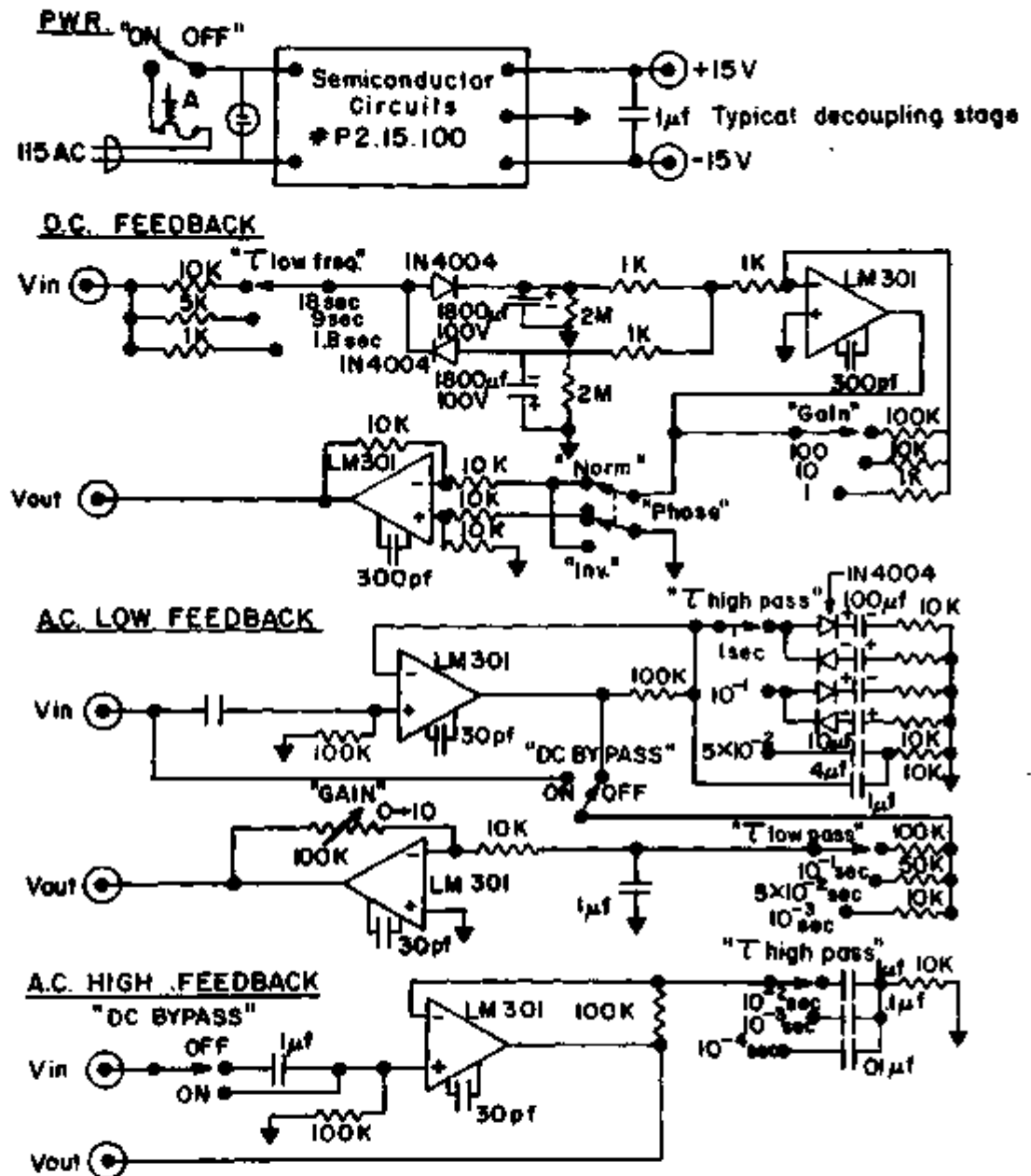
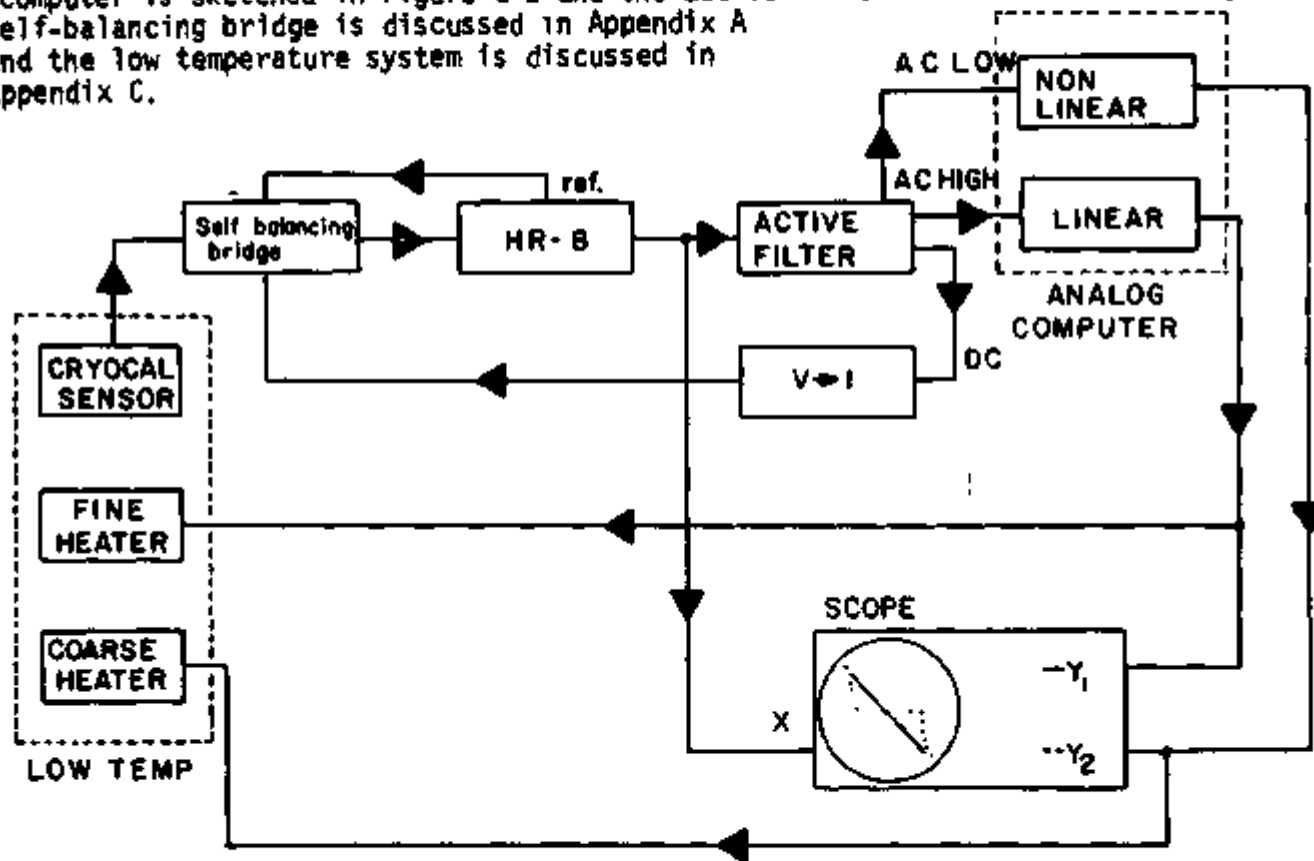


Figure G-4. Electronics for separating the D.C., low frequency and high frequency components of the error voltage V_s . Note that all resistors are 1% 1/8 W thin film; caps are non-polarized unless noted.

Figure G-5.

Complete block diagram of all components used in the temperature servo system. The analog computer is sketched in Figure G-2 and the active filter is the circuit of Figure G-4. The self-balancing bridge is discussed in Appendix A and the low temperature system is discussed in Appendix C.



(one was a Cryocal Standard; the other was a Cryo Resistor Standard). Both sets of leads were isolated with superconducting spliced wires and clamped with copper to the sample block in a lens paper sandwich. In this way, not only would the thermal time constant of the sensor be reduced, but also one could independently monitor the temperature with a sensor outside the feedback loop. The results indicated that in general a servo feedback system behaves as a self-balancing bridge, in that the heater will raise or lower the power to correct the temperature seen by the sensor. This may not be the true temperature errors exhibited by the sample block, since it is not in perfect thermal contact with the sensor. As it turned out, the sensor in the feedback loop would indicate thermal fluctuations of only $5 \mu\text{K}$, but the actual fluctuations as measured with the other sensor were on the order of $30 \mu\text{K}$.

In general, the servoing would improve the long term drifts of the sample block extensively, but at the cost of introducing short term thermal fluctuations in excess of background fluctuations. Because of the increased thermal noise introduced by the servoing, and the complexity of operation, the servoing was used only when taking point by point data, and in general the inner can was servoed by a conventional bridge from an independent sensor, and the sample block was allowed to sit at a temperature determined by a D. C. power level, and not servoed at all. This gave an accuracy of about $10 \mu\text{K}$ fluctuations to the overall experiment.

Appendix H. Sample Preparation and Resistive Transitions

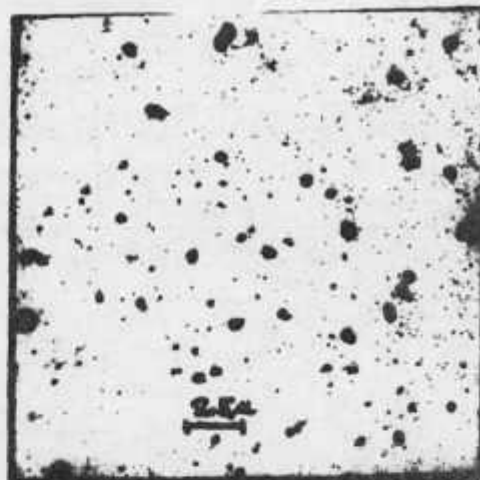
The superconducting films studied were "dirty", granular, aluminum, thin films ($\sim 1000\text{\AA}$ thick) prepared by vacuum evaporation onto a number of different room temperature substrates. Since there has been extensive experimental, as well as theoretical work into the resistive transition of "dirty", aluminum thin films, it is important to show where the samples studied agree with other workers. But, due to the diversity of other workers' sample preparation methods, and the undefined parameters in their work, the correlation will be somewhat limited. The undefined parameters include effects of thickness, grain size, strains, and "dirtiness" in raising the transition temperature (T_c). They also include effects of current densities (A.C. and D. C.), and low magnetic fields used in the measurements that change the width of the transitions. And finally, effects of the chemical environment during sample preparation become undefined parameters in the samples prepared and studied by other workers. No one group working with dirty aluminum films has characterized all these parameters for the films they studied. Thus, this section will point out the effects of the parameters mentioned above in the films studied, with a partial attempt at correlating the gross features of the resistive transitions.

If one evaporates aluminum in some impure atmosphere at a slow rate ($30\text{\AA}/\text{sec}$), one will get a granular aluminum film. The

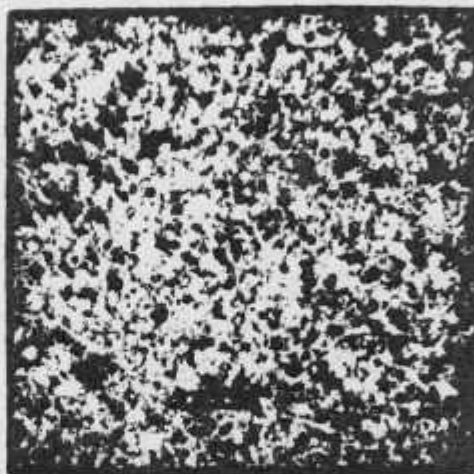
grains vary in size, but the films studied had grains on the order of 400\AA (see Fig. H-1), and have T_c 's which are consistent with the T_c 's of other work.⁴⁷ The method of providing an impure atmosphere varies widely and may not be obvious, even to the person preparing the sample. Some workers co-evaporate SiO to dirty the films. Others have a residual O_2 background. The effect of the O_2 is to first provide seed centers for granular formation (even He^4 works³⁷) and second to oxidize these grains after formation (accomplished later upon exposure to air, if not initially). These processes are governed by other processes too (the "undefined parameters" referred to earlier). The O_2 method was chosen for the author's films due to the inconvenience of working with SiO. One undefined parameter in the O_2 process is the residual water vapor in the evaporator system during evaporation. In this laboratory, Richard Carlson was making SNS tunneling junctions where the insulating layer was a 5\AA layer of Al_2O_3 , and he found that this thickness was drastically affected by the relative humidity of the room. Analysis with a partial pressure gas analyzer showed that oxide layers were dependent on the amount of water vapor present in the vacuum system. Only when going to 4 day system bake-outs at about 120°C could this background be removed. But even evaporation from Al_2O_3 coated boats introduced O_2 and H_2O vapor during evaporation. These water vapor effects are probably due to the OH^- radicals' tunneling ability to create channels in an Al_2O_3 layer that can expose the aluminum to further oxidation. Thus any films made by evaporating aluminum in an oxygen background will be greatly affected by the background water



a.) Run # 33
Approx. 6800 Magnification



b.) Run # 32
Approx. 4000 Magnification



c.) Run # 24
Approx. 4000 Magnification

Figure H-1. TEM micrographs of 1000 Å aluminum films on mica (a.), glass (b.), and self-supporting substrates (c.). The crevice in (a.) is a scratch. The large dark spots in (b.) are foreign particles. And the coarse grid (that looks like little squares) of (c.) is a replica of the salt substrate that textured the film and remained after it was remounted. Notice that the grain sizes are about the same for each substrate. The grain sizes varied between 200 Å and the film's thickness (1000 Å). These micrographs were made with the assistance of Keith Munson and Tom Hutchinson.

vapor in the evaporator, which will vary considerably from laboratory to laboratory.

The samples were prepared predominately by evaporating aluminum from an alumina coated molybdenum boat that was resistively heated. Evaporations were at rates of from 10 to 50 $\frac{\text{Å}}{\text{sec}}$ through a mask over the substrate, with a substrate to source distance of about 40 cm. It should be noted that the rate might also affect the time the grains spend in the oxidizing atmosphere. This atmosphere varied from nothing (outside of the residual O_2 at 10^{-7} torr to 10^{-4} torr O_2 , but was typically 4×10^{-6} torr). Some periods of sample preparation were marked by a very low T_c , which led to the addition of drops of water before the system was baked out (at 120 C for 12 hr.), in order to leave a partial pressure of water vapor during evaporation, and thus enhance the T_c of the films. These methods of sample preparation gave film resistivities ranging from $6 \times 10^{-5} \Omega \text{ cm}$ to $4 \times 10^{-7} \Omega \text{ cm}$ and T_c 's ranging from 1.54 K to 1.90 K. More typical samples were of resistivities of $1.5 \times 10^{-5} \Omega \text{ cm}$ and transition temperatures on the order of 1.60 K, for a thickness of 1000 Å. Since the mean free path in the films is related to the resistivity ($R_{\text{eff}} \sim \frac{4 \times 10^{-12} \Omega \text{ cm}^2}{\rho_n}$)³⁸, these films had mean free paths of about 20 Å.

These heavily oxidized films might have been actually quite dirty, and thus had low T_c 's because they were on the far side of a hump in the empirically observed relationship between T_c of the film and the level of oxidation.⁴² In fact, one extremely dirty film (30 drops of water in the evaporator) exhibited a negative slope in

its resistivity vs. temperature, and it never did go superconducting (down to 1.4K), thus indicating a semi-conductor behavior. It was also found that the heavily oxidized films exhibited considerable effects in the resistive transition from an additional D. C. current ($\sim 10\text{A}/\text{cm}^2$) used in the measurement. For some films this effect was quite sensitive, where only an increase of 10% in the current would bring about the effect. The effect was to add slight bumps and glitches ("kinks") in the resistance vs. temperature curves, which were normally reasonably smooth. If the A.C. current was made equal to the D.C. current, the effect was almost eliminated. This effect might be related to some sort of Josephson tunneling between grains⁴⁵ becoming partially coherent at certain values of D.C. current.

The films were evaporated on predominately mica substrates. These substrates were cleaved from optical quality mica to a thickness of typically $\frac{1}{2}$ mil. The mica was glued around its edges to an alumina substrate that had Pb posts attached, and the alumina substrate was in turn glued to the sample block (see Appendix C and Fig. H-2). After the aluminum film was evaporated onto the mica, silver leads ($\sim 50\text{\AA}$ thick) were evaporated from the film to the posts, and then these leads were overlaid with a $10,000\text{\AA}$ evaporated Pb coating. Finally an indium solder bead (Indium Alloy #2 solder and Flux #2, available from Indium Corp. of America, Utica, New York) was drawn between the leads and the Pb posts to complete the four terminal circuit to the film.

The films were made in both circular and rectangular geometries (see Fig. H-2). The circular films had a 2 terminal measurement, and while the overlapping leads essentially removed edge effects (and hence no scribing was needed), they provided a nonuniform current density in the film. It is interesting to note that the ratio of width/length (used in calculating R_{\square}^N) can be calculated almost exactly for the circular geometry, and it is independent of the diameter of the circle and is equal to 1.568. Because of extra parameters brought in by nonuniform current densities, the film geometry was changed to that of a rectangular form (see Fig. H-2). The edges were scribed because of possible edge effects in the transition⁴⁶, and a 4 terminal measurement was made. Later, a snake scribe was added to give a factor of ten greater resistance, which improved signal coupling and sensitivity in electrical measurements.

The films on mica substrates had predominantly multiple transitions (more than one T_c). It was at first thought that this was due to the layered nature of the mica acting like an edge effect and thus creating a T_c for steps in the mica; and thus the overall transition would have multiple T_c 's. But, films on thin glass (~ 3 mil. thick) also had multiple transitions. Even special consideration was given to examining the mica used. The mica was examined between crossed polarizers, at a large angle, to determine the existence of any differences in the thickness of the substrate, and only uniform substrates were thus used. This precaution did not

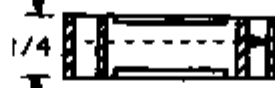
SAMPLE GEOMETRIES

1/2



Circular film
2 terminals
no scribe

3/4



Rectangular film
4 terminals
edge scribed

3/4



Rectangular film
4 terminals
edge scribed and
"snake" scribed

SELF-SUPPORTED METHOD

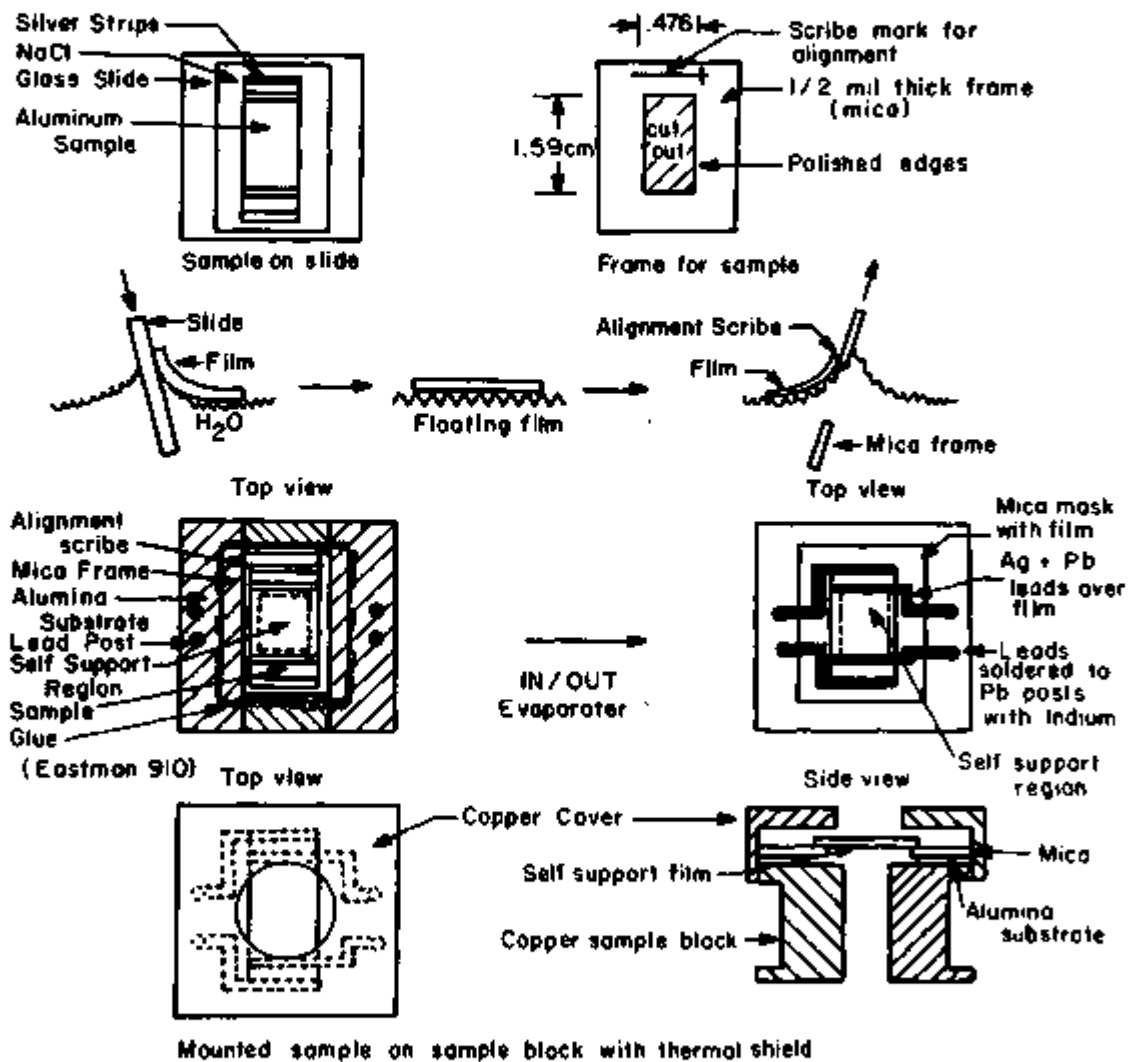


Figure H-2.

Sample geometries and self-supported film preparation method.

improve the transitions. When the measurements of the D.C. thermal conductivity of the mica were made, where the whole substrate was glued uniformly to a flat copper block, the problem of multiple transitions was solved. The previous substrates were held only on the edges and could flex during the cool down from 300 K to 4K. These stresses created multiple transitions. Two films in a row, on rigidly held substrates, had single transitions. The sensitivity of the transition to strains in the substrate has been suggested by Testardi⁴⁴ and presents the possibility of incorporating this "problem" into a very sensitive pressure gauge (although highly non-linear).

Films were also made that were self-supporting. Previous workers (ref. 39) have made self-supporting films with a variety of metals by a variety of methods, although none of their films approach the rather large size in area of these films ($\sim 1\text{cm}^2$). Films were made initially on dissolvable NaCl substrates. They exhibited large contact resistances due to extensive oxidation of the aluminum surface, probably from the Cl^- of the salt tunneling into the surface. A number of attempts were made to remove the contact resistance problem from this surface oxidation. A single NaCl crystal was used as a "plug" in a hole drilled in an alumina substrate, with the crystal cleavage plane parallel to the substrate surface. In this manner, the film and leads could be evaporated at one time and the substrate (NaCl crystal) dissolved away later by a method similar to that of ref. 40, leaving the center portion of the film over the hole in

the substrate, free standing. The problem with this method was that the boundary between the crystal and the substrate had slight crevices that the aluminum film would not quite cover, and thus the film was barely attached to the edges of the alumina substrate. A thin collodion substrate was also tried, but due to problems in surface tension and dissolving the substrate away after evaporation, this method was also discarded. The method that was finally used is similar to that in ref. 41. About 4000 Å of NaCl was evaporated onto a clean glass slide. The film was evaporated onto this substrate. Both circular (up to ½" in diameter) and rectangular (½" by ¾") films were evaporated onto this substrate. Silver "strips" were evaporated onto the rectangular films to reduce contact resistance from leads attached later (although these strips were not always necessary). The slide was very carefully lowered into a still bath of distilled, air free water (see Fig. H-2) with about 5% special denatured alcohol added. Isopropyl alcohol was also used, since it facilitated the film removal by causing less of a water drop to adhere to the film and tear the film, but it also reduced the surface tension of the water and caused the films to sink. The films would also sink on very humid (rel. hum. ~60-70%) days, due to less of a vapor-liquid boundary on the surface of the water. An opposite problem was the electrostatic charge that would cause the film to jump back upon itself during periods of very low humidity in the winter. After the film has been floated free of the slide, it is comparatively strong in the water. But, it is crucial to lower

the film into the water at about 20° from the normal angle and at a steady, continuous speed. Any jitter will cause minute tears of the film or its edges, which will later, upon drying, tear the entire film (it is advised to meditate awhile before trying to float off the films). The film then was picked out of the water by aligning the edge up on a mark on a mica frame and slowly raising it vertically out of the water. The films were at first coated with Napthalene vapor to strengthen them for removal, but although the Napthalene sublimates at room temperature, it hindered the films from sticking to the mica, and it also added to the surface contact resistance. Because the mica is very thin, and because it was raised slowly and vertically out of the water, very little water adhered to the film to "hang" onto it and cause it to rupture. The mounted film was dried by holding vertically in front of a high intensity lamp. The mask was positioned on the alumina substrate and glued around the edges with Eastman 910 glue (because the glue vapor will corrode the film, use a minimal amount). After the glue had dried, the sample block was put back into the evaporator, and leads were evaporated over the "strips". The block was removed from the evaporator (gas being added and removed slowly from the system so as not to rupture the film with a pressure gradient), and the leads were soldered to the Pb pads. The block was covered with a thermal shield and installed in the cryostat. A detector was positioned under the film to detect light passing through a ruptured film after cool down. The rectangular films tended to pull away from the long ends of the frame after cool down (due to larger

thermal contraction), while circular films had less difficulty. Films below 800 \AA thick were impractical to work with. The films of 1000 \AA thick were still thin enough to transmit visible light, since they were on the order of the metallic skin depth in thickness. The whole procedure involves a decreasing percentage of success. One has a one in four chance of floating off a good film. One has a one in three chance of remounting the film and gluing it onto the alumina. After the leads are evaporated on, one has still a 50% chance of tearing the film by the I.R. heating during soldering. Then, upon cool down, the film still can tear, due to the thermal gradients. For this reason, an optical detector was positioned below the film to detect a torn film. Finally, upon completion of the experiment, one has a slight chance of the film surviving the warm up to room temperature. One film survived the complete process outlined above without appreciable tearing, which also had data taken on it for heat capacity.

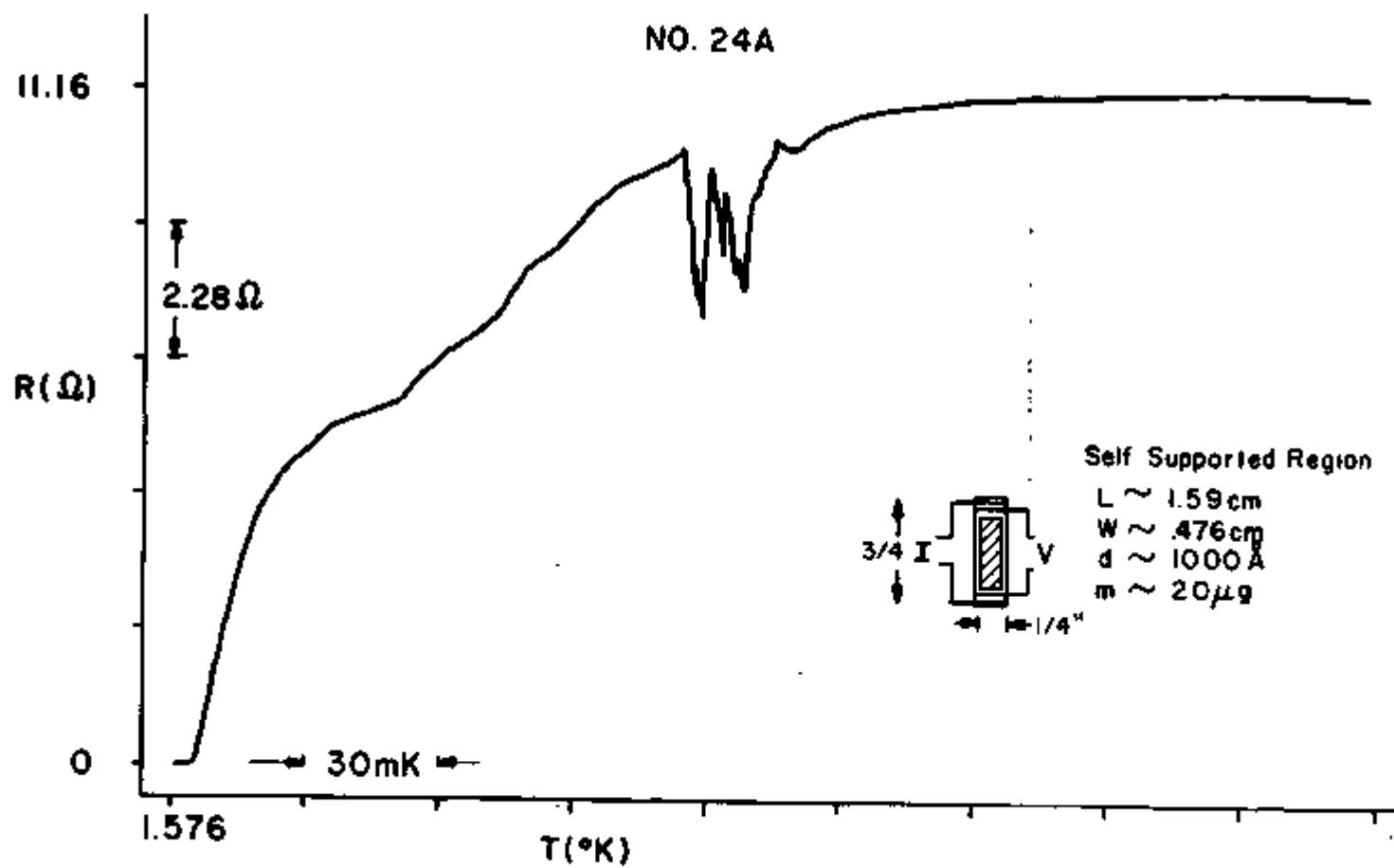
The measurements made on self-supported films showed that almost an equal thermal isolation was obtained in the experiment using a high heating frequency with the mica substrates, and due to the difficult nature of the self supported films, they were no longer studied. The films on mica were made on substrates of thicknesses from 2 mil to $\sim .1$ mil and had results similar to the results of the self supported films, which seemed to support the idea that not only is the transverse thermal conductivity of mica very low, but also that the high frequency of heating

4

essentially removes the mica from the measurement.

One self-supported film had an unusual feature in its resistive transition. This feature is unexplainable, and because it is so unusual, one hesitates to mention it. But, because measurements of the transition were made over seventy times, on two separate runs, and because the effect is a large percentage of the signals measured, one is forced to believe it as being physical. Fig. H-3 shows the resistive transition of sample #24 (see Fig. H-2 for a micrograph of the same film). This film had an unusual luster to it, i.e., very shiny and spectacular, as compared to the usually grayish self-supported films. The transition has in it a "notch" that appears as if it is subtracted off from the usual resistive transition. All the discrete details in the notch are reproducible. During both runs, a gas leak caused a very slight He^4 background ($P \ll 1\text{mm}$) that was steadily decreasing during the run (because of its being continually pumped on). The notch appeared after a few hours of running, and it moved up and down the transition with time. Figure H-4 shows successive transitions with the times between measurements indicated. This movement was periodic, with a period of about three hours and with the maximum temperature reached with each period decreasing with time. The addition of He^4 gas at a later point removed the effect. The film was destroyed during thermal cycling in a low temperature attempt to fix the gas leak. One might make a thermal runaway argument involving the He^4 gas to explain the results. Or possibly a metastable state existed in the transition, as predicted in 1-D by Tucker and Halperin.⁴⁸

Figure H-3. Resistive Transition of a Self-Supported Film.



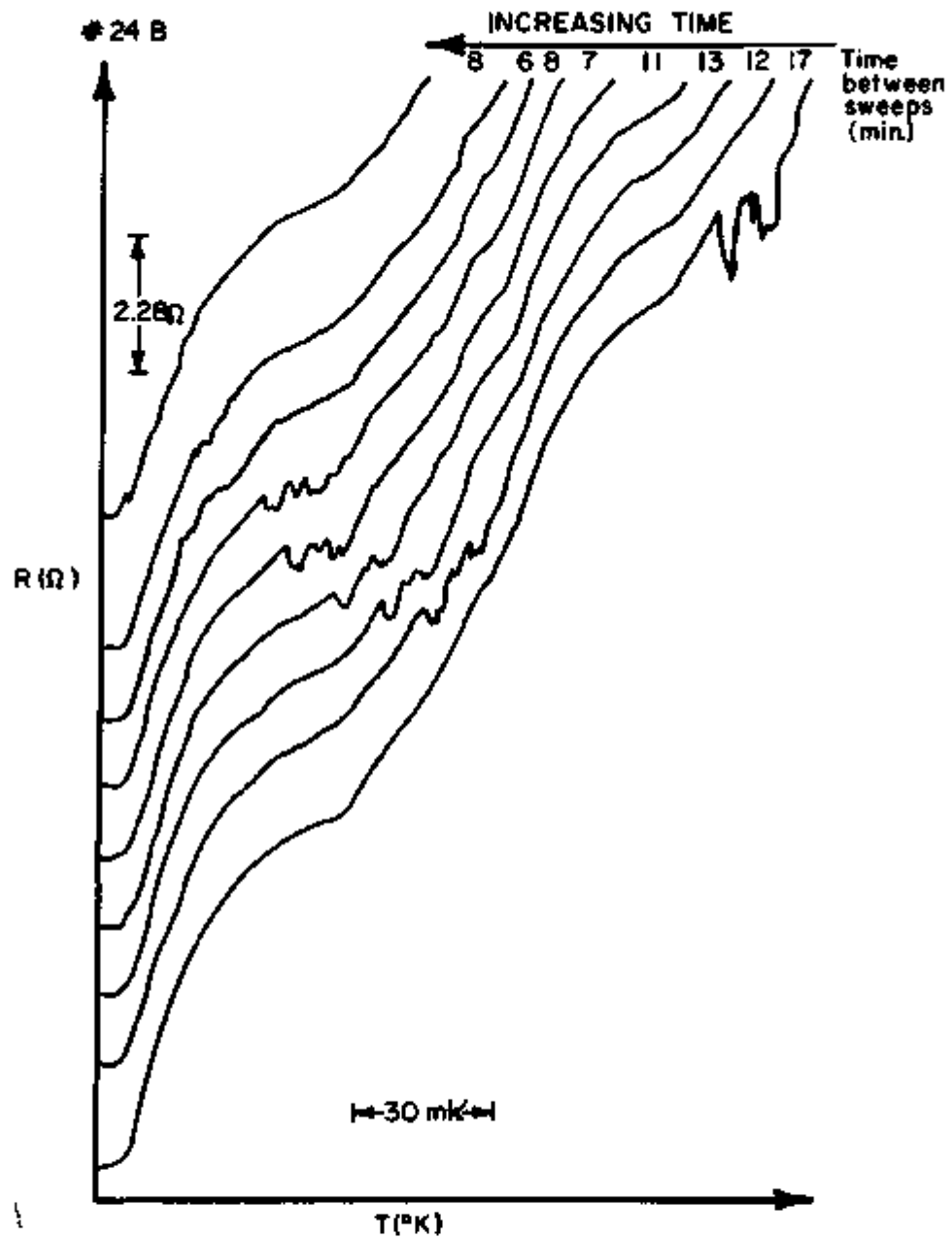


Figure H-4.

Successive resistive transitions of the film shown in Figure H-3. Notice the changing location of the "notch" in temperature for successive plots in time.

The effect was not seen in a normal "greyish" self-supported film's transition where no He⁴ gas was present (run #23). This strongly suggests some form of thermal runaway.

Magnetic field effects on the films' transition were also observed. One of the dirtier films (sample #30) exhibited a slight increase in the width of the transition for small D.C. currents (10^{-6} amp- 10^{-5} amp). The widening of the transition was linear and had a slope of about $\frac{dI}{d(\Delta T)} = 1.6 \times 10^{-9}$ amp/K. The fields associated with these currents are possibly only on the order of tens of nanogauss, so that the increase in the width of the transition may be due to some other effect. But this points out a problem in increasing current densities to measure lowering resistances. Larger magnetic fields were desired (~ 10 gauss) in the experiment, and a relatively simple solenoid was used in run #39 (diameter $\sim 3\frac{1}{2}$ ", length $\sim \frac{1}{2}$ ", ~ 108 turns) to apply a perpendicular field (although quite nonuniform, about 10% over sample region) to the sample. Figure H-5 shows three resistive transitions for three values of magnetic field (H_{\perp}) in a relatively clean (less oxidized, not to be confused with "pure") film. The transition is broadened with a long tail on the low T side, and it is moved to a lower T_c by the increasing magnetic field values. One can calculate the coherence length from these curves in the limit of $(T-T_c/T_c) \ll 1$. Then from ref. 49:

$$H_{C2} = \frac{\phi_0}{2\pi} \xi^{-2}(T) \quad \text{and} \quad H_{\perp c} = H_{C2} \quad (\text{H-1})$$

Then

$$\frac{dH_{\perp}}{dT} = \frac{\phi_0}{2\pi} \xi^{-2}(0) \frac{d}{dT} \left(\frac{T-T_c}{T_c} \right) \text{ for } \frac{T-T_c}{T_c} \ll 1 \quad (\text{H-2})$$

$$\Delta H_{\perp} = \frac{\phi_0}{2\pi} \frac{\Delta T}{T_c} \xi^{-2}(0) \quad (\text{H-3})$$

$$\xi(0) = \sqrt{\frac{\phi_0}{2\pi T_c} \left(\frac{\Delta T}{\Delta H_{\perp}} \right)} \text{ where } \phi_0 = 2 \times 10^{-7} \text{ gauss cm}^2$$

ΔT is the shift in T_c due to the field ΔH . (H-4)

For the film of Fig. H-5, this becomes:

$$\xi(0) = \sqrt{\frac{(2 \times 10^{-7})}{(2\pi)(1.81)(9 \times 10^2)}} \text{ cm} = 440 \overset{\circ}{\text{A}} \quad (\text{H-5})$$

And since for dirty superconductors:

$$\xi(0) = .85 \sqrt{\lambda_{\text{eff}} \xi_0} \text{ where } \xi_0 = 1.6 \times 10^4 \overset{\circ}{\text{A}} \text{ for aluminum} \quad (\text{H-6})$$

This gives an effective mean free path of $1.6 \overset{\circ}{\text{A}}$. Using the expression used earlier to predict the λ_{eff} from the normal sheet resistance ($R_{\square}^N \sim 1.5 \text{ } \Omega/\text{sq}$), one finds an estimated $\lambda_{\text{eff}} \sim 2.6 \overset{\circ}{\text{A}}$, which is not in too good agreement, probably because the resistivity method of calculation is not as accurate. (The work of ref. 50 measure an λ_{eff} as low as $1.6 \overset{\circ}{\text{A}}$ in similar films). Thus the film's resistive behavior in small magnetic fields is in reasonable agreement with theory and other worker's results (ref. 50).

The resistive transitions were measured in a dynamical way.

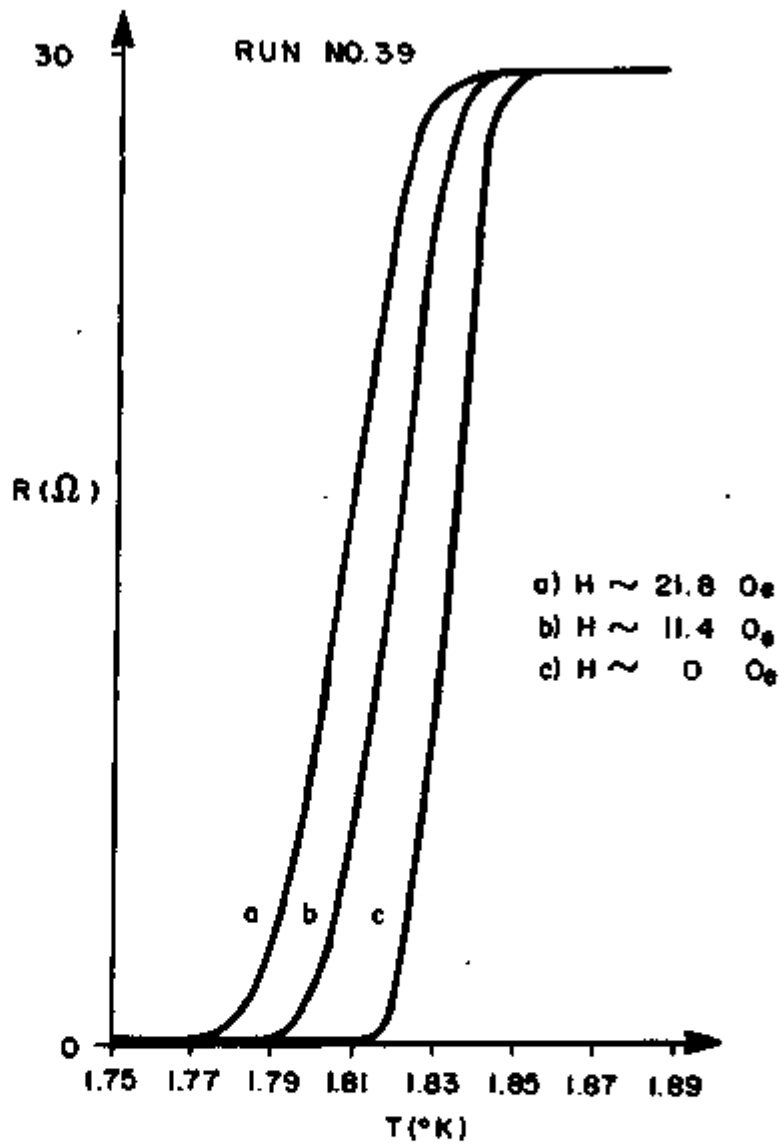


Figure H-5.

Resistive transitions for film #39 for three values of magnetic field (H). The field widens the transition, and moves it to a lower temperature.

The film was biased with a low frequency (41.5 Hz, and thus little of an out of phase component) constant current source, and the voltage produced was phase sensitive detected. The resulting output voltage was scaled to the bridge-measured, normal resistance of the film. The off null voltage from a bridge measurement of a calibrated germanium resistor (see A.C. Bridges Appendix) was scaled to represent temperature. Thus, by making an x-y plot of these two voltages, while the temperature of the sample was steadily increased, one could obtain a 1st order approximation of the resistive transition. As a check on this method, a point by point plot was done using two nulled A.C. bridges, one on the film and one on the thermometer, to measure the transition. Also a point by point plot was done using a D.C. voltage measurement (averaged for both positive and negative currents, to remove emf effects). All three methods agreed quite well. The main error in the voltage-voltage plot is associated with the slightly non-linear relationship between temperature and the off null voltage of the germanium resistor bridge. This gives the overall transition about a 5% error, but a much less error is associated for smaller regions. In this way, the film's resistive transitions were measured and recorded both on an analog trace (x-y recorder) and stored in digital form by a computer (A/D's, and a Nova 1200).

The general features of the films studied were: 1) the resistivities were $\rho_n \sim 10^{-5} \rightarrow 10^{-6} \Omega \text{ cm}$; and therefore (using the relationship between λ_{eff} and R_D^N); 2) the mean free path was

$\lambda_{\text{eff}} \sim 10 + 100 \text{ \AA}$; 3) the films had mostly 1000 \AA thicknesses (as measured with a quartz thickness monitor and later checked by optical methods); 4) they had T_c 's $\sim 1.54\text{K} + 1.93\text{K}$, but predominantly in the $1.7\text{K} + 1.9\text{K}$ range; 5) the transition widths were broadened for the dirtier films and were $\Delta T \sim 14 + 200 \text{ mK}$, where $\Delta T = T(\text{RN}) - T(2/3\text{RN})$; and 6) the ratio of room temperature resistance to the normal resistance was $\sim .63 + 1.2$. The heavily oxidized films had their transitions altered with D. C. currents, and were more likely to have multiple transitions.

To compare more detailed features of the films, involves fitting the film to an A.L. form for the transition (see Theory Section of thesis) and comparing to other work the fitted transition width (τ_0). A. L. Theory works only for a small part of the transition ($T > T_c$), and thus the comparison of the fitted width parameter to other workers depends on how much of the transition is used in the fit. Strongin,⁵¹ et.al., have made aluminum films with very small λ_{eff} ($.2 \text{ \AA}$) and which are quite thin (100 \AA). They observe that their fitted $\tau_0 \sim 10 \tau_0^{\text{A.L.}}$. Bhatnagar,⁵² et.al., have measured aluminum film transitions for a number of thicknesses. They find the thicker films ($\sim 1000 \text{ \AA}$) have a broadening of the transition width ($\tau_0 \sim 10 \tau_0^{\text{A.L.}}$), but also a considerably lower T_c (1.3K), which implies their films are quite clean and would need a Maki-Thompson correction to explain the broadening (see Theory Section). Kajimura and Mikoshiba⁵³ have done extensive work on dirty aluminum films. They find that as one goes to cleaner

systems (λ_{eff} larger), they get less agreement for the A.L. width parameter ($\tau_0 \sim 10 \tau_0^{\text{A.L.}}$ for $\lambda_{\text{eff}} \sim 1000 \text{ \AA}$). In their later work (ref. 54), they include the Maki-Thompson correction and fit their data to a theory involving both the A.L. term and the Maki-Thompson term. They determine an empirical relationship between the pair breaking parameter ($\delta(0)$) and R_{\square}^N where:

$$\delta(0) = 6 \times 10^{-4} R_{\square}^N = \frac{(T_{\text{co}} - T_c)}{T_c} \quad \text{where } T_c \text{ is the transition temperature in the absence of the pair breaking.} \quad (\text{H-7})$$

This means that the dirtier films, which had a larger R_{\square}^N due to a smaller λ_{eff} , had a larger pair breaking mechanism. They mention the possibility of the O_2 in the Al_2O_3 acting as a diamagnetic material involved in the pair breaking. They mainly feel the mechanism in pair breaking is due to a localized moment and a proximity effect with the substrate. Thus, one would expect the dirtier films not to have a Maki-Thompson correction in the conductivity because of the enhanced pair breaking. Masker and Parks,³⁸ also find the disagreement with the $\tau_0^{\text{A.L.}}$, to be in the cleaner films. It should be noted that most of this work involves films that have a very small width to length ratio ($\sim 10^{-3}$) and are in a zig-zag pattern. The total area of their films is on the order of the films studied in this experiment (1 cm^2). Since the films studied in this experiment tended to be broadened and have transition widths wider than the expected $\tau_0^{\text{A.L.}}$, one might

suspect the films were broadened by inhomogeneities. But, due to the large difference in the geometry of the samples studied when compared to the other work mentioned, there might be another explanation for the broadening.

Patton's theory (see the Theory section of this thesis) was used in comparing many experiments on aluminum films by Parks, et.al.,⁵⁵ shown in Fig. H-6. A value for the pair breaking parameter ($\delta(0)$) of 2×10^{-4} was chosen (in the limit of weak pair breaking, where Patton's theory is valid, i.e., $\delta(0) = \tau_{CO} \leq 0.3$). They plot the ratio of the excess conductivity divided by the A.L. excess conductivity ($\sigma'/\sigma'^{A.L.}$) for a reduced temperature of $\epsilon = 0.03$ (chosen because σ 's not as dependent on R_{\square}^N for small ϵ) vs. the normal sheet resistance R_{\square}^N . The A.L. theory is a straight horizontal line (independent of R_{\square}^N) and $\sigma'/\sigma'^{A.L.} = 1$. The Thompson Theory is also a straight line with $\sigma'/\sigma'^{A.L.} \approx 11$. Then by plotting many experiments on Pb, Sn, Al, and Bi, they show that the strong pair breaking systems (Pb, Bi) are near the A.L. theory, and they have a pair breaking parameter of $\tau_{CO} \approx .02$. But the aluminum data shows a curve that agrees with the A.L. theory for large R_{\square}^N and goes smoothly over to the Thompson theory for small R_{\square}^N (large pair breaking). By using the value of $\tau_{CO} = 2 \times 10^{-4}$, Patton's theory is able to agree well with all the data in aluminum films plotted. This plot then could be a convenient method of showing where the films studied in this experiment agree with the films studied by other

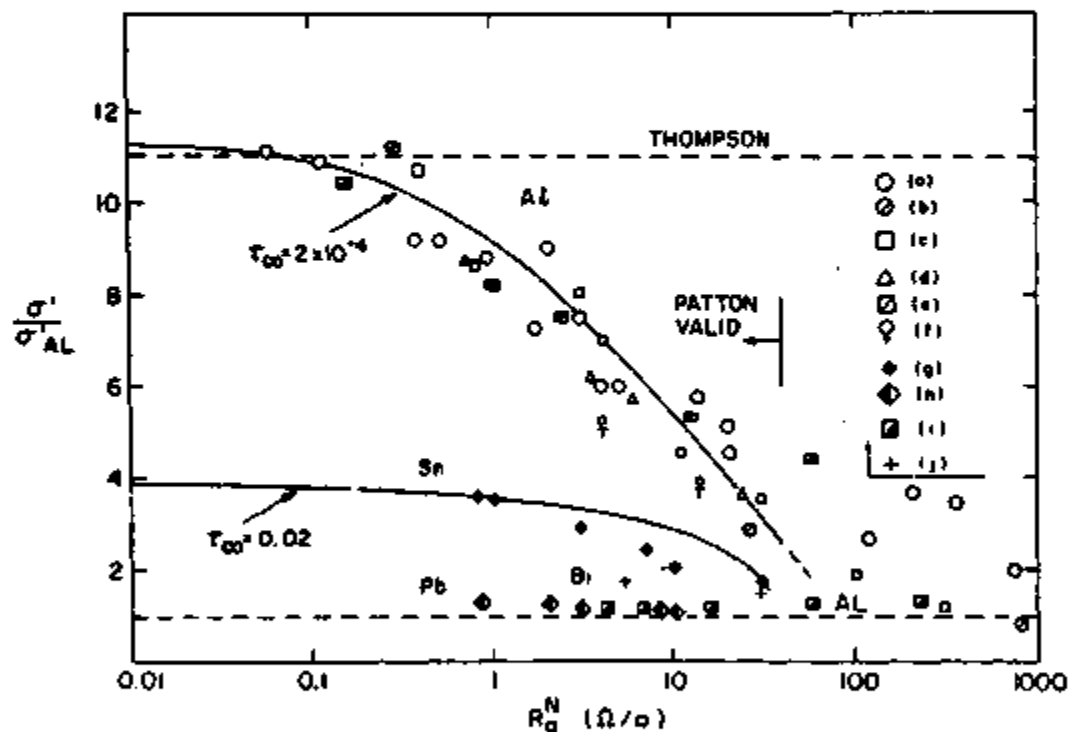


FIG. 5. Ratio of the excess conductivity measured at $\tau = 0.03$ (Ref. 47) to that expected from the AL theory as a function of the normal sheet resistance R_{\square}^N of the samples. The data presented are a collection of the work from seven laboratories and twenty experimenters as indicated below. The solid lines are theoretical predictions by Patton [Eq. (4)] for $\tau_{co} = 2 \times 10^{-4}$ and $\tau_{co} = 0.02$, respectively. The upper dashed line is the prediction of Thompsett's theory for $\tau_{co} = \tau_{co} = 2 \times 10^{-4}$ [Eq. (3)]. The lower dashed line is the AL theory. The decrease in the ratio from the Al system to the Pb system is expected from thermal pair breaking as explained in Sec. IV D.

Figure H-6.

workers, since all films have the Curie-Weiss form ($\sigma' \propto \epsilon^{-1}$), but differ in the width of the transition. But, the arbitrariness of choosing the plane of the plot only for the value of $\epsilon = .03$ distorts the overall understanding, since the ratio of $\sigma'/\sigma'^{A.L.}$, depends on where in the transition (the value of ϵ) one is looking. Also, R_{\square}^N is not such a unique parameter, since films of very large R_{\square}^N are very thin ($\sim 100 \text{ \AA}$) and have quite a different geometry and substrate relationship than films of smaller R_{\square}^N and thus thicker samples. The ratio of $\sigma'/\sigma'^{A.L.}$ can be also written as:

$$\frac{\sigma'}{\sigma'^{A.L.}} = \left[\frac{RN-R}{R} \frac{1}{R_{\square}^N d} \right] \left[\frac{1.52 \times 10^{-5} R_{\square}^N}{R_{\square}^N d} \right]^{-1} \quad \text{where } \epsilon = \frac{T-T_c}{T_c} \quad (\text{H-8})$$

for $\epsilon = .03$, then $T = 1.03 T_c$ and eq. H-8 becomes:

$$\left. \frac{\sigma'}{\sigma'^{A.L.}} \right|_{\epsilon = .03} = \left[\frac{RN}{R(T=1.03 T_c)} - 1 \right] \frac{1.97 \times 10^3 \text{ \Omega/sq}}{R_{\square}^N} \quad (\text{H-9})$$

Thus if the ratio $RN/R(T=1.03 T_c)$ is ~ 2 for large R_{\square}^N and very close to 1 for small R_{\square}^N , one can see how the plot in Fig. H-6 is just showing the inverse relationship of $\sigma'/\sigma'^{A.L.}$ to R_{\square}^N . This does not imply that is all it is showing, but just that the features of the data on aluminum are coming from the value for the ratio $RN/R(T=1.03 T_c)$ at different values of R_{\square}^N .

and that the choice of the ratio was arbitrary. It should also be noted that the relationship shown earlier between R_{\square}^N and $\lambda_{\text{eff}} \times d$ (thickness), implies that one cannot tell the difference on the plot of Fig. H-6, between a dirty thick film (λ_{eff} small, d large) and a clean thin film (λ_{eff} large, d small). In fact some of the data used in the plot of Fig. H-6 is from ref. 38, which involved work on films that had extremely wide transitions (600 mK) and were quite thin (150 Å). Since one might expect the proximity effect involvement in pair breaking (mentioned earlier) to be seen in thinner films, and since short mean free path films also exhibit strong pair breaking, the agreement of the plot in Fig. H-6 for large values of R_{\square}^N may be related to the inverse of the product of λ_{eff} and d rather than R_{\square}^N . And, consequently, the thicker films' disagreement with A.L. theory may be due to the absence of pair breaking from larger λ_{eff} and less of a substrate proximity effect, rather than simple relationship of just small R_{\square}^N shown. Thus, the apparent understanding of resistive transitions shown in Fig. H-6 is misleading. A similar plot for the films used in this experiment indicates reasonable agreement with the A.L. theory in that it is horizontal for all R_{\square}^N , but at a higher ratio of $\sigma'/\sigma^{\text{A.L.}}$, since the plot involved $\sigma'/\sigma^{\text{A.L.}}$ for a $\sigma' = \tau_0 \epsilon^{-1} \sigma_N$ fit for all ϵ . When ϵ is large (.03) the agreement can be made quite good and films are closer to the ratio of 10 for $R_{\square}^N \sim 1 \Omega/\text{SQ}$. A better approach is to use the graphic plots of $R' = (RN)(R)/(RN-R)$ vs. T , and fit the data to a straight line in some region. If

$T_c = T(R=0)$, then $T = 1.03 T_c$ is the region in the R' plot where the best value of τ_0 ($\tau_0 = \frac{RN}{T_c \left(\frac{dR'}{dT} \right)}$) for the films studied is obtained, and the films agree with the plot of Fig. H-6.

In conclusion, the films studied have a short λ_{eff} and should have a somewhat good agreement with the A.L. theory, which does not involve pair breaking. But, because of the thicknesses of the films studied, there might be a proximity effect pair breaking mechanism. The films do fit an ϵ^{-1} behavior, but with larger transition widths (τ_0). The films cannot be directly compared to the other workers because of the large differences in the geometry and current densities used in the studies. There is the possibility that the films are inhomogeneously broadened, since τ_0 is larger than $\tau_0^{A.L.}$. But if one chooses a small enough region to fit to A.L. theory, this disagreement can be partially removed. The agreement with theory was best for films made without O_2 on a rigid substrate.

References for Appendices

1. Cryocal Inc., 1371 Ave. "E", Riviera Beach, Florida, 33404.
2. J. T. Anderson, "Thermal Phase Fluctuations in a Josephson Junction...", Ph.D. Thesis, U of Minn., 1971, unpublished.
3. J. J. Hill, A. P. Miller, "Seven Decade Adj-Ratio... Voltage Divider...", Proceed. of IEE, 109, part B, 157 (1962);
J. J. Hill, A. P. Miller, "An A.C. Double Bridge...", Proceed. of IEE, 110, 453 (1963).
4. Automatic Systems Laboratories, Construction House, Grovebury Road, Leighton Buzzard, Bedfordshire, England.
5. J. C. Solinsky, "Operation of GaAs LED's and Si Detectors at 4.2 K", Rev. Sci. Inst., 41, 1886 (1970).
6. Light guides were the "Crofon" fiber optics, available from Edmund Scientific Co., Barrington, N. J., in bundle sizes of 16, 32, 48, 64, fibers per bundle, with a transmission range of 13,300 Å to 3,300 Å.
7. Light bulbs available from Axialight Corp. (formerly Starlight Corp), P. O. Box 325, Mountain Home, North Carolina, 28758. Model 15-2260- 1.5 v, 15 ma. was used extensively. Those bulbs are only 60 mil. long and 22 mil. in diameter, with a filament of 8½ turns on about a 5 mil. diameter and only about 40 mil. long, yet their output powers are up to 150 μ watts.
8. See for a complete review the article by J.E. Zimmerman, Proceed. of IEE 1972 Appl. Superconductivity Conf., Annapolis Maryland, May 1-3, (1972) pg. 544.

9. J. E. Zimmerman, P. Thiene, J. T. Harding, *J. Appl. Phys.* 41, 1572 (1970).
10. S.H.E. Manufacturing Co., 3422 Tripp Court, Suite B, San Diego, California 92121.
11. Richard J. Warburton, "Fluctuations Near the Phase Transition in 1-D Superconductors", Ph.D. Thesis, Cornell University, Ithaca, N. Y. (1971).
12. S. F. Strait, "Development of Mech. Stable Thermally Cyclicable Point Contacts for use in Superconducting Devices", Ms. Thesis, Cornell University, Ithaca, N. Y., (1971):
13. D. R. Nordlund, *Rev. Sci. Inst.*, 43, 1699 (1972).
14. J. Keighley, P. Rhodes, *Infid Phys.*, 12, 277 (1972).
15. James, Smith, Wolford, "Analog and Digital Computer Methods" or any Analog Computer Manual (i.e., Electronics Associates Inc., "Handbook of Analog Computation").
16. J. W. T. Dabbs, "Method for Obtaining Second Derivatives in Electron Tunneling", preprint. Also see, D. E. Thomas, J. M. Rowell, *Rev. Sci. Inst.*, 36, 1301 (1965) and W. R. Patterson, J. Schewchun, *Rev. Sci. Inst.*, 35, 1704 (1964).
17. J. E. Houston, R. L. Park, *Rev. Sci. Inst.*, 43, 1437 (1972).
18. R. B. Blackman, J. W. Tukey, "The Measurement of Power Spectra", Dover Publications (1958).
19. S. Brandt, Statistical and Computational Methods in Data Analysis, North Holland Publ. Co. (1970).

20. P. Sullivan, G. Seidel, *Proceed. of 1966 LT-Cal. Conf.*,
Ann. Acad. Sci. Fennicae., A VI, #210, pg. 58 (1966);
 P. Sullivan, G. Seidel, *Phys. Rev.* 173, 679 (1968);
 P. Handler, D. Mapother, M. Rayl, *Phys. Rev. Letters* 19,
 356 (1967). It should be noted that N. Zavaritskii (*Progress
 in Cryogenics*, 1, 207, Heywood & Co., London (1959)) first
 developed A.C. methods, but it was in a more complicated nature
 of phase shifts with thermal waves, rather than simply steady
 state amplitude variations.
21. The imaginary part of the index of refraction for k for this
 wave length is about 6.00 (see Heavens, *Optical Properties of
 Thin Solid Films*, Dover 1965) Then $\alpha = 2\pi k/\lambda = 6 \times 10^5 \text{ cm}^{-1}$.
22. S. Crandall, *Quar. of Appl. Math.*, 13, 318 (1955).
23. R. Zerkle, J. Saunderland, *J. Heat Transfer*, 87, 117 (1965).
24. G. K. White, *Exp. Tech. in Low Temp. Physics*, Oxford, England
 (1968).
25. R. C. Weast, *C. R. C. Handbook of Chem. & Physics*, The Chemical
 Rubber Co., Ohio (1971).
26. C. B. Satterthwaite, *Phys. Rev.* 125, 873 (1962).
27. R. L. Greene, C. N. King, R. B. Zubeck, J. J. Hauser, *Phys. Rev.* B6,
 3297 (1972).
28. D. E. Gray, *AIP Handbook* (page 4-159), McGraw Hill, N.Y. (1971).
29. K. K. Kelley, *J. Am. Chem. Soc.* 61, 471 (1939).
30. P. Mahadev, M. F. Panczyk, R. A. Scribner, J. G. Daunt,
Phys. Letters 41A, 221 (1972).

31. W. E. Keller, $\text{He}^3 + \text{He}^4$, Plenum Press, New York 1969.
32. D. H. Martin, D. Bloor, *Cryogenics* 1, 159 (1961).
33. C. L. Bertin, R. Rose, *J. Appl. Phys.* 39, 2561 (1968).
34. L. R. Testardi, *Phys. Rev.* 84, 2189 (1971).
35. W. H. Parker, W. D. Williams, *Phys. Rev. Letters* 29, 924 (1972).
36. C. S. Owen, D. J. Scalapino, *Phys. Rev. Letters* 28, 1559 (1972).
37. D. H. Liebenberg, Los Alamos, N. M., Private communication.
38. W. Masker, R. Parks, *Phys. Rev.* B1, 2164 (1970).
39. H. Oona, D. G. Rickel, *Rev. Sci. Inst.* 38, 980 (1967);
A. Imbusch, *Rev. Sci. Inst.* 38, 974 (1967);
G. Munch, *Rev. Sci. Inst.* 35, 524 (1964).
40. G. J. Unterkofler, and R. Verderber, *Rev. Sci. Inst.* 34,
820 (1963).
41. F. Wooten, *Rev. Sci. Inst.* 38, 124 (1967).
42. G. Deutscher, H. Fenichel, M. Gerschenson, E. Grunbaum,
International Low Temperature Conference #13, Boulder, Colorado,
Paper # Ga59 (1972).
43. N. A. Pankratov, G. A. Zaitsev, I. A. Khrebtov, *Cryogenics*,
April, 242 (1973).
44. L. R. Testardi, *Physics Letters* 35A, 33 (1971).
45. G. Deutscher, *Physics Letters* 35A, 28 (1971);
P. Pellian, G. Dousselin, H. Cortès, J. Rosenblatt, *Solid State
Comm.* 11, 427 (1972).
46. M. Strongin, O. F. Kammerer, A. Paskin, *Phys. Rev. Letters* 14,
949 (1965); P. N. Chubov, V. V. Eremenko, Yu. A. Piliipenko,
Soviet Phys., JETP 28, 389 (1969).

47. A. Rothwarf, Physics Letters 30A, 55 (1969).
48. J. R. Tucker, B. I. Halperin, Phys. Rev. B3, 3768 (1971).
49. D. Saint James, G. Sarma, Type II: Superconductivity, Pergamon Press, New York (1969) pg. 46.
50. B. Abeles, R. W. Cohen, W. R. Stowell, Phys. Rev. Letters 18, 902 (1967); R. W. Cohen, B. Abeles, Phys. Rev. 168, 444 (1968).
51. M. Strongin, O. F. Kammerer, J. Crow, R. S. Thompson, H. L. Fine, Phys. Rev. Letters 20, 922 (1968).
52. A. K. Bhatnagar, P. Kahn, T. J. Zammit, Solid State Comm. 8, 79 (1970).
53. K. Kajimura, N. Mikoshiba, Physics Letters 32A, 216 (1970).
54. K. Kajimura, N. Mikoshiba, J. of Low Temp. Phys. 4, 331 (1971).
55. R. A. Craven, G. A. Thomas, R. D. Parks, Phys. Rev. B7, 157 (1973).
56. The heat capacity of the mica used for the substates was measured independently using conventional methods by Prakash Thadani and extrapolates to $C = 1.1 \times 10^{-4} \text{ J/gm}^{\circ}\text{K}$ at 1.83 K with no unusual behavior in this region. The author is deeply grateful to Prakash Thadani for obtaining these results.

Acknowledgements

The thesis advisor and friend of the author, Allen M. Goldman, suggested this work. It was through the constant communication and mutual support that this work was completed. Without this open and frank relationship that endured between the author and Professor Goldman and a lot of luck, this work would not have been possible.

The author would like to thank Professor Allen M. Goldman for the counsel and aid received during this work and for the encouragement and confidence in the author's research.

The author acknowledges the support for this research by the Metallurgical Division of the A.E.C. on Contract #AT(11-1)-1569. The author also thanks the Office of Naval Research for providing the He gas used in this experiment. A grant from the Research Corporation made possible the mini-computer used in this work. The Graduate School of the University of Minnesota made funds available for the Tektronix display system. The author also acknowledges Earl Klugman for the extended loan of the P.A.R. #126 lock-in used in this work.

The author thanks T. Hutchinson and K. Munson for the assistance with the TEM measurements. The author is grateful to Prakash Thadani for the heat capacity measurements made on the mica substrates. The skills of Don Gooding in the cryostat construction and SQUID fabrication made some experimental aspects of this work

possible. The evaporator system used for film preparation was built by Peter Kreisman. It was through the urging of Patrick Lee that the magnetic field studies were made. The interaction with fellow graduate students was a constant source of enlightenment.

Finally, without the love and understanding of the author's graduate-widow wife and family and their desire to return to a more liveable climate, this work would not have been possible.